# Isolierte Neutronensterne und ihre sub-stellaren Begleiter

## Dissertation

zur Erlangung des akademischen Grades doctor rerum naturalium (Dr. rer. nat.)



vorgelegt dem Rat der Physikalisch-Astronomischen Fakultät der Friedrich - Schiller - Universität Jena

von Dipl.-Phys. Bettina Posselt geboren am 7. Juni 1977 in Bernburg

#### Gutachter:

- 1. Prof. Dr. Ralph Neuhäuser, Friedrich-Schiller-Universität Jena
- 2. Prof. Dr. Günther Hasinger, Max-Planck-Institut für extraterrestrische Physik Garching
- 3. Prof. Dr. Klaus Werner, Eberhard-Karls Universität Tübingen

Tag der letzten Rigorosumsprüfung: 1.12.2006

Tag der öffentlichen Verteidigung: 21.12.2006

# Zusammenfassung

Neben den Radiopulsaren, die die Mehrheit der gegenwärtig beobachteten Neutronensterne ausmachen, gibt es radioleise junge Neutronensterne mit rein thermischer Röntgenstrahlung. Diese Neutronensterne haben ihr Emissionsmaximum unterhalb von 1 keV, sind also weiche Röntgenquellen. Diese Gruppe ist sehr interessant für die Forschung, weil man bei ihnen direkt die Emission der Neutronensternphotosphäre beobachtet im Gegensatz zur magnetosphärischen Emission, die z.B. bei nahezu allen bekannten Radiopulsaren überwiegt. Man kennt nur sieben, vermutlich sehr nahe (< 500 pc) gelegene Vertreter dieser Neutronensterne. Innerhalb der nahen Sonnenumgebung repräsentieren diese Objekte jedoch etwa ein Viertel der bekannten Neutronensternpopulation. Es stellt sich die Frage, wo und wieviel weitere, ähnliche Neutronensterne auffindbar sind.

Die vorliegende Arbeit widmet sich zum einen dieser Frage, sowohl in Form von Simulationen der erwarteten, beobachtbaren Anzahl dieser Objekte als auch mittels einer Kandidatensuche. Zum anderen beschäftigt sich diese Arbeit mit möglichen sub-stellaren Begleitern um junge Neutronensterne.

Populationssynthese junger kühlender Neutronensterne In dieser Arbeit wird untersucht, wie gut die unter Anwendung verschiedener Annahmen simulierte Anzahl von Neutronensternen mit den Beobachtungen übereinstimmt und wieviel mehr Neutronensterne man unter den detektierten, schwachen Röntgenquellen aufgrund dieser Simulationen erwarten kann. Wichtige Fragen sind der Einfluss der Verteilung der Vorgängersterne und der Absorption durch das Interstellare Medium auf die vorhergesagten Neutronensternzahlen. Massereiche Sterne, die sich zu einem Neutronenstern entwickeln können, sind besonders häufig in OB- oder Sternenassoziationen zu finden. Dies wird erstmals in dieser Arbeit im Detail berücksichtigt und führt im Ergebnis zu einer Konzentration von jungen kühlenden Neutronensternen in Richtung dieser Assoziationen. Die Absorption der Röntgenstrahlung in besonders dichten Gebieten des Interstellaren Mediums (ISMs) führt dagegen in der entsprechenden Richtung zu weniger erwarteten Neutronensterndetektionen. Die Absorption durch das ISM nimmt auch Einfluss auf die Gesamtzahl der Neutronensterne für eine bestimmte Röntgenflussempfindlichkeit. In dieser Arbeit werden zur Bestimmung der Absorption zwei unterschiedliche dreidimensionale Modelle für die Verteilung des ISMs entwickelt, getestet und angewendet. Eine wichtige, gemeinsame Grundlage für diese Modelle ist das Natriumdichtemodell aus Messungen von Lallement et al. (2003). Die beiden Modelle, ein analytisches und ein auf Sternenextinktionsmessungen beruhendes Modell, erweisen sich als realistisch bezüglich der Wiedergabe von bisherigen Beobachtungsergebnissen von Sternhaufen oder Neutronensternen. Es sind jedoch großskalige Modelle, die bei größeren Entfernungen im Detail ungenau werden. Ein Unterschied von einem Faktor zwei in der vorhergesagten Gesamtzahl von Neutronensternen mit sehr schwacher Röntgendetektion bei Verwendung dieser beiden Modelle verdeutlicht die Notwendigkeit einer Weiterentwicklung dieser ISM-Modelle. Als Nebenprodukt sind unter Verwendung der ISM-Modelle und Röntgenspektren erstmals die Entfernungen zu zwei radioleisen Neutronensternen (grob) bestimmt worden. Demnach hat RX J0720.4-3125 eine Entfernung von  $250 \pm 25$  pc und RX J0806.4-4123 eine Entfernung von  $240 \pm 25$  pc.

Kandidatensuche Wie die Ergebnisse der Populationssynthesesimulationen zeigen, sind weitere Neutronensterne mit vorwiegend thermischer Röntgenemission am Himmel zu erwarten, allein in der RÖntgenSATelliten Himmelsdurchmusterung, dem ROSAT All Sky Survey (RASS), etwa noch einmal ebenso viele wie gegenwärtig bekannt. Das Problem bei ihrer Identifizierung sind die großen Röntgenpositionsfehler und die benötigten tiefen, optischen Beobachtungen. Zur (teilweisen) Lösung des letzteren Problems ist die neue optische Durchmusterung von etwa einem Viertel des Himmels, der Sloan Digital

Sky Survey (SDSS), in dieser Arbeit erstmals für die Kandidatensuche verwendet worden. Für die Röntgenquellen des RASS, deren Positionen im Bereich des SDSS liegen, führen sorgfältig gewählte Auswahlkriterien zu neun neuen Kandidaten für radioleise Neutronensterne. Diese werden gegenwärtig mit dem amerikanischen Röntgensatelliten Chandra nachbeobachtet. Für die Suche nach Kandidaten in tiefen ROSAT- oder XMM-Newton-Einzelbeobachtungen müssen die optischen, SDSS-basierten Auswahlkriterien weniger streng gewählt werden. Die hier überprüften Röntgenquellen sind deutlich schwächer als die RASS-Quellen, weswegen tiefere optische Beobachtungen nötig wären, um ähnlich hohe Flussverhältnisse wie für RASS/SDSS erreichen zu können. Die tiefen ROSAT- oder XMM-Newton-Einzelbeobachtungen haben jedoch den Vorteil von durchschnittlich kleineren Röntgenpositionsfehlern. Zusammen mit dem Kriterium eines weichen Röntgenspektrums können daher auch für die tiefen Einzelbeobachtungen insgesamt zwölf neue Neutronensternkandidaten identifiziert werden. Der Anteil von "Störquellen" in der Kandidatenliste, wie beispielsweise Aktiven Galaxien, ist vermutlich recht hoch, wenn man die Lage der Kandidaten am Himmel (hohe galaktische Breiten) und die Ergebnisse unserer Populationssynthese berücksichtigt. Nur mit Nachbeobachtungen im Optischen und bei Röntgen-Wellenlängen lässt sich die Kandidatenzahl weiter eingrenzen.

Für die Suche nach weichen Röntgenquellen in den XMM-Newton-Beobachtungen wurde erstmals das Verfahren von Dennerl et al. (2004) zur Berücksichtigung von Detektorenergien von 150 eV bis 200 eV konsequent angewandt. Dafür wurden außerdem bisher unberücksichtigte, auffällige Pixel in den Detektor-CCDs (Charge – Coupled Devices) gesucht und von der weiteren Analyse ausgeschlossen. Drei neue Neutronensternkandidaten (im SDSS-Himmelsbereich), die mit der Standardanalyse (ab 200 eV) nicht gefunden wurden, sind das Resultat dieser Berücksichtigung niedriger Detektorenergien. Es ist jedoch anzumerken, dass trotz deutlicher Rauschunterdrückung durch das Verfahren von Dennerl et al. (2004) in einigen Fällen Rauschstrukturen zurückbleiben, so dass dieses Verfahren nicht ohne anschließende genaue Überprüfung zur Identifizierung von weichen Röntgenquellen genutzt werden sollte.

Suche nach sub-stellaren Begleitern Seit Wolszczan & Frail (1992) die ersten Neutronensternplaneten durch Variationen in Radiopulssignalen entdeckt haben, stellt sich die Frage, ob es weitere sub-stellare Begleiter um Neutronensterne gibt und wie häufig Begleiter um Neutronensterne sind. In dieser Arbeit wird erstmals das Verfahren der direkten Abbildung im Nahen Infrarot (NIR) zur Suche nach warmen sub-stellaren Begleitern um junge, nahe Neutronensterne verwendet. Dies schließt auch zum ersten Mal radioleise Neutronensterne in die Begleitersuche ein. So gefundene sub-stellare Begleiter wären direkt weitergehend beobachtbar, beispielsweise durch Spektroskopie. Die durch die Radiopulsvariationen gefundenen Planeten können bisher nicht direkt beobachtet werden, da sie vermutlich zu alt und zu weit weg sind. Im Rahmen unseres langfristigen Projektes sind erste Beobachtungen für zehn Neutronensterne in dieser Arbeit dokumentiert, insbesondere möglicherweise interessante Begleiterkandidaten, ausgewählt nach NIR-optischen-Farbkriterien. Für alle Neutronensterne sind obere Grenzen der NIR-Helligkeiten bestimmt worden.

Zwei Neutronensterne haben eine ausreichend hohe Eigenbewegung, so dass bereits jeweils eine Wiederholungsbeobachtung analysiert werden konnte. Es wird keine gemeinsame Mitbewegung von detektierten Objekten mit den Neutronensternen festgestellt. Daher kann man für den radioleisen RX J1856.6-3754 sub-stellare Begleiter mit mehr als etwa 10 Jupitermassen ausschließen, wenn man ein Neutronensternalter von  $10^6$  a und eine Entfernung von 161 pc annimmt. Für PSR J1932+1059 (3.1 ·  $10^6$  a, 361 pc) können sehr wahrscheinlich sub-stellare Begleiter mit mehr als 52 Jupitermassen ausgeschlossen werden. Aufgrund großer instrumentenbedingter Fehler ist hier eine weitere Nachbeobachtung sinnvoll.

## Abstract

Most known neutron stars are radio pulsars, but there are also radio-quiet neutron stars with pure thermal X-ray emission. Their X-ray emission maximum is below 1 keV, thus they are soft X-ray sources. These radio-quiet neutron stars are of special interest because their thermal X-ray spectra are caused by photospheric emission – allowing a direct view onto the stars' surfaces – in contrast to the magnetospheric emission which is dominating in case of e.g. most of the radio pulsars. Only seven sources are known of this fascinating radio-quiet neutron star type. However, they represent about one fourth of the known neutron stars in the solar neighbourhood. How many more such neutron stars can one expect to find with current instruments and where? One part of this work deals with these questions – on the one hand by simulations predicting the observable number of neutron stars with strong thermal emission, on the other hand by a candidate search. The second part of this work is the search for substellar companions around young neutron stars.

**Population synthesis of young cooling neutron stars** This work investigates the performance of a population synthesis model which is based on several assumptions. Predictions are compared with the observed number of neutron stars for bright X-ray fluxes. The amount of detectable neutron stars with thermal emission is simulated for faint X-ray fluxes. Important questions in this work concern the influence of the distribution of the progenitor stars on the observable neutron star number and the role of an inhomogeneous distribution of the X-ray-absorbing interstellar medium (ISM). High-mass stars, the progenitors of neutron stars, are more frequent in OB or star associations. In this work, the higher probability for neutron star births in these associations is taken into account for the first time. As a consequence, young cooling neutron stars with thermal X-ray emission are concentrated towards the respective lines of sight in the sky. Absorption of X-rays in regions with especially dense ISM lead to lower detectable neutron star numbers there. Two 3D distributions of the ISM are developed, tested and applied in this work to consider a realistic absorption of the emitted soft X-ray spectra. One major ingredient is the 3D Natrium density cube by Lallement et al. (2003). One ISM model is furthermore based on stellar extinction measurements, the other one is an analytical ISM model. Both models reproduce relatively well the known observational properties of star clusters and a few neutron stars. They are well suited for statistical studies. However, they are large-scale models whose performances are insufficient towards small ISM structures, especially at large distances. A difference of roughly a factor of two is found for the predicted number of very faint neutron stars comparing the results applying both ISM-models. Thus, there is definitely room for improvement concerning realistic ISM models. For the first time the developed ISM models allow to estimate roughly the distances towards two of the seven known radio-quiet neutron stars with pure thermal X-ray spectra. Using both ISM distributions and the X-ray spectra of the neutron stars we get a distance of  $250 \pm 25$  pc in case of RX J0720.4-3125 and  $240 \pm 25$  pc for RX J0806.4-4123.

**Searching for new candidates** More neutron stars with strong thermal X-ray emission are expected. According to our population synthesis model one would expect, for example, twice as many sources as currently known down to typical fluxes reached in the ROSAT All Sky Survey (RASS). It is difficult to identify these X-ray sources because of large RASS positional errors and the deep optical observations needed. To overcome the latter problem, the recent *Sloan* Digital Sky Survey (SDSS), which covers around one fourth of the sky, is used in this work. Carefully chosen selection criteria lead to nine new radio-quiet neutron star RASS candidates in sky regions covered by the SDSS. There are on-going X-ray follow-up observations using *Chandra* for these sources. The selection criteria in case of the ROSAT and XMM-*Newton* pointings are less stringent compared to the RASS

candidates since the X-ray sources investigated in the pointings are much fainter than the RASS sources. Therefore, deeper optical observations are needed to reach an X-ray to optical flux ratio similar to the case of RASS and SDSS. However, the pointings usually provide better X-ray positions. Together with the criterion of a soft X-ray spectrum this leads to the identification of additional twelve new neutron star candidates. Due to the less stringent selection criteria a relatively large contribution of confusing sources (e.g. active galaxies) to the candidate list is expected given the candidate locations in the sky (high galactic latitudes) and taking into account the results of our population synthesis for these regions. Only by follow-up observations at optical and X-ray wavelengths one can constrain the candidate list further.

In the frame of our search for soft X-ray sources in deep XMM-Newton pointings, this work considers for the first time the low energies from 150 eV to 200 eV for a large set of observations. This is done following Dennerl et al. (2004) to correct for detector noise and wrong offsets, and by applying a dedicated bad pixel search resulting in exclusion of the bad pixels found. Three of the above mentioned twelve new neutron star candidates are the result. They are not found by the standard analysis (starting from 200 eV). Due to some remaining noise patterns one always has to visually inspect soft X-ray sources found after applying the method by Dennerl et al. (2004).

Searching for substellar companions around neutron stars When Wolszczan & Frail (1992) discovered the first pulsar planets by the radiopulse timing technique, the questions arose whether there are other substellar companions around neutron stars and how frequent they are. In this work we apply for the first time direct imaging in the near infrared (NIR) in order to search for young and thus still warm substellar companions around young nearby neutron stars. With this new method also radio-quiet neutron stars are included. Substellar companions found in this way can be directly investigated by follow-up observations. This is not possible in case of the known pulsar planetary systems because the planets found by the radiopulse timing technique are probably too old, too far away or too small. In the frame of our long-term project this work presents first NIR observations of ten neutron stars, in particular potentially interesting substellar companion candidates found by their NIR-optical colors. The neutron stars are undetected and the derived limiting NIR magnitudes are given. Since two objects have sufficiently large proper motions we succeeded in re-observing them and analysed these second epoch observations. No common proper motion is observed for any of the detected NIR objects. Therefore, one can exclude substellar companions heavier than  $\approx 10$  Jupiter masses in case of RX J1856.6-3754 if one assumes an age of the neutron star of 10<sup>6</sup> yrs and considers its distance to be 161 pc. Regarding the radio pulsar PSR J1932+1059 ( $3.1 \cdot 10^6$  yrs, 361 pc), there are probably no substellar companions heavier than 52 Jupiter masses. Here, the positional errors are too large for firm conclusions to be drawn, and follow-up observations would be useful.

# **C**ontents

| 1        | Intr | roduction  | 1  |
|----------|------|--|----|
| <b>2</b> | A s  | patially resolved population synthesis of young isolated neutron stars |    |
|          | (pai | tially published, Posselt et al. 2006, to appear in APSS)              | 11 |
|          | 2.1  | The neutron star progenitor distribution                               | 13 |
|          | 2.2  | The modified source flux   | 18 |
|          |      | 2.2.1 Minor new improvements in the flux treatment                     | 20 |
|          | 2.3  | The inhomogeneous interstellar medium                                  | 23 |
|          |      | 2.3.1 The ISM distribution used by Popov et al. (2005)                 | 25 |
|          |      | 2.3.2 Two new models of the ISM distribution                           | 27 |
|          | 2.4  | Fainter sources with XMM-Newton  | 40 |
|          | 2.5  | Conclusions  | 41 |
|          |      |  |    |
| 3        |      | rching for new X-ray thermal isolated neutron stars                    |    |
|          |      | <b>31</b> , (3)  | 43 |
|          | 3.1  | The ROSAT All Sky Survey   |    |
|          | 3.2  | The ROSAT pointed observations   |    |
|          |      | 3.2.1 ROSAT PSPC Pointings   |    |
|          |      | 3.2.2 ROSAT HRI Pointings  |    |
|          | 3.3  | XMM-Newton pointed observations  |    |
|          | 3.4  | Conclusions  | 88 |
| 4        | Sea  | rching for substellar companions to neutron stars                      |    |
| •        |      | tially published, Posselt et al. 2005, IAUC200)                        | 93 |
|          | 4.1  | Methods and sample selection   |    |
|          |      | 4.1.1 First epoch observations   |    |
|          |      | 4.1.2 Second epoch observation   |    |
|          | 4.2  | Observations and data reduction  |    |
|          |      | 4.2.1 First epoch observations   |    |
|          |      | 4.2.2 Second epoch observations  |    |
|          | 12   | First results  |    |

|              |       | 4.3.1 First epoch observations                   | )2           |
|--------------|-------|--|--------------|
|              |       | 4.3.2 Second epoch observations                  | 13           |
|              | 4.4   | Conclusions                                      | 18           |
| 5            | Sun   | nmary and Outlook 11                             | .9           |
|              | 5.1   | Summary  | 19           |
|              | 5.2   | Future Plans                                     | 22           |
| Bi           | bliog | graphy 12  | :5           |
| $\mathbf{A}$ | Tele  | escopes, instruments and data sources            | i            |
|              | A.1   | X-ray telescopes                                 | i            |
|              |       | A.1.1 ROSAT                                      | i            |
|              |       | A.1.2 XMM-Newton                                 | ii           |
|              |       | A.1.3 Chandra                                    | iii          |
|              | A.2   | Optical and Near Infrared Telescopes             |              |
|              |       | A.2.1 Very Large Telescope (VLT)                 | $\mathbf{V}$ |
|              |       | A.2.2 New Technology Telescope (NTT)             |              |
|              | A.3   | Data bases                                       |              |
|              |       | A.3.1 The Sloan Digital Sky Survey (SDSS)        | ⁄ii          |
|              |       | A.3.2 Further data bases                         | ⁄ii          |
| В            | Add   | litional figures to Chapter 2                    | i            |
| $\mathbf{C}$ | Add   | litional information about the Magnificent Seven | i            |
| D            | Add   | litional tables to Chapter 2                     | iii          |
| E            | Add   | litional tables to Chapter 3                     | $\mathbf{v}$ |

# **List of Figures**

| 1.1  | The $P$ - $\dot{P}$ Diagram   | 8  |
|------|---|----|
| 2.1  | The initial neutron star distribution   | 16 |
| 2.2  | The $\log N$ - $\log S$ curve – the new progenitor distribution                 | 17 |
| 2.3  | The influence of $N(H)$ , abundances and cross-sections                         |    |
| 2.4  | Effects of minor changes in the code  | 23 |
| 2.5  | Tbabs / wabs versus distance  | 23 |
| 2.6  | The $\log N$ - $\log S$ curve – different abundances and cross-sections         | 24 |
| 2.7  | The $\log N$ - $\log S$ curve – different ISM distributions                     | 24 |
| 2.8  | Galactocentric Hydrogen number density according to Bochkarev (1992) .          | 26 |
| 2.9  | The limits of the Ferlet et al. (1985) formula to derive $N(H)$                 | 28 |
| 2.10 | The analytical model at 1 kpc   | 30 |
| 2.11 | The extinction model at 1 kpc   | 30 |
| 2.12 | Testing with open cluster data (1)  | 31 |
| 2.13 | Testing with open cluster data $(2)$  | 31 |
|      | The NS distribution for $r_{GB} = 500 \text{ pc} \dots \dots \dots \dots \dots$ | 38 |
| 2.15 | The NS distribution for the new progenitor distribution                         | 38 |
| 2.16 | The NS distribution if using $tbabs$  | 38 |
| 2.17 | The NS distribution for the analytical ISM model                                | 38 |
| 2.18 | The NS distribution for the ISM model based on Hakkila et al. $(1997)$          | 38 |
| 2.19 | The expected neutron star number density  | 39 |
| 2.20 | The $\log N$ - $\log S$ curve for XMM EPIC-pn                                   | 41 |
| 3.1  | The SDSS images of the RASS candidates (1)                                      | 49 |
| 3.2  | The SDSS images of the RASS candidates (2)                                      |    |
| 3.3  | Candidate RASS positions on the sky   | 53 |
| 3.4  | Sky coverage of SDSS DR5 and ROSAT pointings                                    | 55 |
| 3.5  | ROSAT images of the PSPC candidate  | 59 |
| 3.6  | ROSAT candidate fields in SDSS (1)  | 59 |
| 3.7  | ROSAT images of the HRI candidates  | 65 |
| 3.8  | XMM-Newton images of the HRI candidates   | 66 |
| 3.9  | ROSAT candidate fields in the SDSS (2)  | 67 |

| 3.10 | The X-ray images of the XMM-Newton candidates (1) 80                     | ) |
|------|--|---|
| 3.11 | The X-ray images of the XMM-Newton candidates (2) 81                     | L |
| 3.12 | The X-ray images of the XMM-Newton candidates (3) 82                     | 2 |
| 3.13 | The X-ray images of the XMM-Newton candidates (4) 83                     | 3 |
| 3.14 | The X-ray images of the XMM-Newton candidates (5)                        | 1 |
|      | The X-ray images of the XMM-Newton candidates (6)                        | ó |
|      | XMM-Newton candidate fields in the SDSS (1)                              | 3 |
|      | XMM-Newton candidate fields in the SDSS (2)                              | 7 |
|      | Pointing candidate positions on the sky                                  | ) |
|      |  |   |
| 4.1  | Bolometric luminosities of substellar companions                         | ; |
| 4.2  | H-band limits (1)  | ) |
| 4.3  | H-band limit (2)   | ) |
| 4.4  | Interesting NIR-objects  | L |
| 4.5  | Interesting NIR-objects (2)  | 2 |
| 4.6  | Differences between SOFI and ISAAC positions                             | 3 |
| 4.7  | Harmonizing the pixel scales of $ISAAC$ and $SOFI$ observations 114      | 1 |
| 4.8  | Pixel shifts between $ISAAC$ and $SOFI$ positions for PSR J1932+1059 116 | 3 |
|      |  |   |
| A.1  | Effective areas of different X-ray satellites iv                         | Ţ |
| В.1  | Cooling curves for model I by Popov et al. (2006a) is                    | ; |
|      | Locations of the OB associations by de Zeeuw et al. (1999) is            |   |
| D.Z  | Locations of the OD associations by the Zeeth et al. (1999)              | 1 |
|      |  |   |

# **List of Tables**

| 2.1 | The used OB associations and assumed age ranges             |
|-----|---|
| 2.2 | Testing the ISM models for individual objects               |
| 2.3 | Distances obtained for the Magnificent Seven                |
| 3.1 | The 11 RASS candidate INS fields                            |
| 3.2 | The PSPC candidate  |
| 3.3 | The HRI candidates  |
| 3.4 | XMM candidates  |
| 4.1 | NIR Results   |
| 4.2 | Coordinates and box sizes used in Fig. 4.2 and 4.3          |
| C.1 | X-ray and optical properties of the Magnificent Seven ii    |
| C.2 | Magnetic field estimates for the Magnificent Seven ii       |
| D.1 | The used 36 star associations outside a 400 pc iii          |
| E.1 | HRI hardness ratios for five of the M7                      |
| E.2 | Hardness ratios of the Magnificent Seven                    |
| E.3 | SSC2 hardness ratios of the Magnificent Seven vi            |
| E.4 | Bad Pixels for XMM-Newton EPIC-pn at energies $< 200eV$ vii |

# Chapter 1

## Introduction

The variety of astrophysical objects identified today as neutron stars (NS) was certainly not expected when Baade & Zwicky (1934) first had the idea of a neutron star as the end product of a supernova. Today, one observes neutron stars as objects powered by their rotational energy, by gravitational energy via accretion from binary companions, or by thermal energy via cooling of the hot stellar interior. Bursts from accreting sources are powered by nuclear energy. For the so-called magnetars it is suspected that the observed high luminosities, especially in super-bursts, are due to huge magnetic fields. Most neutron stars are solitary objects, but some are companions to low- or high-mass stars, and even to other neutron stars. These double neutron star systems are particularly interesting for studying general-relativity effects. Equally fascinating are the two known planetary systems around neutron stars.

In the following, we briefly summarize the spectral characteristics of the NS types known today. The spectra of neutron stars allow one to distinguish between NS populations, as we discuss in greater detail later. This thesis concentrates on the one hand on the group of isolated NSs emitting thermally at X-ray wavelengths as well as on the other hand on possible planetary mass or brown dwarf companions to neutron stars. These main emphases are discussed and motivated at the end of the introduction.

#### Multi-wavelength astrophysics of neutron stars

The first neutron stars were discovered by J. Bell and A. Hewish in the 1960s as radio pulsars (Hewish et al., 1968), and radio pulsations are still the main characteristic observation feature of most known neutron stars. The radio emission is a coherent emission process and has its origin in the magnetosphere of the pulsar. The shape of the observed radio pulse is determined e.g. by the viewing geometry of these relativistic objects, especially the viewing angle with respect to the angle between the rotational axis and the axis of the magnetic field, which is assumed to first approximation to be a dipole field. For a detailed discussion of the radio emission properties of NSs we refer to Lorimer & Kramer

(2004). The observed radio periods, P, and the period derivatives,  $\dot{P}$ , are used to form the most important diagram in neutron star astronomy - the P- $\dot{P}$  diagram, which is plotted in Fig. 1.1 (in Appendix). Shown in the diagram are also lines of constant magnetic field strength and characteristic age, which are deduced from P and  $\dot{P}$  by assuming that the loss of rotational energy is due to (vacuum) magnetic dipole radiation.

While roughly 1600 radio pulsars are known, the number of X-ray detections is much smaller (around 4\%, ignoring millisecond(ms)-pulsars, whose X-ray detections are due to accretion from binaries) and we know only a handful of Gamma-ray pulsars (e.g. Manchester et al. 2005, Becker & Pavlov 2002). The X-ray and Gamma-ray detected neutron stars are indicated in the  $P-\dot{P}$  diagram (Fig. 1.1). The neutron stars showing high-energy emission usually experience a large loss of rotational energy. One distinguishes between magnetospheric emission and photospheric emission in the observed spectra of neutron stars, e.g. at X-ray wavelengths. The emission properties of NSs can be summarized as follows, for an detailed overview we refer to Lyne & Graham-Smith (2005) or Michel (1991). Photospheric emission has its origin on the star's cooling surface or on its hot polar caps. The polar caps are either heated by the interior of the neutron star (e.g. Greenstein & Hartke, 1983) or by bombardment from magnetospheric particles (e.g. Helfand et al., 1980). Blackbody-like spectral components indicate the presence of photospheric emission. The photospheric emission can be observed primarily in soft X-rays, in some objects also at optical wavelengths. Magnetospheric emission, observed primarily in the radio, X-ray and Gamma-ray ranges, has its origin in highly relativistic charged particles accelerated by the magnetic field of the neutron star. Synchrotron radiation or, more generally, curvature radiation is responsible for the observed power law(s) of the magnetospheric emission. For most of the known neutron stars the magnetospheric emission outshines the photospheric emission, especially in case of the X-ray emission. Neutron stars are best observed at high energies and radio wavelengths. They are very faint in the optical and in the infrared.

#### Neutron star populations

It is assumed that there are around 10<sup>9</sup> neutron stars in our galaxy, most of them old objects. However, this assumption, which is based on the supernova rate and the metallicity of the interstellar medium (Tammann et al., 1994, Arnett et al., 1989), is difficult to verify. About 10<sup>6</sup> of the objects are expected to be 'active' neutron stars in the sense that they emit in the radio or in X-rays (Lorimer & Kramer, 2004). However, even the observed radio pulsar population, which is the largest set of known NSs, is highly incomplete (e.g. Lorimer 2004). The effects of the interstellar medium (ISM) are key in understanding selection effects. At radio wavelengths, the most important processes are the dispersion of the pulse, pulse scattering and interstellar scintillation (Lorimer & Kramer, 2004). At X-ray wavelengths, the ISM's most important effect is absorption.

Most neutron stars are isolated objects due to their violent birth, when they receive large kick velocities. Only 4% of them are bound in binary systems (Lorimer, 2005), a significant reduction in comparison to the high rate of binarity among main-sequence stars. Ms-pulsars are exceptional relative to most NSs: they are spun-up by the consumption of

material from their binary companions and 80% are in binary systems (Lorimer, 2005). With 'isolated' neutron stars (INSs), we mean in the following those NSs without stellar companions. Sub-stellar (planetary-mass and brown-dwarf) companions usually cannot be excluded observationally.

For detailed reviews about isolated neutron stars in general, we refer to Kaspi et al. (2004) and Becker & Pavlov (2002) and summarize here only the main sub-populations. Most known isolated neutron stars are radio pulsars. As noted above, we currently know roughly 1600 of them (Manchester et al., 2005), and some are also detected in the X-ray, optical, or Gamma-ray wavelength regime. In addition, there are a few isolated neutron stars without strong radio emission. Usually one refers to these objects as radio-quiet. Radio-quiescence can be explained by an unfavorable viewing geometry of the radio beam or indeed by the absence or near absence of radio emission from the neutron star. For example, the five so-called 'Central Compact Objects' in supernova remnants are not detected at radio wavelengths. Another example is the Gamma-ray pulsar Geminga, for which the claimed weak radio detection by Malofeev & Malov (1997) is still without confirmation. Radio-quietness is also reported in the case of the seven ROSAT-detected neutron stars, often called the 'Magnificent Seven'. The Magnificent Seven are peculiar because they have pure thermal soft X-ray spectra without any (confirmed) non-thermal emission. When they were discovered, it was suspected that they may belong to the population of 're-activated' old neutron stars accreting from the ISM. Thousands of such NSs were expected before the launch of ROSAT (e.g. Ostriker et al. 1970, Blaes & Madau 1993). The Magnificent Seven with their blackbody-like X-ray spectra are one of the foci of this thesis and will be discussed in more detail below.

There is another class of suspected isolated neutron stars – the so-called magnetars. Anomalous X-ray pulsars (AXPs) and Soft Gamma Repeater (SGRs) have too high X-ray luminosities to be powered *only* by the loss of rotational energy. The eight known AXPs are soft X-ray sources with long pulse periods, and they are rapidly spinning down. The four known SGRs differ from the AXPs by their huge bursts at soft Gamma- and X-rays. For more details about AXPs and SGRs we refer to Woods & Thompson (2004). The commonly preferred model for these objects is that of magnetars, i.e. neutron stars with extremely large magnetic fields ( $\approx 10^{15}$  G). It was proposed as explanation by Paczynski (1992) and Duncan & Thompson (1992). A competing model is based on accretion disks (e.g. Ertan et al. 2006, van Paradijs et al. 1995); it can explain all the properties of the AXPs and SGRs except the observed super-bursts.

McLaughlin et al. (2006) recently discovered the new class of Rotational Radio Transients (RRATs). These sources emit single radio pulses from time to time instead of the steady pulsations one knows from the ordinary radio pulsars. Not much is known about this new

class, but McLaughlin et al. (2006) estimated that there may be twice as many RRATs as ordinary radio pulsars. The recent discovery of RRATs suggests that the NS menagerie may be even more diverse than is currently realized. The questions concerning the origin of the differences among the NS populations or the possible evolutionary connections between these populations are current topics of NS research and play a key role in our overall understanding of neutron stars.

#### The Magnificent Seven

Given the fact that of the 24 known neutron stars within 400 pc (Manchester et al. 2005) 1), seven are ROSAT-discovered NSs with pure thermal emission, one can conclude that Magnificent Seven (M7)-like objects represent a significant fraction of the local neutron star population. First, it was thought that the M7 may be some of the long-sought old neutron stars accreting from the ISM. Since then, however, measurements of their proper motions, combined with the determination of their probable birthplaces, and the longand short-term stability of their X-ray spectra (with the exception of the freely precessing RX J0720.4-3125, Haberl et al. 2006) indicate that these sources are most likely cooling neutron stars with an age of less than 2 Myrs. The thousands of old isolated NSs which are re-activated by accretion from the ISM have not yet been found in contrast to the earlier expectations. It is commonly believed today that the numbers predicted by e.g. Blaes & Madau (1993), Zane et al. (1995) or Paczynski (1990) were overestimated because the NSs are moving faster than assumed earlier (Arzoumanian et al., 2002, Hobbs et al., 2005) and the Bondi-Hoyle accretion rate scales with the inverse cube of the stellar velocity. Further reductions of the accretion rate are expected if the magnetic fields in the material to be accreted or propeller effects are taken into account (e.g. Perna et al., 2003). The inefficiency of the Bondi-Hoyle accretion explains the discrepancy between the absent old, ISM-accreting neutron stars and the ealier predictions. Furthermore, Bondi-Hoyle accretion cannot be responsible for the majority of the Magnificent Seven.

As mentioned earlier, there are no confident detections of non-thermal emission from any of the M7. Instead, all these objects have blackbody-like X-ray spectra; they are radio-quiet (but note Malofeev et al. 2006, 2005). Their soft blackbody-like X-ray spectra are likely to be due to polar caps either heated by the neutron star interior or by accelerated (non-thermal) particles in the magnetosphere. Magnetospheric heating of the M7's polar caps was favoured by e.g. Kaspi et al. (2004). A new magnetic field model by Geppert et al. (2004, 2005), including toroidal magnetic fields in addition to dipole fields, predicts hot polar caps of different sizes heated by the NS interior. A contribution of magnetospheric particles is not necessary.

Kaspi et al. (2004) suspected that the lack of non-thermal emission is due to an

<sup>&</sup>lt;sup>1</sup>http://www.atnf.csiro.au/research/pulsar/psrcat/

unfavorable viewing geometry where the (radio) beams do not intersect with the observer's lines of sight. The long periods of the pulsating neutron stars result in narrow radio beams which are more difficult to detect, see e.g. a statistical study by Tauris & Manchester (1998). Thus, only  $\approx 3\%$  of pulsars with M7-like periods are expected to be observable at radio wavelengths. There is one radio pulsar within 400 pc, PSR J2144-3933, which has a period (8.5 s) similar to those found in the M7. In summary, the absence of radio emission is consistent with the theoretical expectations, but no further conclusions can be made in this context given the small numbers (the M7 plus one source).

No supernova remnant is detected around any M7 member. The optically identified objects among the M7 show an optical excess of a factor of 5 to 14 with respect to the extrapolated X-ray spectrum. Five of the M7 pulsate in their X-ray fluxes with relatively long periods comparable to those of magnetars. The period histories of two of the M7 were studied by Kaplan & van Kerkwijk (2005a,b). The derived period P and period derivatives  $\dot{P}$  result in magnetic fields of around 10<sup>13</sup> G, if a magnetic dipole field is assumed. In addition to high velocities these large magnetic fields may hinder accretion from the ISM (long ejector stage, e.g. Treves et al. 2000). Five of the M7 show absorption features in their thermal X-ray spectrum which may be explained in terms of proton cyclotron lines (e.g. Haberl 2006), atomic lines of strongly magnetized Hydrogen or Helium (e.g. van Kerkwijk & Kaplan 2006) or lines of molecules which exist at sufficiently high magnetic fields and low temperatures (Turbiner, 2006). In either case the required magnetic field strengths are of the order of  $10^{13}$  G. This is in rough agreement with the magnetic fields derived by Kaplan & van Kerkwijk (2005a,b). Once a line has been found which can be unambiguously identified with an atomic line, one could determine the NS's surface gravity, and thereby obtain its mass. However, the unambiguous identification of the lines is unlikely in the near future for neutron stars with such strong magnetic fields like those of the M7. The main difficulty for the calculation of synthetic spectra and their comparison to the observations is the necessary exact knowledge about the distributions of the magnetic field and temperature which are clearly model-dependent (J. Trümper, personal communication; see also Harding & Lai 2006, Zane & Turolla 2006).

Because of the direct view one has onto the surfaces of the M7 it was thought it would be possible to study NS atmospheres. However, the absorption lines are currently not very good tracers of atmospheres due to the ambiguity of possible interpretations. Furthermore, the brightest object, RX J1856.5-3754, is very puzzling. Despite long X-ray integrations at high spectral resolution, it was not possible to find any deviation from a blackbody (e.g. Burwitz et al. 2003). The X-ray spectrum of RX J1856.5-3754 is the second best determined blackbody in astrophysics after the cosmic background radiation. It is a remarkable source which also does not show any X-ray pulsations, which may be

due to a special viewing geometry. There are several ideas to explain an object like RX J1856.5-3754. We mention here only one promising option, namely the possibility of a condensed atmosphere in solid or liquid form as was discussed by Burwitz et al. (2003) and van Adelsberg et al. (2005).

Overall, the Magnificent Seven are peculiar neutron stars and of great interest given their proximity and the undisturbed view onto their surfaces.

#### Why do we need more Magnificent Seven like neutron stars?

Observations of the Magnificent Seven offer the possibility to measure NS radii which are important – in addition to NS masses – to constrain the equation of state of matter at supra-nuclear densities. There is no neutron star with radius and mass determinations up to now. However, the wealth of possible theoretical equations of state can already be constrained by considering results from nuclear collision experiments and other (indirect) observational data as e.g. burst oscillations of accreting neutron stars in binaries (for more details see Trümper 2006). While NS masses have been studied in binaries and are determined very accurately in double NS sytems (see e.g. Lorimer 2005), radius estimations remain rare. We note here the possibility of deriving NS masses also by Keplerian motion of possible sub-stellar companions, which is especially interesting for isolated objects like the M7. Concerning the lack of well determined NS radii, the M7 are of special interest because their photospheric emission allows a direct radius estimation. This is quite difficult in case of e.g. radio pulsars because the magnetospheric emission outshines the thermal emission from the surface. The Magnificent Seven are not the only NSs with a strong thermal X-ray component from the surface. Other examples are the Gamma-ray pulsar Geminga, the Central Compact Objects such as the one in Cassiopeia A and the young radio pulsar Vela. None of the latter, however, can provide a comparably undisturbed, direct view onto the surface due to additional magnetospheric emission. An other advantage of the M7 is their proximity and the well determined parallactic distance to RX J1856.5-3754 (Walter & Lattimer 2002, note also van Kerkwijk & Kaplan 2006). Thus, the radius determination of this star is the best we currently have for neutron stars (e.g. Trümper et al. 2004) and suggests larger neutron star radii than previously thought. Together with other constraints this radius implies a rather stiff equation of state for the neutron stars (Trümper, 2006). The equation of state is not the only interesting subject in the investigation of the M7. Further questions include those about the structure and composition of neutron star surfaces as mentioned above.

Unfortunately, the M7 are far from fully understood. The seven objects are rather diverse considering details of their X-ray spectra or their pulsations. Seven objects are too few to disentangle the influence of various parameters like the viewing geometry, magnetic fields or atmospheres. As noted above, these neutron stars represent a significant fraction

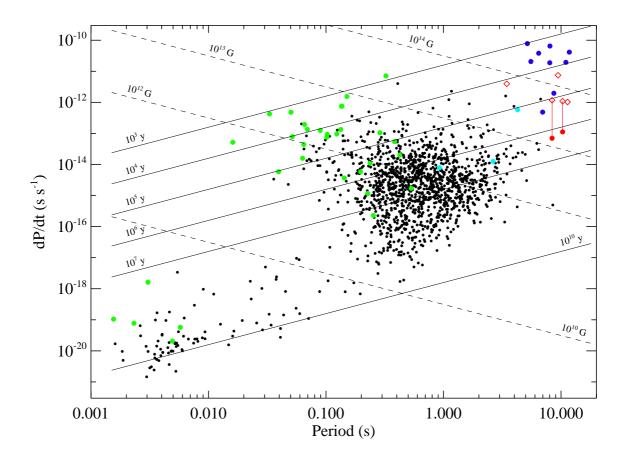


Figure 1.1: The P- $\dot{P}$  Diagram

The known pulsating neutron stars are placed into the diagram according to their pulse period P and period derivative  $\dot{P}$ . Black dots correspond to the radio pulsars, the green dots are neutron stars which are also detected in X-rays or Gamma-rays (incomplete for ms-pulsars). The blue dots mark the AXPs and SGRs. The three cyan dots correspond to the Rotational Radio Transients with known  $\dot{P}$ . The red dots show the direct measurements of  $P, \dot{P}$  for RX J0720.4-3125 and RBS 1223 (for assumed magnetic dipoles), while the open diamonds represent the  $\dot{P}$  values expected from magnetic field estimates assuming proton resonance as origin of the absorption lines. The diamonds and dots are connected by a line in case of RX J0720.4-3125 and RBS 1223.

Based on Fig. 8 by Haberl (2006)

of the local NS population. According to the results by Kaplan & van Kerkwijk (2005a,b) and the absorption line interpretation, four of the seven can be included in the  $P-\dot{P}$  diagram which is plotted in Fig. 1.1. The four M7 members with obtained P,  $\dot{P}$  lie away from the bulk of ordinary radio pulsars, close to the magnetar candidates, AXPs

and SGRs. The three RRATs with known P and  $\dot{P}$  are scattered between them and the ordinary pulsars. The positions in the P -  $\dot{P}$  diagram gave rise to speculations about possible connections or evolution between the different neutron star populations (e.g. Popov et al. 2006b, Guseinov et al. 2005). However, the current small numbers of M7-like objects and RRATs do not allow unambiguous conclusions. For example, we may observe only a local enhancement of M7-like objects due to the close birthplaces in the Gould Belt, whose importance was shown by Popov et al. (2000b).

In summary, the detection of new M7-like objects would be very important for a better understanding of neutron star physics. By searching for neutron stars with soft X-ray spectra and without radio emission one may finally find one of the rare old neutron stars which are slow enough to accrete from the ISM.

Many searches for new X-ray thermal NSs have been carried out, e.g. by Chieregato et al. (2005), Rutledge et al. (2003), Danner (1998a,b). None of them has resulted in any new confirmed candidate up to now. The searches suffered mainly from large X-ray error boxes and the lack of deep optical observations. In Chapter 2 we simulate the number of expected observable NSs with thermal X-ray emission. In Chapter 3 we describe our search strategy to overcome the mentioned observational problems and present several new M7-like candidates.

#### Sub-stellar companions around neutron stars

Up to now only radio pulsars have been searched for planetary companions by the radio pulse timing technique, which is most sensitive to close companions in case of ms-pulsars. Unexpectedly, two planetary systems around ms-pulsars have been found (Wolszczan & Frail, 1992, Sigurdsson et al., 2003). The discovery of the first extra-solar Earth-mass objects around PSR 1257+12 was one of the numerous surprises in the investigation of neutron stars. Different scenarios have been developed to explain these two pulsar planetary systems. Among them are the supernova survival scenario, the fallback disk model, the circumbinary disk model, the disrupted companion model or the planet scavenging model (see Podsiadlowski (1995) for a detailed discussion). If the planets form from the disk created after the supernova, the planet formation is likely to be different from the same process in proto-stellar disks. Thus, the study of neutron star planetary systems in comparison to those around solar-like or other main-sequence stars can be very fruitful for understanding planet formation in general. Furthermore, one may get valuable insights into the supernova event itself, as well as into the composition and the final stages of the progenitor stars. Obtaining the NS mass by Keplerian motion of sub-stellar companions is another interesting possibility, especially for NSs without stellar companions like the Magnificent Seven.

Apart from indirect detections at radio wavelengths, the known pulsar planets are not de-

tectable with current instruments in the optical or at other wavelengths. Thus, no further investigations can be done currently and discovering new - directly observable - planets would be useful. This is the motivation for our search for new sub-stellar companions around NSs (Chapter 4). We note that currently there is no brown dwarf companion known around a NS.

#### Outline of the thesis

With the help of population synthesis we investigate in Chapter 2 whether the currently observed number of NSs with strong thermal X-ray emission agrees with the one predicted by theoretical assumptions and models. We concentrate especially on the influence of interstellar absorption on the soft X-ray spectra and on the local NS progenitor distribution. Both are important in predicting the most likely sky regions in which to find X-ray thermal NSs. As a by-product we estimate distances towards two of the Magnificent Seven with hitherto unknown distances.

In Chapter 3, we present our new search for M7-like NSs applying for the first time all deep ROSAT pointed observations, deep XMM-Newton EPIC-pn observations in combination with the optical Sloan Digital Sky Survey. In the case of the XMM-Newton observations we consider lower detector energies than usually applied for source detections. Several candidates are presented and discussed together with problems one is facing for faint X-ray candidates.

In Chapter 4, we present our search for sub-stellar companions around young nearby neutron stars, which includes also the Magnificent Seven. For two NSs with high proper motion, PSR J1932+1059 and RX J1856.5-3754, the recently obtained second epoch observations and implications for possible sub-stellar companions are discussed. Additionally, near infrared limits have been derived for all the ten NSs with first epoch observations. Each chapter has its own short introduction and conclusions. An overall summary and outlook is given in Chapter 5.

# Chapter 2

# A spatially resolved population synthesis of young nearby isolated neutron stars

(partially published, Posselt et al. 2006, to appear in Astrophysics and Space Science)

Despite many searches for new Magnificent Seven (M7)-like objects by e.g. Agüeros et al. (2006), Chieregato et al. (2005), Rutledge et al. (2003) there is no confirmed new candidate of a X-ray thermal neutron star up to now. One possibility for better understanding this neutron star population and its distribution within the Galaxy is by population synthesis. This method simulates the expected number of neutron stars for given theoretical and observational constraints. The correspondence of the predictions with the actual observed number can also be seen as a test whether the theoretical models assumed are realistic. For example, Popov et al. (2006a) used their population synthesis model to test different sets of cooling curves. It is in principle possible to exclude very unlikely models. Caution has to be taken in claiming one particular model as the 'real' one. On the one hand, there are many uncertainties in the various theoretical assumptions besides the investigated one. On the other hand, there is only a small number of neutron stars with which to constrain the model. Thus, one cannot exclude selection effects. However, population synthesis is a very useful tool to get a feeling about our current knowledge of the evolution of neutron stars as well as to derive predictions of the expected observable neutron star number, especially for observations with new instruments.

The population synthesis model of NSs with strong thermal emission discussed here is a derivative of the one by Popov et al. (2000b), further developed by Popov et al. (2003) and Popov et al. (2005). The general picture is that the neutron stars are born with an initial inhomogeneous spatial distribution, having a mass spectrum and expected inital temperatures. They receive a kick velocity and their further motion is influenced by

the Galactic gravitational field. They cool down according to cooling curves which are dependent on their mass and composition. The X-ray surface emission of these neutron stars is modified by absorption in the interstellar medium. Finally, how many we can detect depends on the sensitivity of the observing instrument. For a detailed description we refer to Popov et al. (2000b, 2003, 2005). Here we summarize only the main physical ingredients, which enter their latest population synthesis model (Popov et al., 2005).

- The initial spatial distribution of the NSs was derived randomly from the infinitesimal thin disks of the Gould Belt and the Milky Way, scaled with the expected correspondent birthrates there.
- The kick velocities were chosen according to the double-Maxwellian distribution by Arzoumanian et al. (2002)
- The NS mass spectrum was derived by models from Timmes et al. (1996), Woosley et al. (2002). For these models one needs to consider the progenitor masses which can be derived roughly from spectral types.
- The gravitational potential of the Milky Way was treated following Paczynski (1990) with bulge, disk and halo components. The galactic bar which extends to a galactocentric distance of maximal 3.5 kpc (e.g. Pichardo et al., 2004) is neglected because its influence is very small for the relatively nearby objecs we are interested in.
- The cooling curves Popov et al. (2005) applied are those of Kaminker et al. (2002) for hybrid stars. We note here the later work by Popov et al. (2006a) dealing especially with a large representative set of cooling curves calculated with different assumptions. From Popov et al. (2006a) we adapt a set of cooling curves for further usage in this work. More precisely we use 'model I' by Popov et al. (2006a) in the following (see also Fig. B.1 in the Appendix). It considers only hadronic matter and was noted as the best model regarding the tests Popov et al. (2006a) applied. This model uses cooling curves by Blaschke et al. (2004).
- The surface emission was assumed to be blackbody radiation as only thermal emission is considered. Popov et al. (2005) investigated also the effect of reduced emissivity by mimicking it with a radiation radius being around one third of the actual neutron star radius.
- The interstellar absorption was taken into account by an analytical model for the hydrogen density. We discuss the absorption treatment extensively in Sec. 2.2 and 2.3.

• The observing instrument was ROSAT's position sensitive proportional counter (PSPC), which was used for the ROSAT All Sky Survey.

At the end the  $\log N$ - $\log S$  curve is obtained. It is the expected number N of observable neutron stars brighter than a given X-ray flux S. In the following, we use S for the count rate measured with ROSAT. For all following subsections we note that we use the same velocity distribution and gravitational potential as taken by Popov et al. (2005). The mass spectrum is the same as in Popov et al. (2006a) and the cooling curves correspond to those marked as model I in Popov et al. (2006a). Only blackbody emission is considered (more details below). In this work we report significant improvements of the population synthesis model considering the initial progenitor distribution (Sec. 2.1) and the absorption treatment (Sec. 2.2). In particular, a more realistic model for the ISM distribution (Sec. 2.3) is investigated. Minor improvements in the program code are noted in Sec. 2.2.1. The results are discussed in the individual subsections, including one improvement after the other in the population synthesis. Conclusions are drawn at the end of the chapter.

The project is done in cooperation with S.B. Popov (Sternberg Astronomical Institute, Moscow).

## 2.1 The neutron star progenitor distribution

Popov et al. (2003) considered for the first time not only the Galactic disk but also the Gould Belt for neutron star births. They showed that the population of the nearby neutron stars with strong thermal emission is genetically related to the Gould Belt.

| OB association            | Age   |
|---------------------------|-------|
| Upper Scorpius            | 4-6   |
| Upper Centaurus Lupus     | 12-14 |
| Lower Centaurus Crux      | 9-11  |
| Vel OB2                   | 6-10  |
| Trumpler 10               | 15-30 |
| Collinder 121             | 4-6   |
| Per OB2                   | 3-7   |
| $\alpha$ Persei (Per OB3) | 25-50 |
| Cas-Tau                   | 25-50 |
| Lac OB1                   | 2-25  |
| Cep OB2                   | 5-10  |
| Cep OB6                   | 25-50 |

**Table 2.1:** The used OB associations and assumed age ranges in Myrs.

The Gould Belt (see Pöppel (1997, 2001) for a detailed description of the Belt structure) was reported to have a supernova rate of 20-25 per Myr according to Grenier (2000). According to Tammann et al. (1994) this rate represents 2/3 of the new born neutron stars within 0.6 kpc around the Sun. This fits well to the result by Torra et al. (2000), who estimated that about 2/3 of the massive stars within 0.6 kpc around the Sun belong to the Gould Belt. Popov et al. (2003) scaled this birthrate to the number of neutron stars born at random positions within a ring-shaped Gould Belt, which was

modeled as an infinitesimal thin disk. Popov et al. (2003) took into account a birthrate of 250 per Myr for the contribution of newborn neutron stars in the Galactic plane within Solar distances of 3 kpc, following Tammann et al. (1994). The birthplaces of the neutron stars in the Galactic plane were modeled again as randomly distributed positions in an infinitesimal thin disk. In reality the OB associations as the most likely birthplaces are not equally scattered through the Gould Belt. This is also true for possible progenitors in the Galactic disk. Therefore we improve the progenitor distribution in the following way:

Up to the Hipparcos limit of 400 pc (ESA, 1997) the known B2-O8 stars are considered individually as well as their affiliation to an OB association (de Zeeuw et al. 1999; see also Fig. B.2 in the Appendix) resulting in birth properties depending on the age of the OB association (see Table 2.1). We can roughly estimate the mass of each star as we know its spectral type. The stellar mass gives us an idea about the lifetime of the star. If we have no other information about the possible age of a star then we assume that its probability of exploding just depends on its full lifetime. The probability is inversly proportional to the lifetime of a star with the lightest star living the longest time. The mass interval corresponding to each spectral class can be converted to the approximate limiting lifetimes:  $T_{LM}$  is the longest lifetime for the lowest mass, and  $T_{HM}$  is the shortest lifetime for the high mass end of the particular mass interval. If the star is known to belong to an OB association, we also consider the age of the OB association. The ages of the OB associations in Table 2.1, which are taken from the discussion in de Zeeuw et al. (1999), are not well determined. We artificially added an uncertainty if de Zeeuw et al. (1999) provided just one number as an estimate (for example, if the age is given  $\sim 13$  Myr we assume the range 12-14 Myr). By this we have with  $TL_{OB}$  and  $TU_{OB}$  a lower and upper age limit for the OB association, respectively. If  $T_{HM} > TU_{OB}$ , then the probability of a star exploding is 0, as the shortest estimated lifetime is longer than the age of the OB association

If oppositely  $T_{LM} < TL_{OB}$  then the probability is inversly proportional to the longest liftime,  $T_{LM}$ , of the star. This probability is also used in the field within 400 pc distances, if the star is not related to an OB association.

If  $T_{HM} < TL_{OB}$  but  $T_{LM} > TU_{OB}$  then the probability is inversly proportional to  $(TU_{OB} - TL_{OB})$  as one has to consider overlapping time scales as more likely for the massive stars giving births to neutron stars.

If  $T_{HM} < TL_{OB}$  and  $TL_{OB} < T_{LM} < TU_{OB}$  then the probability of exploding is inversly proportional to  $(T_{LM} - TL_{OB})$ .

If  $TL_{OB} < T_{HM} < TU_{OB}$  and  $T_{LM} > TU_{OB}$  then the probability is inversly proportional to  $(TU_{OB} - T_{HM})$ .

If  $TL_{OB} < T_{HM}$ , but  $T_{LM} < TU_{OB}$  then the probability of exploding is set inversly proportional to the minimum time value  $(T_{LM} - T_{HM})_{MIN}$ , which was found for the mass intervall of spectral type B0, [15 M $_{\odot}$ , 18 M $_{\odot}$ ].  $(T_{LM} - T_{HM})_{MIN}$  is 1.44 Myrs. As normalisation the probability  $\propto 1/1.44$  Myr is set to one. The supernova rate of all possible progenitors within 400 pc are normalised to the birth rate of 25 neutron stars per Myr.

For distances larger than 400 pc we distinguish between two possibilities for neutron star births: 20 NSs per Myr are supposed to be born inside the Galactic disc at distances father than 400 pc, but closer than 3 kpc, from the Sun. Their positions in the disc are calculated randomly. The disc is exponential both in R and z with a z-scale of 100 pc and a radial scale of 3 kpc.

Most (225 per Myr) of the neutron stars, however, are born in one of 36 star associations (table. D.1). The data are taken from the catalogs by Blaha & Humphreys (1989) and Mel'nik & Efremov (1995). Note that the distances to the associations are reduced (the distances given by Blaha & Humphreys (1989) are multiplied by 0.8) according to Dambis et al. (2001). The ages and sizes of these associations are poorly known. We assume spheres with a radius of 100 pc for each association. Neutron stars are born randomly within these spheres. The birth probability is set to be proportional to the number of stars in each cluster. We hereby assume that the number of stars with known photometry (Nt in the Table D.1 in the Appendix) roughly reflects the total number of stars in the cluster. An overview of the whole initial progenitor distribution is plotted in Fig. 2.1

In the log N-log S curves in Fig. 2.2, and in the Galactic maps of predicted NS number density (Fig. 2.15 versus Fig. 2.14 on page ??) the effect of the improved progenitor distribution is shown. The same mass spectrum, cooling curves (model I of Popov et al. (2006a) for hadron stars) as well as the same absorption models are used for comparison. The new log N-log S curve in Fig. 2.2 lies in-between those of the two Gould Belt sizes (with outer radius,  $r_{out}$ , of 300 pc or 500 pc), which is reasonable. However, the separation relative to the measured integrated number of objects is larger than in the case of a  $r_{out} = 500$  pc Gould Belt. The difference is largest for bright objects. While in principle it is possible that neutron stars are missed by the observations, this seems to be rather unlikely for bright objects. As the log N-log S curve does not fit well the observations at the bright end, one has to conclude that other parameters (e.g. masses, cooling curves or absorption) of the population synthesis are not optimal and have to be adapted. At the faint end, the small number of currently known sources certainly underestimates the real neutron star number. Correspondance with the simulated result can be regarded only as fullfilling a lower limit condition. We note here that in addition one would need

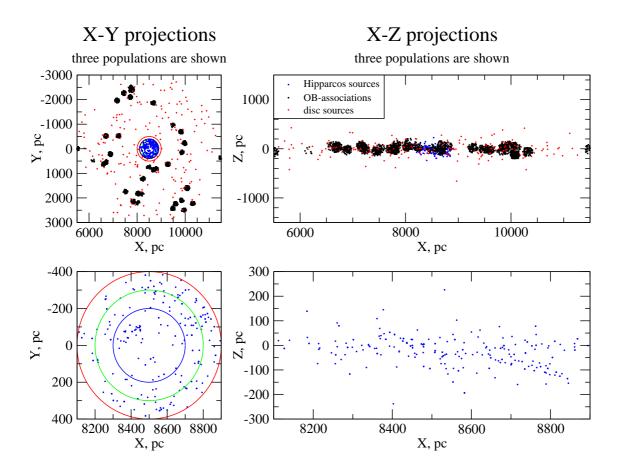
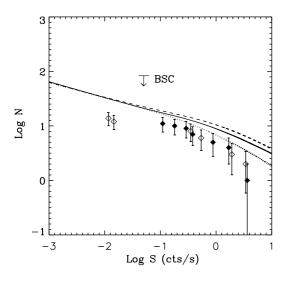


Figure 2.1: The initial neutron star distribution

Shown are plane projections in cartesian Galactic coordinates with the Galactic center at (0,0,0), x pointing to  $l=180^{\circ}$ , y pointing to  $l=90^{\circ}$ , z pointing to the north Galactic pole. The black dots represent the neutron stars born in the 36 associations. The blue dots correspond to the neutron stars inside 400 pc. The red dots show the neutron stars in the disc (400 pc < d < 3000 pc). The circles in the left images are at 200 pc (blue), 300 pc (green) and 400 pc (red).

to consider at the faint end of the simulations those neutron stars, whose thermal X-ray emission is below the non-thermal X-ray emission. Otherwise we overpredict the neutron star number as we consider a birthrate, which is suspected to be that of the whole neutron star population. If we consider the local young neutron star population, the neutron stars emitting strong thermal X-ray emission represent more than half of this population. Therefore one would expect that for the faintest objects the possible overestimation error cannot be larger than a factor of two. Generally one can see in

Fig. 2.2 a less steep behaviour of all  $\log N$ - $\log S$  curves towards lower count rates. As discussed already by Popov et al. (2003), this is the influence of the Gould Belt causing a 'bump' in the result one would get from the Galactic disk alone. One could have expected that nearby large OB associations like Upp Sco would result in similar, but smaller structures in the number counts. However, the simulations do not show such an effect. But there is an effect of the new progenitor distribution – in the expected locations of neutron stars in the sky. Popov et al. (2005) showed a Galactic map of the projected distribution of cooling isolated neutron stars as a by-product. We replot a comparable result in Fig. 2.14 (on page 38). The only difference to the simulation done for Fig. 6 by Popov et al. (2005) is that the minor changes in the absorption treatment (integration mechanism, energy range) have been applied, see Sec. 2.2.1. One can compare Fig. 2.14 with the new Fig. 2.15 for our improved population synthesis model. We note that these images are currently only by-products of the simulations. The 'traces' which one sees in the illustrations are due to statistical reasons: Once a neutron star is born, count rates are 'measured' during the whole simulation for this particular neutron star. A 'trace' corresponds to the motion of the neutron star, which usually starts from close to the Galactic plane. As the born neutron stars are scaled with the supernova rate, this is correct in the case of the  $\log N$ - $\log S$  curve, for which the statistics are improved comparing to simulations done in the same computational time but without following one neutron star along its way. For a statistically well sampled Galactic map without 'traces' we would need much more simulations, thus computational time. However, these Galactic maps provide a good overview of areas of e.g. especially high numbers of expected neutron



**Figure 2.2:** The figure shows the expected number N of neutron stars at ROSAT PSPC count rates S. The symbols correspond to the Magnificent Seven (black filled diamonds) and six other neutron stars with relatively strong thermal X-ray emission as summarised in Popov et al. (2003). Poissonian errors are plotted for the observational points only as the statistical noise of the computed curves is low due to the simulated large number of neutron stars. 'BSC' stands for Bright Source catalogue and is a limit found for ROSAT data by Rutledge et al. (2003). The  $\log N$ - $\log S$  curve of the new progenitor distribution (solid line) lies in between the result for a Gould Belt with a radius  $r_{out}$  of 500 pc (dotted line) or  $r_{out} = 300$  pc (dashed line). All others parameters are the same, especially the ISM distribution and the absorption treatment.

stars. Individual 'traces' should not be compared. While in the old simulated neutron star distribution there was a strong concentration in the whole Galactic plane, this is not the case for the new one. In the old simulation there is a tilt visible for the dense part of the distribution of the predicted NS number. This tilt is due to the applied Gould Belt disk. With the new progenitor distribution there are some individual regions of enhanced neutron star density. For example, the enhancement at  $l \approx 200^{\circ}$  to  $250^{\circ}$ ,  $b \approx 0^{\circ}$  to  $-30^{\circ}$  is probably caused by the Ori OB association. Another one at  $l \approx 270^{\circ}$  to 350°,  $b \approx -10^{\circ}$  to 20° is very likely related to Upper Scorpius, Upper Centaurus Lupus and Lower Centaurus Crux, the three neighbouring OB associations of the Gould Belt which are closest to us (de Zeeuw et al., 1999). Other regions of more expected neutron stars are at  $l \approx 100^{\circ}$ and at  $l \approx 140^{\circ}$  (both very roughly at  $b \approx 0^{\circ}$ ). The first one is probably caused by the progenitors in the Cepheus OB2 association, the latter could be related to the  $\alpha$  Persei OB association. At  $l \approx 20^{\circ}$  to  $50^{\circ}$ ,  $b \approx 0^{\circ}$  the expected density of neutron stars is lower in the case of the new progenitor distribution when compared to the old simple Gould Belt model. At this Galactic longitudes there are no reported close OB associations, see e.g. Fig. 29 of de Zeeuw et al. (1999), shown in the Appendix as Fig. B.2.

#### 2.2 The modified source flux

The X-ray flux from a source is usually measured in terms of a count rate CR (counts per sec) in an instrument in response to the X-ray flux. The instrument specific sensitivity at a frequency  $\nu$  is expressed by the so-called effective area  $A(\nu)$ . Additionally, one has to consider the interstellar absorption for the measured flux. It is usually described by a factor  $e^{-[\sigma_{ISM}(\nu)N(H)]}$  where N(H) is the total hydrogen column number density measured in particles cm<sup>-2</sup>.  $\sigma_{ISM}$  is the total photoionization cross-section and a sum of  $\sigma_{gas}$ ,  $\sigma_{molecules}$ , and  $\sigma_{grains}$ . The count rate CR, which is measured in a frequency range  $[\nu_1, \nu_2]$ , can therefore be described as:

$$CR = \int_{\nu_1}^{\nu_2} A(\nu) \cdot e^{-[\sigma_{ISM}(\nu)N(H)]} \cdot \frac{F_{\nu}}{h\nu} \cdot \frac{4\pi R^2}{4\pi D^2} \cdot d\nu, \tag{2.1}$$

where h is the Planck constant,  $F_{\nu}$  is the flux density, which is emitted by the object's surface  $4\pi R^2$ , and is scaled by its distance D. For a relativistic object like a neutron star one has to consider that the measurements are at a wide distance from the neutron star. Therefore R corresponds to the apparent radius  $R_{\infty}$ , which is related to the true neutron

star radius  $R_{NS}$  and the Schwarzschild radius  $R_S$  by:

$$R_{\infty} = \frac{R_{NS}}{\sqrt{1 - R_S/R_{NS}}},\tag{2.2}$$

where  $R_S = G \cdot M_{NS}c^{-2}$  with G the gravitational constant,  $M_{NS}$  the mass of the neutron star and c the velocity of light. Furthermore,  $F_{\nu}/(h\nu)$  is actually  $F_{\nu_{\infty}}/(h\nu_{\infty})$ .

Together with equation 2.1 and the transformation  $E_{\infty} = h\nu_{\infty}$  we get:

$$CR = \int_{E_1}^{E_2} A(E_{\infty}) \cdot e^{-[\sigma_{ISM}(E_{\infty}) \cdot N(H)]} \cdot \frac{F_{E_{\infty}}}{E_{\infty}} \cdot \frac{R_{\infty}^2}{D^2} \cdot \frac{1}{h} \cdot dE_{\infty}, \tag{2.3}$$

We consider here only the thermal radiation of a neutron star. The thermal radiation can be described as blackbody radiation. This assumption is well supported by the measured blackbody-like spectra of the Magnificent Seven. We neglect here possible atmospheres or hot spots. The first are poorly understood, and may not be present for all neutron stars. For example, RX J1856.6-3754 has a blackbody spectrum that is the second best determined one after the microwave background spectrum. Hot spots may be of interest in future improvements of the population synthesis. However, this will need further initial assumptions about e.g. the birth magnetic fields. Therefore we restrict ourselves here to the flux density of a blackbody which can be described at infinity by:

$$F_{\nu_{\infty}} = \int_{0}^{2\pi} d\phi \int_{0}^{\frac{\pi}{2}} d\theta \cos\theta \cdot \frac{2h}{c^{2}} \cdot \frac{\nu_{\infty}^{3}}{\exp\left[(h\nu_{\infty})/(kT_{\infty}]\right) - 1} = \frac{2h\pi}{c^{2}} \cdot \frac{\nu_{\infty}^{3}}{\exp\left[(h\nu_{\infty})/(kT_{\infty})\right] - 1},$$
(2.4)

where k is the Boltzmann constant and c the speed of light. Applying again  $E_{\infty} = h\nu_{\infty}$  we derive from equation 2.3:

$$CR = \int_{E_1}^{E_2} A(E_{\infty}) \cdot e^{-[\sigma_{ISM}(E_{\infty}) \cdot N(H)]} \cdot \frac{R_{NS}^2}{(1 - \frac{R_S}{R_{NS}})D^2} \cdot \frac{2\pi}{c^2 h^3} \cdot \frac{E_{\infty}^2}{\exp\left[E_{\infty}/(kT_{\infty})\right] - 1} dE_{\infty}$$
 (2.5)

 $A(E_{\infty})$  and  $e^{-[\sigma_{ISM}(E_{\infty})\cdot N(H)]}$  in equation 2.5 are known by discrete measurements and averaged over small energy intervals  $\Delta E_i$ . For these individual energy intervals they can be then treated as constant factors. In the program code by Popov et al. (2003) the integral in equation 2.5 was solved numerically by a Gaussian integration mechanism with 50 mesh points.

#### 2.2.1 Minor new improvements in the flux treatment

In the following we outline some of the minor technical improvements in the code. First, we changed the integration to a Newtonian integration, making individual accuracy adaption more flexible. The integration is done in NP steps of  $\Delta E_i = i \cdot (E_2 - E_1)/NP$ . The integrand is taken at the center of each energy interval, thus at  $E_i = E_1 + i \cdot (\Delta E_i)/2$ .

After several tests we adapted NP = 300 as the best compromise between accuracy and computational time. It also gives better results than the earlier Gaussian integration. The energy range considered by Popov et al. (2003) was 0.08 keV to 3 keV for the obtained ROSAT PSPC count rates. To compare with the ROSAT All Sky Survey (RASS) one has to consider exactly the same energy range as was done in the data analysis of the RASS. Therefore, we changed the energy range to 0.1 keV to 2 keV. The effective area of the intrument is highly inhomogeneously sampled due to the sharp instrumental absorption edges in the energy band of interest. In the program code by Popov et al. (2003) the effective area was derived only at the fifty energy points of the Gaussian integration, taken at two points  $\pm 1eV$  around each energy point. This can be highly unprecise by chance, at e.g. absorption edges. We consider therefore all measurement points of the effective area file within the energy intervals  $\Delta E_i$ . All effective areas at the base points within  $\triangle E_i$  are averaged to obtain  $A(\triangle E_i)$ . Besides, one has also to consider that the effective area is a function of the off-axis angle. An average effective area, which involves an average vignetting, represents the observation parameters of the All Sky Survey better. This is taken into account in our effective areas. The combined effect of these minor improvements in the population synthesis flux treatment can be seen in Fig. 2.4. Plotted are the flux differences versus distances of the simulated neutron stars. During simulations we found that the effect of Gaussian or Newtonian integration alone is small, so that the overall differences are due mainly to the changed energy range and better sampling of the ROSAT effective areas. The large changes of up to 40% at low distances are probably due to the adapted effective area calculation in the new routine. Especially at soft energies, which are best seen at low distances, there are edges in the instrument response function.

The absorption is considered in equation 2.1 by the term  $e^{-[\sigma_{ISM}(\nu)\cdot N(H)]}$ . The column density N(H) is dependent on the distribution of the interstellar medium (ISM), which is discussed in detail in Section 2.3. The principal influence of N(H) on the overall absorption, however, can be seen in Fig. 2.3. The sum of the photoionization cross-sections,  $\sigma_{ISM}(\nu)$ , is influenced by the individual photoionization cross-sections of the elements and their ions as well as by dust grain properties. Thus, the abundances of the elements are important considering the absorption. The relevance of abundances to the interpretation of X-ray spectra is also illustrated in Fig. 2.3. Nearly every absorption model presumes the same abundances of elements independent of the direction of sight.

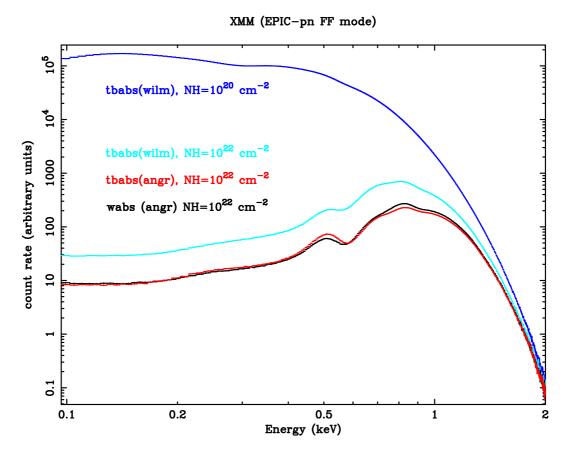


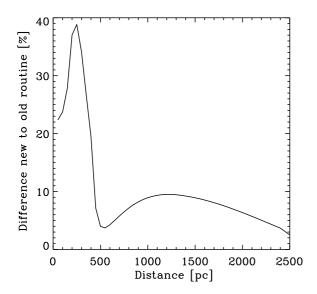
Figure 2.3: The influence of column densities, abundances and cross-sections
The XSPEC routines wabs and tbabs simulate the interstellar absorption on a X-ray spectrum, here for a 90 eV blackbody. The abundances tables used are indicated by (wilm) if abundances of Wilms et al. (2000), and (angr) if the abundances of Anders & Grevesse (1989) are used. The instrument is XMM EPIC PN in full frame mode. The count rate given is arbitrary as a normalisation of 1 was applied. The influence of the interstellar absorption is apparent at higher hydrogen column densities NH comparing the blue with the cyan curve. Both curves are obtained using the abundances of Wilms et al. (2000) for tbabs. The routine tbabs is also applied to simulate the red curve, but now with the abundances of Anders & Grevesse (1989). There is nearly no difference to the wabs routine (black curve) which uses other cross-sections but the same abundance table. See also text in Section 2.2.1 for discussion.

It was outlined by Wilms et al. (2000) that the total gas plus dust ISM abundances are lower than the local – Solar – abundances and the general ISM abundance uncertainties are still in the order of 0.1 dex because measurements are very difficult. One can choose between several different abundance tables implemented e.g. in XSPEC for analysing X-ray spectra. We note here only two examples commonly used – the abundance tables by Anders & Grevesse (1989) ('angr' in XSPEC) and Wilms et al. (2000) ('wilm' in

XSPEC) considering newer measurements by e.g. Snow & Witt (1996), Cardelli et al. (1996), Meyer et al. (1997, 1998). One apparent difference between 'angr' and 'wilm' is the Oxygen abundance, which differs by a factor of two, influencing strongly the absorption below the Oxygen edge at around 530 eV. Thus, in case of the lower 'wilm' abundance nearly a factor of 2 more N(H) is required to result in a similar attenuation at low energies (see e.g. Fig. 2.3).

As already noted the individual abundances and photoionization cross-sections of the elements and their ions influence the total photoionization cross-section as well as dust grain properties (e.g. sizes, shapes). Considering the models of the photoionization cross-sections we mention here only two example works used very often for analysis of X-ray spectra. Morrison & McCammon (1983) did a polynominial fit of the effective absorption cross-section per hydrogen atom based on measured atomic absorption crosssections by Henke et al. (1982) and abundances mostly from Anders & Ebihara (1982). With the exception of oxygen Morrison & McCammon (1983) assumed the elements to be either entirely in the gas phase or completely depleted into dust grains. A recent improved absorption treatment by Wilms et al. (2000) takes into account newer element abundances as noted above and more recent photoionization cross-section calculations by e.g. Verner et al. (1993), Verner & Yakovlev (1995). Wilms et al. (2000) included additionally an improved molecular cross-section for  $H_2$ . Besides this updated database Wilms et al. (2000) considered furthermore a simple spherical composite dust grain model in a MRN distribution (Mathis et al., 1977). The composition is represented by actually measured depletion factors: the ratio between the gas phase abundance and the total abundance of an element. Both models are implemented in XSPEC and can be used via the routines 'wabs' (Morrison & McCammon, 1983) or 'tbabs' (Wilms et al., 2000). The various absorption descriptions can lead to differing results (see Fig. 2.3 and also Fig. 2.5) or expectations of e.g. observable object numbers. The differences caused by the diverse treatments show our incomplete knowledge about the interstellar absorption and should be kept in mind, especially for soft X-ray spectra.

For comparisons in the following discussions we use either the tbabs-routine together with the abundance table 'wilm' or the wabs-routine together with the abundance table 'angr', which was used by Popov et al. (2005) before. The difference is small between tbabs(wilm) and wabs(angr) for the overall result of the population synthesis, see Fig. 2.6. There is also no obvious difference in the obtained Galactic maps of expected neutron stars as can be seen by comparing Fig. 2.15 and Fig. 2.16 We adapt in our improved final model the XSPEC routine tbabs and the abundance table 'wilm'.



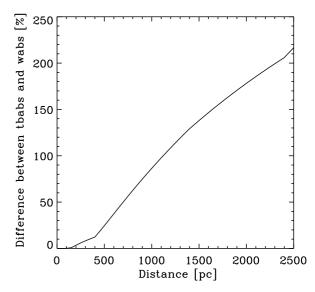


Figure 2.4: The effect of integration mechanism and energy range on the absorption on soft X-ray sources

Figure 2.5: The effect of different abundances & cross-sections on the absorption on soft X-ray sources

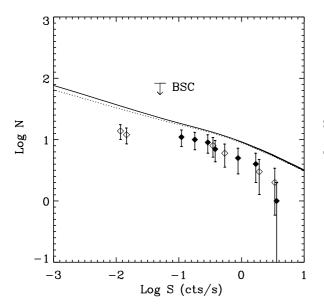
**Description of the figures:** The differences are calculated for the same neutron star parameters (blackbody of 90 eV, 11.67 km radius, and 1.48 Solar masses) at different distances. The Galactic coordinate x varies from 50 to 2500 pc in the direction from the Sun towards the Galactic center, y is always 0, z is 25 pc north . We applied the same interstellar medium distribution as that used by Popov et al. (2000b), which is described in more detail below.

In Fig. 2.4 we compare the absorbed fluxes produced by the old program code with those derived by the new code, which includes the new Newtonian integration, the RASS energy range and adaptive effective area consideration. The effect is small, see also text. The old abundances and cross-sections of Morrison & McCammon (1983) are used in both routines.

In Fig. 2.5 the differences are plotted for the absorbed fluxes obtained by the two XSPEC routines 'tbabs' and 'wabs'. For descriptions of the routines and discussion see text. As can be seen the effect of less absorption by the use of the newer routine 'tbabs' is stronger at larger distances, an effect due to larger column densities.

#### 2.3 The inhomogeneous interstellar medium

In X-ray astronomy with low spectroscopic resolution the chosen abundances and crosssections of the heavy elements are taken to transform the interstellar absorption, which actually is mainly caused by the heavy elements, to an equivalent hydrogen column den-



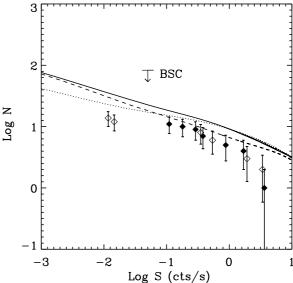


Figure 2.6:

The solid line represents the resulting  $\log N$ - $\log S$  curve if applying the absorption routine tbabs(wilm), the dotted line stands for applying the routine wabs(angr) as e.g. Popov et al. (2005) did. Both simulations are done with the new progenitor distribution. All other parameters are the same as for Fig. 2.2. In particular, the same ISM distribution was used as in Popov et al. (2005). For description of axes and symbols see also Fig. 2.2; for discussion see Sec. 2.2.1.

Figure 2.7: The  $\log N$ - $\log S$  curves using the old analytical ISM model as applied by e.g. Popov et al. (2005) (solid line), the improved analytical ISM model (dotted line) and the ISM model based on the extinction study by Hakkila et al. (1997) (dashed line). The absorption routine tbabs(wilm) and the new progenitor distribution are applied. All other parameters as well as axes and symbols are the same as for Fig. 2.2, see Sec. 2.3 for details.

sity. Cold and warm H-atoms (H I ) as well as hydrogen molecules and ionized hydrogen (H II ) contribute to the overall amount of hydrogen along a line of sight. These different components of the hydrogen column density are estimated by different measurement methods, e.g. various extinction measurements as summarized by Knude (2002) or radio 21-cm observations of hydrogen, namely (H I ), as the extensive study by Dickey & Lockman (1990) and more recently by Kalberla et al. (2005). A wealth of theoretical models of the ISM has been applied to these observations. However, most of them are only 2D models with some more recent exceptions (see e.g. Drimmel et al. (2003), Amôres & Lépine (2005) or Marshall et al. (2006) for 3D models). The overall result is a highly inhomogeneously distributed interstellar medium within the Milky Way, present in bubbles with loops or

dense rims, and shaped by molecular clouds, supernova explosions and stellar activity (for an illustrated overview see Henbest & Couper 1994). The ISM distribution is best known in the close Solar neighbourhood, especially in the Local Bubble (e.g. Breitschwerdt 1998). The most detailed view is provided by the study of Lallement et al. (2003), who measured Na I absorption towards 1005 sightlines to stars with Hipparcos distances up to 350 pc from the Sun; for more details on the measurements and the applied density inversion method see Lallement et al. (2003), the precursor paper Sfeir et al. (1999), and Vergely et al. (2001). Nai is regarded as good tracer of the total amount of the neutral interstellar gas and the sodium column density is thought to be convertable into a hydrogen column density (e.g. Ferlet et al. (1985), but see also discussion below). For more distant regions the determination of a 3D-distribution of the ISM is hampered mainly by the unknown or imprecise distances of the measured objects and the lack of a well-sampled grid of measurement points. This is true for all extinction-related methods to our knowledge and results in much more coarse sampling compared to the Solar neighbourhood. The results obtained by the various methods can differ for the same regions and a combination can be difficult. These difficulties result partly from the different observed astrophysical phenomena like measuring the dust emission or stellar magnitudes. They also result from different sets of stellar absolute magnitude calibrations and the underlying assumptions which can deviate from each other as interstellar extinction determination is an iterative process coupled with the identification of the statistical properties of stars (Hakkila et al., 1997).

# 2.3.1 The ISM distribution used by Popov et al. (2005)

Popov et al. (2005) applied an analytical ISM distribution model, which they first used and described in Popov et al. (2000b). It is based on the formulae by Zane et al. (1995), Dickey & Lockman (1990), de Boer (1991), but included a galactocentric radius dependency for the number density of atomic and molecular hydrogen as estimated by Bochkarev (1992). The model of hydrogen densities applied by Popov et al. (2005) is described in the following. First, the very small contribution of the ionized hydrogen to the total density can be neglected as mentioned by Zane et al. (1995). Thus, the total hydrogen density  $n_H$  is  $n_H = 2n_{H_2} + n_{HI}$ . The individual densities of H I and H<sub>2</sub> are taken into account by:

$$n_{HI} = n_1 \exp(-\frac{z^2}{2\sigma_1^2}) + n_2 \exp(-\frac{z^2}{2\sigma_2^2}) + n_3 \exp(-\frac{z}{h_1}), \quad n_{H_2} = n_4 \exp(-\frac{z}{h_2})$$
 (2.6)

where  $\sigma_1 = 212 \text{ pc}^1$ ,  $\sigma_2 = 530 \text{ pc}^1$ ,  $h_1 = 403 \text{ pc}$ ,  $h_2 = 70 \text{ pc}$  (Zane et al., 1995, Dickey & Lockman, 1990, de Boer, 1991). Popov et al. (2000b) changed the constant number densities  $n_1$  to  $n_4$  by including a galactocentric radius dependency for the number density of atomic and molecular hydrogen as shown, for example, by Bochkarev (1992) (see Fig. 2.8).

Popov et al. (2000b) transformed the  $n_{HI}^i(r_i)$  reported by Bochkarev (1992) at discrete radii  $r_i$  (representing the middle of a radius interval i) to the  $n_1, n_2$ , and  $n_3$  from above

<sup>&</sup>lt;sup>1</sup>Please note that actually these are FWHM values, the variances are  $\sigma_1 = 212/2.35482$  pc and  $\sigma_2 = 530/2.35482$  pc. This is corrected in subsequent versions of the new absorption model

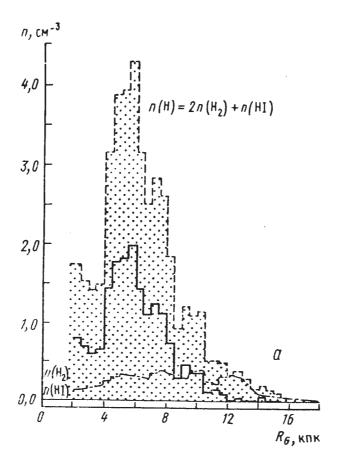


Figure 2.8: Galactocentric Hydrogen number density according to Bochkarev (1992) The x-axis corresponds to radii from the galactic center in kpc. The y-axis corresponds to the number density in particles per cm<sup>-3</sup>. Shown are the atomar Hydrogen number density n(HI), the molecular Hydrogen number density  $n(H_2)$ , and the number density of both together n(H). The number densities are averaged over all directions from the galactic center.

by applying:

$$n_1 = 0.7 n_{HI}^i(r_i), \quad n_2 = 0.19 n_{HI}^i(r_i), \quad n_3 = 0.11 n_{HI}^i(r_i), \quad n_4 = n_{H_2}(r_i)$$
 (2.7)

Zane et al. (1995) noted that equation 2.6 is only applicable at galactocentric radii of 3.4 kpc to 8.5 kpc. In the outer Galaxy the scale height of the gas layer expands linearly to 2 kpc. For galactocentric radii r (in kpc) larger than 8.5 kpc Popov et al. (2000b) consequently applied:

$$n_{HI} = n_{HI}^{i}(r_i) \exp(-\frac{z^2}{2(\sigma_2 r/8.5 kpc)^2}), \quad n_{H_2} = n_{H_2}^{i}(r_i) \exp(-\frac{z}{h_2})$$
 (2.8)

by considering only the largest scale of equation 2.6 for H I. Popov et al. (2005) modified the model reported by Zane et al. (1995), Dickey & Lockman (1990) not only by taking into account radius dependency, but also by considering ecpecially the close Solar vicinity. The Local Bubble is treated as a sphere of 140 pc radius having a constant low density of 0.1 particles cm<sup>-3</sup>. However, the interstellar medium is so inhomogeneously distributed that the hydrogen densities cannot be treated in the same manner for a given galactocentric radius but different lines of sight. This is the main weakness of the analytical ISM model used by Popov et al. (2005) and its precursor papers.

## 2.3.2 Two new models of the ISM distribution

The dependence of the hydrogen column density N(H) on the line of sight can already be seen in the local Solar neighbourhood, where the Local Bubble is surrounded inhomogeneously by the ISM. It is especially important to consider these local inhomogenities if one is interested in the local population of soft X-ray emitting neutron stars. The two 3D-distribution models of the ISM, which we discuss in the following, take into account the best currently available database of the local ISM distribution – the result by Lallement et al. (2003).

R. Lallement kindly provided us with the sodium density cube derived using the inversion method developed by Vergely et al. (2001). Due to the smoothing length of 25 pc applied in this method by Lallement et al. (2003), structures smaller than 25 pc cannot be resolved. We note further that even if measurements go up to Hipparcos distances of 350 pc from the Sun, the sampling becomes coarser at larger distances. Thus the sodium density cube has a span of only 250 pc and starting from 200 pc one has to be careful dealing eventually with the a priori density information applied in the inversion method

(R. Lallement, personal communication).

From the NaI density cube we calculate the column density for the same grid (sampling 3.9 pc). This is then converted to H I column density applying the formula by Ferlet et al. (1985).

It has to be mentioned that there are ongoing discussions about how well the sodium D-line absorption actually traces H<sub>I</sub>. The correlation found between the H<sub>I</sub> and Na column densities derived from Na-D absorption lines by Ferlet et al. (1985) was doubted by Welty et al. (1994), especially for low column densities (log N(NaI) < 11). The region of the Lallement cube that should not be used because it has such low column densities is indicated in Fig. 2.9. However, the lowest known X-ray-measured hydrogen column density for one of the M7 converts to a sodium column density of  $\log N(NaI) > 11.5$ (applying the formula by Ferlet et al. 1985). Therefore this low-column density uncertainty is not important considering the M7 and negligible for the intended population synthesis with neutron stars at usually larger distances.

Vergely et al. (2001) could not always find a correlation of the NaI density with the H I density. They concluded that the correlation is rather weak due to non-constant population ratios for interstellar medium species, thus different abundances. Lallement et al. (2003) noted the size of the Local Bubble revealed by H I is smaller than when derived by NaI. This was explained by the first ionization stage of NaI being below that of H I, resulting in a longer neutral phase of H I (Lallement et al., 2003).

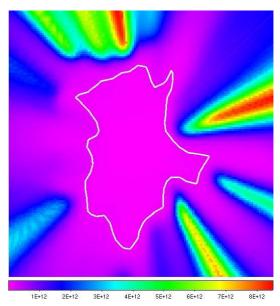


Figure 2.9: The limits of using the Ferlet et al. (1985) formula

The sodium column density as derived from the density data by Lallement et al. (2003) is shown in Galactic cartesian coordinates at z=0; x is towards the center which is at the right, y toward l=90° is pointing up. The image spans 500 pc times 500 pc. The area within the contour has low column densities (log N(NaI) < 11) for which Welty et al. (1994) doubted whether the Ferlet et al. (1985) formula is applicable. This region of small sodium column densities is largest at z=0 and becomes smaller for lower or larger z.

Recently, Hunter et al. (2006) found indications that the correlation between the NaI and H I column densities is different if one uses NaI UV transitions instead of the D-lines. They argue that there is an underestimation of approximately 30 % of N(H) in the case of NaI D-lines observations. Recapitulating, one has to be aware of the still not completely

solved problems concerning the conversion of NaI to HI column densities when it comes to interpreting individual results. However, we regard the measurements by Lallement et al. (2003) and the conversion to a hydrogen column density according to Ferlet et al. (1985) as the best possibility at hand to take into account the local inhomogenity in the ISM for X-ray astronomy with low spectral resolution.

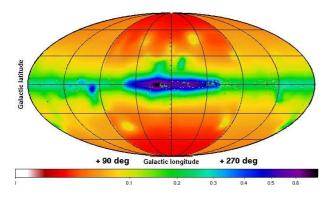
At distances larger than 230 pc we consider two different 3D models – one is the analytical model by Popov et al. (2005) and another one is based completely on extinction measurements. In the analytical model, the formulae from Sec. 2.3.1 are applied for distances above 230 pc. As noted above, there are other more recent theoretical 3D extinction models. However, the analytical H density model by Popov et al. (2000b, 2005) seems to be at least as good as e.g. the underlying model used by Amôres & Lépine (2005). The model of Drimmel et al. (2003) cannot be applied to distances less than a few hundred parsecs in the Solar neighbourhood and the data of Marshall et al. (2006) has a coarse sampling with distance bins of 1 kpc.

The second 3D ISM distribution model is based on the work of Hakkila et al. (1997). Hakkila et al. (1997) put several extinction studies carefully together in an easily accessible routine. All studies have been modified to statistically account for unsampled regions. Additionally, a correction method for the systematic underestimation between 1 and 5 kpc was developed. Errors were provided individually for each considered main survey and for their mean. The often large mean error values illustrate the disagreeing individual observing results. The model by Hakkila et al. (1997) is a large scale model, capable of identifying e.g. molecular clouds at intermediate distances, but not sensitive to extinction variations on scales of less than 1 degree. It is well suited for statistical studies.

Both ISM models are applied only for distances larger than 230 pc in case they provide an N(H) larger than derived from the sodium cube at 230 pc. Otherwise the hydrogen column density at 230 pc is taken since the column density can only increase with distance. We use spherical coordinates – the Galactic coordinates l, b and distance d. The nominal sampling is one degree in l and b, and 10 pc for the distance. This is technically motivated and does not represent the actually achieved accuracy. Distances are covered up to 4500 pc.

## Testing the models and further improvements

To test our models we first consider a relatively large number of test objects with well known distances and extinction measurements, not necessarily determined from X-rays. Then we proceed to a few of the rare neutron stars with well known distances, having also small error bars for the absorbing N(H) derived by X-ray observations.



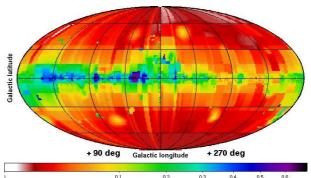


Figure 2.10: The N(H) predicted by the analytical model at 1 kpc

The Galactic map is in Mollweide projection. Positive Galactic latitudes are up and  $l=0^{\circ}$  is in the center. The N(H) is in units of  $10^{22} \mathrm{cm}^{-2}$ . For description of the model and discussion see text.

Figure 2.11: The N(H) predicted by the extinction model at 1kpc

The Galactic map is in Mollweide projection. Positive Galactic latitudes are up and  $l=0^{\circ}$  is in the center. The N(H) is in units of  $10^{22} {\rm cm}^{-2}$ . For description of the model and discussion see text.

As Hakkila et al. (1997) noted, different extinction studies do not agree precisely with each other due to the various applied methods or objects studied. The latter are usually very coarsely scattered and measurement errors can influence the extinction values of a large region. One possibility to overcome this problem is investigating open clusters. An open cluster has the advantage that one can measure a number of stars at approximately the same distance, which is usually well known. Therefore, open clusters are a good choice in aiming to minimize the extinction measurement errors along one line of sight. Usually one measures the reddening E(B-V). We concentrate here on the recent comprehensive reddening measurements for 650 open clusters by Piskunov et al. (2006), representing a complete sample up to distances of about 850 pc from the Sun. Details about this open cluster study can be found in Piskunov et al. (2006), Kharchenko et al. (2005b,a). To convert the reddening E(B-V) we apply the formula by Paresce (1984):  $N(H) = 5.5 \times 10^{-5}$  $10^{21}E(B-V)$  [cm<sup>-2</sup>]. This is quite similar to the slope found in the X-ray study for the extinction  $A_V$  by Predehl & Schmitt (1995):  $N(H) = 1.79 \pm 0.003 \times 10^{21} A_V - 0.41 \,[\text{cm}^{-2}]$ if  $A_V = 3.1E(B-V)$ . This is noted here because there is a deviation of the correlation by Predehl & Schmitt (1995) between  $A_V$ , indicator of the dust, and N(H), indicator for cold gas and dust, at low distances. This is probably due to a significantly lower amount of dust in the Local Bubble, as also found by Predehl & Schmitt (1995) for the source LMC X-1. Therefore, we consider only open clusters with distances larger than 230 pc. We compared the hydrogen column densities we inferred from the open cluster reddenings with those obtained by our two 3D models of the ISM distribution. 628 out of the 650 open clusters by Piskunov et al. (2006) lie within the considered data cube with distances larger than 230 pc and smaller than 4.5 kpc. The scatter in the obtained extinction differences increases with distances for both models (see Fig. 2.12). For the model based on Hakkila et al. (1997) the mean deviation is around  $9 \cdot 10^{20}$  cm<sup>-2</sup>, the mean value for the analytical model is  $27 \cdot 10^{20}$  cm<sup>-2</sup>. Considering only distances up to 1 kpc these values are  $3.3 \cdot 10^{20}$  cm<sup>-2</sup> and  $8.1 \cdot 10^{20}$  cm<sup>-2</sup> respectively. Interestingly at some Galactic longitudes ( $l \approx 0^{\circ}$ ,  $120^{\circ}$ , and  $300^{\circ}$ ; see Fig. 2.13) and at the Galactic latitude  $b \approx 0^{\circ}$  the scatter is more pronounced. The extinction routine by Hakkila et al. (1997) predicts the observed properties of the open clusters better than the analytical model. This can be partly explained by the use of (older) open cluster data (e.g. Fitzgerald (1968)) in the routine by Hakkila et al. (1997).

The analytical model tends to overpredict the extinction by an order of magnitude, especially at larger distances. Due to the convincing advantages of extinction data derived

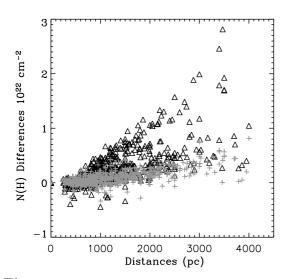


Figure 2.12: N(H) deviations at different distances

Shown are the differences between the model N(H) at the distances and positions of the open clusters and the N(H) obtained directly from the reddening measurements according to Piskunov et al. (2006). The results of the extinction model based on Hakkila et al. (1997) are plotted as grey crosses, those of the analytical model as black triangles. While the scatter at low distances is relatively small for both models, the analytical model has a larger spread at larger distances.

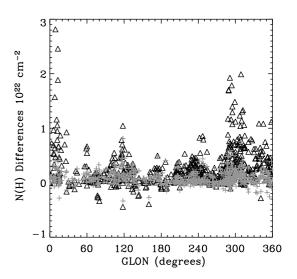


Figure 2.13: N(H) deviations at different Galactic longitudes

Shown are the differences between the model N(H) at the distances and positions of the open clusters and the N(H) obtained directly from the reddening measurements according to Piskunov et al. (2006). The results of the extinction model based on Hakkila et al. (1997) are plotted as grey crosses, those of the analytical model as black triangles. For both models a larger scatter is visible at  $GLON=0^{\circ},120^{\circ}$ , and  $300^{\circ}$ .

from open clusters, we include them finally as local inhomogenities in our models for distances larger than 230 pc. Again, we take into account that the column density can only increase with distance. If the column density at a distance of 240 pc,  $N(H)_{240}$ , is lower than the value from the Lallement cube at 230 pc at the same line of sight, then we consequently change the N(H) values for distances smaller than 240 pc to the lower value  $N(H)_{240}$  until N(H) is always either constant or increasing with distance for this particular line of sight.

In principle, our N(H)-models can be used to determine distances of sources with known hydrogen column densities. Aiming to apply our N(H)-models later to X-ray detected neutron stars the performance of our models for well known sources is interesting. We selected four of the rare neutron stars having at the same time known parallaxes and hydrogen column densities with small error bars obtained from X-ray observations. In Table 2.2 we present the model-derived distances for the measured N(H) range as well as the model-derived N(H) at the given parallelectic distance. While the analytical model gives reasonable results for PSR B0656+14, Vela and RX J1856.5-37541, the extinction model based on Hakkila et al. (1997) underestimates the column density towards Vela significantly. As both models are equal up to 230 pc, both give the same minimal distance of 220 pc towards Geminga which deviates from the claimed distance by Caraveo et al. (1996). Interestingly, Walter et al. (Conference, London, April 2006) reported recently a revised distance of  $254^{+111}_{-59}$  pc towards Geminga. In the case of RX J1856.5-37541 the derived minimal and maximal distances are completely included in the N(H) cube obtained by the Lallement et al. (2003) measurements. Here, an error of 25 pc applies while an error estimate is difficult for the analytical model at distances larger than 230 pc. The Hakkila et al. (1997) model has often a formal mean error of the same order as the obtained N(H) values.

As noted above it is still debated how good NaI D-lines are as tracer for hydrogen. It is especially unclear whether molecular hydrogen is traced at all and how well. In Table 2.2 we include the results obtained for two further test objects situated in or behind molecular cloud cores – the star-forming molecular cloud core of CrA close to RX J1856.5-37541 and MBM12 (Magnani et al., 1985). While towards MBM12 there is an enlarged but still underestimated amount of hydrogen (see also discussion by Lallement et al. (2003)), the small CrA cloud is clearly missed. Both examples indicate that one has to be cautious applying the N(H) cube obtained from the Lallement et al. (2003) measurements in the direction of small molecular clouds. However, there are only few such density enhancements of molecular hydrogen in the close Solar neighbourhood. The extinction model as well as the analytical model are in principle sensitive to molecular hydrogen at distances larger than 230 pc. At large distances > 1 kpc the extinction model may

miss molecular clouds due to their low angular size and bad sampling while the analytical model does not consider individual clouds.

### Table 2.2: Testing the ISM models for individual objects

For each object the known distance and hydrogen column density N(H) with references are given. Furthermore are listed for each model: the obtained minimal distance  $D_{MIN}$  for the lowest N(H) value and the maximal distance  $D_{MAX}$  for the largest N(H) value as well as the expected N(H) for the known distance. The models are the same up to a distance of 230 pc (see text in Sec. 2.3.2 for details). The first four objects are neutron stars with VLBI or HST parallaxes and X-ray-obtained N(H). TY CrA lies within the CrA star forming molecular cloud core close to RX J1856.5-37541. HD 18190 is thought to be situated behind MBM 12.

Golden et al. (2005); 2: Marshall & Schulz (2002); 3: Dodson et al. (2003); 4: Pavlov et al. (2001); 5: Caraveo et al. (1996); 6: Jackson & Halpern (2005); 7: Kaplan et al. (2002b); 8: our EPIC PN fit; 9: Casey et al. (1998); 10: Forbrich et al. (2006); 11: Hobbs et al. (1988);

 $^a log(N(NaI)) = 10.6 < 11$  Ferlet et al. (1985) formula was doubted by Welty et al. (1994), see text;  $^b$  distance towards TY CrA in the star forming region CrA;  $^c$  mean value;  $^d$  lower limit for N(NaI) was converted to N(H); out: needed N(H) is not reached up to the here considered 1 kpc distance

| Name             | Distance          | Ref. | N(H)                        | Ref. | analytical model    |                    |                             | extinction model |                    |                             |  |
|------------------|-------------------|------|-----------------------------|------|---------------------|--------------------|-----------------------------|------------------|--------------------|-----------------------------|--|
|                  |                   |      |                             |      | $\mathcal{D}_{MIN}$ | $\mathbf{D}_{MAX}$ | N(H)                        | $D_{MIN}$        | $\mathbf{D}_{MAX}$ | N(H)                        |  |
|                  | [pc]              |      | $[10^{20} \text{ cm}^{-2}]$ |      | [pc]                | [pc]               | $[10^{20} \text{ cm}^{-2}]$ | [pc]             | [pc]               | $[10^{20} \text{ cm}^{-2}]$ |  |
| PSR B0656+14     | $288^{+33}_{-27}$ | 1    | $1.73 \pm 0.18$             | 2    | 240                 | 260                | 2.68                        | 230              | 240                | 2.86                        |  |
| Vela             | $287^{+59}_{-34}$ | 3    | $3.3 \pm 0.3$               | 4    | 300                 | 330                | 2.73                        | 860              | 910                | 1.07                        |  |
| Geminga          | $157^{+19}_{-17}$ | 5    | $1.76 \pm 0.95$             | 6    | 220                 | 300                | $0.09^{a}$                  | 220              | 240                | $0.09^{a}$                  |  |
| RX J1856.5-37541 | $140 \pm 40$      | 7    | $0.74 \pm 0.10$             | 8    | 130                 | 140                | 0.87                        | 130              | 140                | 0.87                        |  |
| TY CrA           | $129 \pm 11^{b}$  | 9    | $130 \pm 0.3^{c}$           | 10   | out                 | out                | 0.08                        | out              | out                | 0.08                        |  |
| HD 18190         | 185               | 11   | $> 7.21^d$                  | 11   | 440                 | • • •              | 5.05                        | 800              | • • •              | 5.05                        |  |

Table 2.3: Distances obtained for the Magnificent Seven

The N(H) was obtained by blackbody and absorption line (tabs) XSPEC-fits from EPIC-pn observations. The number of lines used is indicated in parenthesis. The corresponding model prediction of the distance is given for the analytical model:  $d_{ana}$ , the extinction model based on Hakkila et al. (1997)  $d_{ext}$ , and the analytical model plus consideration of possible 30% underprediction by the sodium D-lines:  $d_{ana130}$ . See also text for discussion.

| name            | N(H) (#lines)               | $d_{ana}$ | $d_{ext}$ | $d_{ana130}$ |
|-----------------|-----------------------------|-----------|-----------|--------------|
|                 | $[10^{20} \text{ cm}^{-2}]$ | [pc]      | [pc]      | [pc]         |
| RX J1856.5-3754 | 0.7(0)                      | 135       | 135       | 125          |
| RX J0420.0-5022 | 1.6 (1L)                    | 345       |           | 325          |
| RX J0720.4-3125 | 1.2 (1L)                    | 270       | 235       | 265          |
| RX J0806.4-4123 | 1.0 (1L)                    | 250       | 235       | 240          |
| RBS 1223        | 4.3 (1L)                    |           |           |              |
| RX J1605.3+3249 | 2.0 (3L)                    | 390       |           | 325          |
| RBS 1774        | 2.4 (1L)                    | 430       | • • •     | 390          |

## Application of the two 3D models

**Distance estimates** A possible application is to estimate the distances to neutron stars without parallaxes or other distance measurements. This is the case of the majority of the M7 where up to now only a parallactic distance towards RX J1856.5-37541 and a tentiative parallactic distance towards RX J0720.4-3125 are reported in the literature (Walter & Lattimer, 2002, van Kerkwijk & Kaplan, 2006). We obtain N(H) by considering the best XSPEC-fits for blackbody and absorption lines of all currently available XMM-Newton EPIC-pn observations reduced with XMM SAS 6.5 for each neutron star. As noted by Haberl (2006), in this respect the XMM-Newton EPIC-pn is the best-suited instrument for relative measurements with reasonably small errors ( $\approx 0.1 \cdot 10^{20} \text{ cm}^{-2}$  for all objects). The model predictions considering the column densities of the M7 can be found in Table 2.3. As noted before, the technical sampling is 10 pc. If a N(H) value lies between two sampling points we indicate this by noting  $\cdots 5$ , e.g. 125 pc if the N(H) of the object is between the model N(H) values at distances of 120 pc and 130 pc. However, even errors in the best-studied regions ( $\leq 230$  pc) are around 25 pc, and can be much larger otherwise. In case of the extinction model based on Hakkila et al. (1997) one cannot always derive a convincing value due to bad sampling with the (low) extinction not changing over a large scale of distances (e.g. up to 1 kpc). For the analytical model only the high latitude object RBS 1223 is a problem where at 1 kpc one arrives only at  $3.2 \cdot 10^{20} \; \mathrm{cm^{-2}}$ . The limitations of this large-scale model appear here. However, absorption lines in the spectrum also influence N(H). Schwope et al. (2006) fitted the spectrum of RBS 1223 using recent observations and obtained  $N(H) = 3.7 \cdot 10^{20} \text{ cm}^{-2}$  for one absorption line. This value is comparable to our result in Table 2.3, taking into account the additional data. However, the fit was not very good and Schwope et al. (2006) obtained better fits with two absorption lines, yielding N(H) values ranging from  $1.2 \cdot 10^{20}$  cm<sup>-2</sup> to  $1.8 \cdot 10^{20}$  cm<sup>-2</sup>. The lower value would correspond to a distance of 525 pc when using the analytical model.

Overall, the distances derived from both models towards two neutron stars are in acceptable agreement: RX J0720.4-3125 has a distance of 250 pc and the distance of RX J0806.4-4123 is 240 pc. Since both objects are close to the border of the sodium measurements, an error of  $\approx 25$  pc seems reasonable. Very recently, van Kerkwijk & Kaplan (2006) reported a parallax measurement of RX J0720.4-3125 yielding a prelimnary distance of  $330^{+170}_{-80}$  pc, which is in agreement with our value within errors. The distance values obtained for other objects via the analytical model have to be used with caution as local clumpiness of the ISM is not considered by this model at distances > 230 pc. Considering the open cluster test from above, the mean N(H) deviation of the analytical model up to 500 pc is  $0.05 \cdot 10^{20}$  cm<sup>-2</sup>; the standard deviation, however, is  $4.9 \cdot 10^{20}$  cm<sup>-2</sup>.

#### Population synthesis

Both new 3D models of the ISM distribution can be regarded as more realistic than the analytical model used before by e.g. Popov et al. (2005). The derived  $\log N$ - $\log S$  curves are plotted in Fig. 2.7 in comparison to the old ISM model used by Popov et al. (2005). The same mass spectrum as in Popov et al. (2006a), cooling curves (model I of Popov et al. (2006a) for hadron stars), the initial progenitor distribution as outlined in Sec. 2.1, the same abundances and cross-sections (here those of Wilms et al. (2000) for comparison) and identical remaining parameters are used. The curve obtained with the refined analytical absorption model is very similar to the old curve at the bright end. Both are situated a little apart from the measured integrated number of objects. Towards lower count rates, the new curve lies clearly below the old analytical model without the data by Lallement et al. (2003) and Piskunov et al. (2006). One might have expected that differences should be largest at low distances and hence for bright sources. However, averaging over the small Local Bubble gives apparently the same result as the simpler description by e.g Popov et al. (2005). The influence of the better model for the Solar vicinity is apparent in the expected location likelihoods for neutron stars (see below). Going to larger distances the additive column densities are especially large around  $l \approx 300^{\circ}$  to  $l \approx 60^{\circ}$  in the Galactic plane where many objects could be expected. Thus, the number of predicted neutron stars is reduced. Considering the absorption based on the extinction model by Hakkila et al. (1997) gives another picture. At the bright end this curve is much lower than the old without refined 3D ISM model, while the difference becomes smaller towards low count rates. The N(H) model based on the extinction study by Hakkila et al. (1997) shows on average much higher column densities already at 240 pc compared to the new analytical model. Given the nearly rectangular shape of the regions with relatively high values in the l, b plane these seem to be caused at least partly by bad sampling and the necessary statistical treatment. The higher N(H) results in less observable sources bringing the corresponding  $\log N - \log S$  much closer to the actually measured number of sources at the bright end. We note here again that both absorption models are the same up to 230 pc based on the measurements by Lallement et al. (2003). Both also consider the open cluster data, however slightly differently as the column density is only allowed to increase.

We compare in the following the Galactic maps (Fig. 2.16 to Fig. 2.18 on page 38) of simulated number density of the neutron stars: Fig. 2.16 corresponds to the population synthesis with the old analytical ISM model by Popov et al. (2005), Fig. 2.17 is obtained when applying the refined analytical ISM model, and Fig. 2.18 represents the result of using the ISM model based on the extinction study by Hakkila et al. (1997). All remaining parameters are the same (e.g. masses, cooling cuves, abundances). As explained on page 17 one has to restrict on the interpretation of the general behaviour in the Galactic maps. Comparing to the old result (Fig. 2.16), the two new ISM models result both in a reduction of the expected neutron star number at  $l \approx 90^{\circ}$  to 140°,  $b \approx 0^{\circ}$ . This reduction is very likely caused by the Taurus Dark Cloud being present in the data of Lallement et al. (2003), see especially their Fig. 9. These data have been applied in both models. It seems, there is also a slight reduction in the neutron star number expected at higher Galactic latitudes  $|b| > 30^{\circ}$ . However, we need better statistics here. The main difference found by comparing Fig. 2.17 to Fig. 2.18 is the enhanced density of expected neutron stars in the region  $l \approx 340^{\circ}$  to 20° in case of the extinction model based on Hakkila et al. (1997). This is due to the lower absorption predicted by Hakkila et al. (1997) towards the Galactic center, which is apparent in the model N(H) (Fig. 2.11 comparing to Fig. 2.10 referring to the results of the refined analytical model).

We show in Fig. 2.19 the locations of the known 13 neutron stars which have strong thermal X-ray emission. These are the same sources as plotted in the  $\log N$ - $\log S$  curves. The neutron star number predicted by the population synthesis fits well for  $l > 180^{\circ}$ . At  $l \approx 100^{\circ}$  to  $140^{\circ}$  there are up to now no known sources while the population synthesis predicts a high number density here. In the region  $l < 90^{\circ}$  there are suprisingly two sources while the population synthesis predicts a low source density there. One may suspect that the region  $l \approx 100^{\circ}$  to  $140^{\circ}$  ( $|b| < 15^{\circ}$ ) is a good place to look for the next candidates of X-ray thermal neutron stars. One of the two closeby NSs, PSR 1929+10, seems not to come from this region given its proper motion direction Hobbs et al. (2004), while we do not know the proper motion of 3EG J1835+5918.

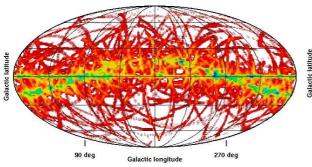


Figure 2.14: The NS distribution for  $r_{GB} = 500$  pc, absorption treatment with wabs (angr) and the analytical ISM model as applied by e.g. Popov et al. (2005).

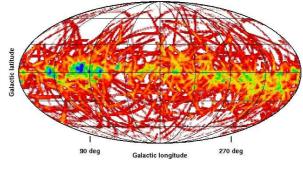


Figure 2.15: The NS distribution for the new progenitor distribution as described in sec. 2.1. All other parameters are the same as for the simulation of Fig. 2.14, especially the ISM distribution.

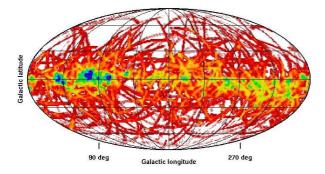


Figure 2.16: The NS distribution for the new progenitor distribution as in Fig. 2.15, but applying tbabs(wilm) instead of wabs(angr) as described in sec. 2.2.1.

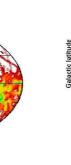


Figure 2.17: The NS distribution in case of applying the analytical 3D-model as described in sec. 2.3. The new progenitor distribution and tbabs(wilm) are used like for Fig. 2.16.

Galactic longitude

90 ded

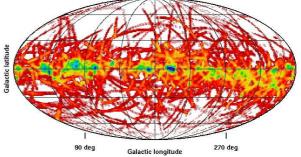


Figure 2.18: The NS distribution in case of applying the 3D-extinction model based on Hakkila et al. (1997), for description see sec. 2.3. The new progenitor distribution and tbabs(wilm) are used like for Fig. 2.16.



The galactic maps show the expected numbers of isolated neutron stars with thermal X-ray emission in units of density per square degree. All galactic maps are in Mollweide projection with galactic coordinates l and b. The galactic center at  $l=0^{\circ}$ ,  $b=0^{\circ}$  is in the center. All maps have the same scale [0,0.015] number density per square degree. Only sources with ROSAT PSPC count rates larger than 0.05 cts s<sup>-1</sup> are considered. As outlined in sec. 2.1 (page 17), one should not compare individual 'traces' but only the general picture with concentrations in particular regions. For discussion see individual sections 2.1, 2.2.1 and 2.3.

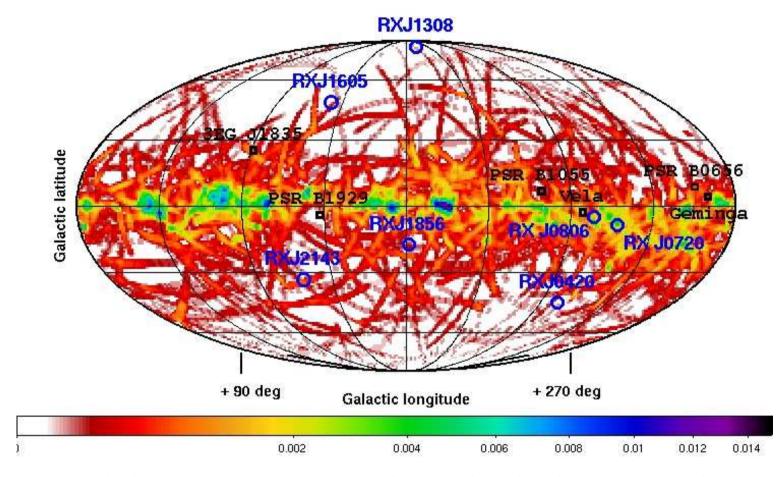


Figure 2.19: The obtained expected neutron star number density together with the known neutron stars showing strong thermal X-ray emission. The new progenitor distribution, tbabs(wilm) and the 3D ISM model based on Hakkila et al. (1997) were used for the population synthesis. For discussion see Chapter 2.

# 2.4 Fainter sources with XMM-Newton

As one of the two current modern major X-ray observatories XMM-Newton surpasses Chandra in collecting area and sensitivity, especially when considering the soft X-ray regime in which objects such as the Magnificent Seven are investigated. The European Photon Imaging Camera (EPIC) with its pn-CCDs has been found to be the best currently available instrument with respect to relative measurements of the M7 (Haberl, 2006). It would be interesting to have an idea how many more sources one could observe using XMM-Newton instead of ROSAT. Unfortunately there is no All Sky Survey done or planned with XMM-Newton. We note here the second XMM Serendipitous Source Catalogue (XMM-SSC2, pre-released 20.7.2006 by the XMM Survey Science Centre Consortium<sup>1</sup>), which covers 285 deg<sup>2</sup> (0.7% of the sky). The included sources have a median flux of  $2.4 \cdot 10^{-14}$  erg cm<sup>-2</sup> s<sup>-1</sup> in the total photon-energy band from 0.2 keV to 12 keV. The XMM-Newton pointings have, however, different depths and the percentage of the sky they cover has not necessarily to scale with the expected/observed NS number. It was shown above that the expected density of the observable neutron stars is highly inhomogeneous on the sky and one would need to consider the Galactic coordinates of the pointings. Therefore, we regard the following more as preparatory work in respect to future planned All Sky Surveys like the one of eROSITA<sup>2</sup>. However, it may also be useful in the individual discussion of larger regions covered by XMM.

XMM-Newton has a nominal sensitive energy range of 0.2 keV to 12 keV. We use this full energy range in the program code. However, all the flux of the sources studied here is below 2 keV. The lower energy border is more important and it is above the one of ROSAT. While in principle it is possible to consider lower energies down to 150 eV for individual pointings (see Sec. 3.3), this is not the standard procedure applied e.g. in the XMM Slew Survey or the XMM-SSC2. The effective areas were calculated from recent (spring 2006) response files available at MPE from calibration work done by F. Haberl. They have around 2000 nodes in energy. The effective areas are for on-axis observations. We therefore consider a mean vignetting of 80% to take into account sources observed off-axis. In contrast to ROSATs proportional counter one deals with CCDs for the XMM-Newton EPIC-pn instrument. X-ray photons of high energies can illuminate multiple pixels. However, at the low energies important for thermally emitting NSs, most EPIC-pn events are recorded by single pixels, and there is little contribution from double-pixel events. Our population synthesis result, the log N-log S curve of expected thermally emitting X-ray NSs at XMM-Newton EPIC-pn count rates, is presented in Fig. 2.20.

<sup>&</sup>lt;sup>1</sup>http://xmmssc-www.star.le.ac.uk/

<sup>&</sup>lt;sup>2</sup>www.mpe.mpg.de/erosita/Flyer.pdf; see also Sec. 3.4

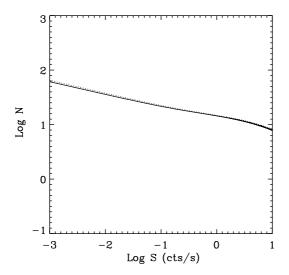


Figure 2.20: The  $\log N$ - $\log S$  curve for XMM EPIC-pn

The expected number N of neutron stars with strong thermal X-ray emission is plotted over the XMM-Newton EPIC-pn count rate S. The population synthesis applied is similar to that decribed before for ROSAT, but with the instrument function of the XMM-Newton EPIC-pn camera in the energy range from 0.2 keV to 12 keV, see also text. The new progenitor distribution and absorption treatment tbabs(wilm) for the analytical ISM model are applied as described for the ROSAT simulations. To illustrate the unimportance of double-pixel events in case of XMM-Newton EPIC-pn, the solid curve is obtained if considering single-pixel events only, and the dotted curve stands for also including double-pixel events. We note that the  $\log N$ - $\log S$  curves are obtained for the (unrealistic) full sky coverage by XMM-Newton observations.

# 2.5 Conclusions

From Sec. 2.1 we conclude that the new progenitor distribution which takes into account the locations of OB associations does not change significantly the number of expected neutron stars integrated over the whole sky, but it is important when it comes to predictions for particular regions in the sky. These predictions are also interesting in the light of new searches for X-ray thermal isolated neutron stars. In particular, new searches are promising in regions where the predicted numbers of isolated neutron stars with thermal X-ray emission are high.

In general, interstellar absorption has a strong effect on the observed soft X-ray spectrum of a thermally emitting neutron star. The most important parameter influencing

interstellar absorption is the amount of material, described by the hydrogen column density, towards the objects. The 3D-distribution of the ISM (Sec. 2.3) influences strongly the number of observable neutron stars with (soft) thermal X-ray emission. It is especially important to consider the local Solar neighbourhood as it was done in our models by the usage of data by Lallement et al. (2003). Considering the expected number of neutron stars in particular regions both ISM models described in Sec. 2.3 deviate only shlighly from each other in their predictions. The  $\log N$ - $\log S$  curve in case of the ISM model based on Hakkila et al. (1997) fits better the bright end of the observational measurement points compared to the refined analytical ISM model. Comparing predicted to measured properties of particular, (relatively close) known sources indicates the weakness of the ISM model based on Hakkila et al. (1997), which is often poorly sampled. Here, the analytical model gives more reasonable results. However, our tests are based on a very small number of objects.

Different abundances and cross-sections (Sec. 2.2) can lead to flux differences of a factor larger than two at high column densities. The differences are much smaller at low column densities. The effect on the population synthesis is small as the neutron stars at low hydrogen column densities (usually the closest NSs) have the largest impact on the  $\log N$ - $\log S$  curve.

Additionally, the distances towards two of the Magnificent Seven have been estimated. Here, the results obtained from the both ISM models are in agreement. The estimated distance for RX J0720.4-3125 is  $250 \pm 25$  pc, and for RX J0806.4-4123 it is  $240 \pm 25$  pc. The recent preliminary parallactic distance of RX J0720.4-3125,  $330^{+170}_{-80}$  pc, by van Kerkwijk & Kaplan (2006) is in agreement with our estimation.

The instrumental response and its implemention in the population synthesis code influence the simulated X-ray spetra which could be observed in case of a thermally emitting neutron star. In Sec. 2.2 our improved code results in higher fluxes with differences to the old code of up to 40% for individual close objects.

In Sec. 2.4 the population synthesis code is adapted to the instrumental response of the XMM-Newton EPIC-pn camera which is based on CCDs in contrast to e.g. the multi-wire proportional counters of ROSAT. The obtained  $\log N$ - $\log S$  curve can be interesting for XMM-Newton surveys covering a relatively large region of the sky with similar sensitivity. Furthermore, the discussion about new aspects in case of the CCD technology (e.g. single-pixel events or single- and double-pixel events) are important as preparatory work in respect to future planned All Sky Surveys like the one of eROSITA.

# Chapter 3

# Searching for new X-ray thermal isolated neutron stars

(partially published, Agüeros et al. 2006, AJ 131, 1740)

It has already been outlined in the Introduction that the Magnificent Seven (M7)<sup>1</sup>, as the seven ROSAT-discovered isolated neutron star with purely thermal X-ray spectra are also named, are exceptional due to the direct view onto their surfaces. However, this sample is too small and too diverse in detail to definitely address the neutron star (NS) equation of state. For example, while RX J1856.5-3754 has a pure blackbody spectrum, the spectrum of RX J1605.3+3249 is best modeled by three absorption lines (Haberl, 2006). A larger sample is clearly needed if one wants to disentangle the possible influences of e.g. geometry, atmospheres and magnetic fields on the individual M7 properties observed. Furthermore, more such objects, some of them at larger distances than the M7, would also allow statistical conclusions about NS populations besides the very local one. In particular, this may shed light on the connections or a possible evolution between the different NS types observed today. As noted in the Introduction most M7 members are probably cooling NSs instead of isolated ISM-accretors. The fraction of bright ISM-accreting NSs expected today is rather small, overpowered by the numbers of coolers (Popov et al., 2000a). The M7 have spectra that peak at soft X-ray energies, making this the best wavelength regime in which to search for similar objects. Furthermore, expanding to fainter X-ray fluxes there are probably some rare NSs which are slow enough to accrete from the ISM (Popov et al., 2000a) and then they also would be observable by their soft X-ray emission. There were many efforts in the past to find new cooling NSs or ISM-accreting

<sup>&</sup>lt;sup>1</sup>for an overview about the known properties of the M7 see Introduction, also Tables C.1, C.2, E.1, E.2, and E.3 in Appendix

NSs, e.g. by Chieregato et al. (2005), Rutledge et al. (2003) and Danner (1998a,b). None of them resulted in any new confirmed candidate up to now. Obstacles were the source confusions due to the large X-ray positional uncertainities as already noted by Rutledge et al. (2003), and the lack of a sufficiently deep optical survey to derive large X-ray-to-optical flux ratios and to identify stringently most of X-ray emitter types. Chieregato et al. (2005) for the first time used ROSAT High Resolution Imager (HRI) pointed observations to overcome the problem of large X-ray error boxes and identified four new candidates, where three turned out to be transients or artefacts while the remaining one still has to be confirmed. This can be rather tricky as the example of Rutledge et al. (2003) shows, whose thirteen candidates turned out not to be isolated NSs by follow-up Chandra observations.

Here, we describe several new attempts to find new M7-like objects from correlations between the ROSAT All Sky Survey (RASS), ROSAT pointed observations and deep XMM-Newton pointings on the one hand and the Sloan Digital Sky Survey (SDSS; York et al. 2000) on the other hand (for further information on ROSAT, XMM-Newton and SDSS see Appendix). All of the M7 have large X-ray-to-optical flux ratios  $f_X/f_{opt}$  and very soft X-ray spectra. Concerning the X-ray-to-optical flux ratios, common classes of X-ray emitters like normal stars, normal galaxies, quasars, BL-Lac objects have typical  $\log (f_X/f_{opt})$  values of -1, 0, +1, +1.5 respectively, while the M7 have values  $\geq 4$  (e.g. Zickgraf et al. 2003, Haberl & Pietsch 1999, Stocke et al. 1991, see also Fig.3 by Schwope et al. 1999). White dwarfs and X-ray binaries, however, can also reach high values. Usually they have  $\log (f_X/f_{opt})$  values of 1 or 2, but can reach also 3 (Rutledge et al., 2003). Mushotzky 2004, and references therein, remarked that a 'typical' soft X-ray-selected AGN has a  $\log (f_X/f_B)$  of around 0, with a full range up to 2. For AGNs selected above 2 keV they reported a significant tail of high  $\log (f_X/f_B)$  values extending up to 4.

According to Maccacaro et al. (1988) one can estimate the  $\log(f_X/f_{opt})$  by combination of the X-ray flux with the V-band magnitudes applying the following formula:

$$\log(f_X/f_V) = \log f_X + \frac{V}{2.5} + 5.37,\tag{3.1}$$

where V is the apparent magnitude of the object in the V-band. In the following we substitute the V magnitude by the SDSS magnitude  $g^1$  to obtain  $\log (f_X/f_{opt})$ . The soft X-ray spectra of the M7 can be identified by the hardness ratios (HR)<sup>2</sup> 1 and

<sup>&</sup>lt;sup>1</sup>While g and V are not equal, the color dependent difference between the two is relatively small, only around 0.05 mag (measured for a typial low-redshift quasar by Fukugita et al. 1996)

<sup>&</sup>lt;sup>2</sup>A hardness ratio HR is a kind of 'X-ray color' defined by the count rate CR in the energy bands band1 (low energy) and band2 (high energy):  $HR = (CR_{band2} - CR_{band1})/(CR_{band2} + CR_{band1})$  ROSAT HR1 applies band1=[0.1,0.4] keV and band2=[0.5,2.0] keV and ROSAT HR2 applies

2 in ROSAT Position Sensitive Proportional Counter (PSPC) observations. The PSPC hardness ratios HR1 and HR2 of the M7 are well below 0 (Table E.2 in Appendix) tracing the very soft objects. We note that soft X-ray-selected AGNs represent around one third of the overall soft X-ray sources (e.g. Hasinger et al. 2005 or Grupe 1996). Thus, source confusion in case of insufficient X-ray-to-optical flux ratios  $f_X/f_{opt}$  is likely. The large flux ratio and the soft X-ray spectrum usually define the conditions for the searches for new M7-like objects. The radio-quiescence of the M7 is an additional search criterion for new candidates. While for the RASS we extend the search to the Faint Sources Catalogue (FSC; Voges et al. 2000); even fainter objects may be found in the deep pointings of ROSAT and XMM-Newton.

The search strategy for RASS with its relatively bright sources and large position errors is different from that used for the deep pointings, especially since the bright sources of the RASS been searched several times already for isolated NSs. One difference is for example the use of hardness ratios, which are not considered for the RASS as initial search condition (see details below).

In the following sections the different search strategies and data used in this thesis are described individually. We start with the RASS, continue with the ROSAT PSPC and HRI pointings and end with the analysed deep XMM-Newton observations. There is a discussion of the results, especially the candidates identified, in each section as well as overall conclusions at the end of this chapter.

In the following we use SDSS primary photometry, which requires that objects have a single entry in the database, that they are not deblended<sup>3</sup> and that they fall within the survey boundaries (see Stoughton et al. 2002). PSF magnitudes are used as they provide the best estimate for isolate stellar magnitudes (see Stoughton et al. 2002).

# 3.1 The ROSAT All Sky Survey

This part of the project is based mainly on the PhD work by M. Agüeros, appeared as Agüeros et al. 2006. Done in close cooperation, we note that our main contribution is the investigation of the X-ray properties of the analysed sources.

The X-ray-to-optical flux ratio limits reached by comparing the RASS and SDSS is usually high enough to exclude soft X-ray-selected AGNs. A serious problem, however is the source confusion resulting from the large positional errors of the RASS sources and the many possible optical objects within it. M. Agüeros at Washington University (Seattle, USA) therefore developed an algorithm to identify initial candidates only by the exclusion of confusing optical sources within the RASS error circles. Only RASS sources with quoted  $1\sigma$  positional errors below 15'' are selected. Optical sources of the correlated SDSS Data Release 4 (DR4) are analysed within four times the ROSAT positional error. Fields with known RASS quasars (e.g. Anderson et al. 2003) with  $\leq 1'$  of the X-ray position have been excluded, along with fields having g < 15 mag objects, which are probable stellar X-ray emitters. In this first step roughly half of the selected 9500 RASS sources remain for further analysis. In the next step, the fields were screened for UV-excess objects. These are objects satisfying u-g < 0.6 mag and  $u \le 22.0$  mag, the SDSS 95% completeness limit in the u-band (Stoughton et al., 2002). As derived in statistical studies by e.g. Richards et al. (2002), these sources are candidate (photometric) quasars, but this cut removes also white dwarfs and cataclysmic variables / X-ray binaries. Quasars with atypical colors or red-shifted quasars cannot be ruled out completely

<sup>&</sup>lt;sup>3</sup>deblending object means usually an extended composobject decomposed into several child ('deblended') objects; see e.g. http://www.sdss.org/dr5/products/catalogs/flags\_detail.html#status

by this cut. Therefore, all fields are excluded which have any SDSS DR4 source in the  $4\sigma$  error circle, whose  $\log (f_X/f_{opt})$  is  $\leq 1.2$ , the typical upper limit for active galactic nuclei (AGNs) given by Stocke et al. 1991. All objects of magnitudes  $g \leq 22.2$  mag, the SDSS 95% completeness limit in the g-band (Stoughton et al., 2002), are taken into account for this stringent elimination step. The remaining 74 RASS sources with SDSS photometry are fed to SIMBAD¹ and the NASA /IPAC Extragalactic Database (NED)². Catalogued galaxy clusters, BL-Lac objects, radio sources or bright 2MASS sources within the X-ray  $4\sigma$  error circle lead to exclusion of 41 fields from further consideration. By visual inspection of the SDSS images another 3 fields are eliminated due to confusion in the SDSS photometry, e.g., because of a saturated and uncatalogued bright star.

The ROSAT soft and hard band images for the remaining 30 fields were visually inspected, and X-ray catalogues were searched for pointed observations in order to assess whether any of these sources are variable. Some of the RASS sources with low detection likelihoods<sup>3</sup> turned out to be rather uncertain X-ray detections. Others are artefacts, e.g. from a nearby bright RASS source. Some of the sources seem to be extended and are also excluded. We note that one of the candidates by Rutledge et al. (2003), 1RXS 115309.7+545636, is eliminated at this stage. As has been confirmed by the follow-up Chandra observation by Rutledge et al. (2003), this source is indeed not a M7-like object. Three RASS sources seem to have an underestimated position error  $1\sigma = 6''$  given their countrates and exposure times. These fields are also excluded from further analysis. We are left with 18 RASS sources after checking their X-ray images. For these objects, the hardness ratios are not taken into account for candidate selection. One the one hand, the HR errors of the mostly faint sources are large. On the other hand, we wanted to extend our search to INSs suffering maybe from larger interstellar absorption than the M7, thus showing harder X-ray spectra than these sources.

Finally, a catalogue of optically selected SDSS clusters (J.Annis 2005, private communication) has been used to get an idea whether it is likely that some of the remaining RASS sources may be associated with faint clusters of galaxies. The richness of a galaxy cluster is described by the  $n_{gal}$  parameter, the number of red-sequence galaxies brighter than  $0.5L_{\star}^{4}$  within 1 Mpc radius volume, where redshifts were obtained by SDSS photometry. RASS sources are not considered further if a cluster candidate with  $n_{gal} \geq 3$  is present within 1', or  $n_{gal} \geq 6$  within 5'. The coordinates of two fields are not covered by the cluster catalogue.

<sup>&</sup>lt;sup>1</sup>http://simbad.u-strasbg.fr/

<sup>&</sup>lt;sup>2</sup>http://nedwww.ipac.caltech.edu/

<sup>&</sup>lt;sup>3</sup>The detection likelihood L is determined by  $L = -\ln(1-p)$ , where P is the probability of source detection. Usually a maximum likelihood algorithm is applied in case of ROSAT source detections.

 $<sup>^4</sup>L_{\star}$  is the luminosity of the Milky Way

The final result consists of 11 candidate RASS fields. Among them is RX J1605.3+3249, the only previously known neutron star of the Magnificent Seven which is located in the sky region covered by SDSS DR4. All objects are listed in Table 3.1, their positions on the sky are shown in Fig. 3.3. The candidate fields of new isolated neutron stars are scheduled in the current *Chandra* observation cycle to obtain confirmation of the X-ray properties and better positions.

| Source name             | p.e.      | Count rate                     | DL   | HR1              | HR2              | Exp. | Min.                       |
|-------------------------|-----------|--------------------------------|------|------------------|------------------|------|----------------------------|
| 1RXS J                  | $1\sigma$ | $[10^{-2} \text{ cnt s}^{-1}]$ |      |                  |                  | [s]  | $\log\left(f_X/f_g\right)$ |
| $003413.7 - 010134^{a}$ | 14''      | $1.3 \pm 0.6$                  | 10   | $-0.05 \pm 0.40$ | $0.35 \pm 0.51$  | 630  | 1.8                        |
| $013630.4 + 004226^{a}$ | 13''      | $2.5 \pm 1.0$                  | 16   | $1.00 \pm 0.45$  | $0.75 \pm 0.27$  | 283  | 1.5                        |
| 092310.1 + 275448       | 14''      | $2.5 \pm 1.0$                  | 14   | $0.16 \pm 0.40$  | $1.00 \pm 0.50$  | 407  | 1.5                        |
| 103415.1 + 435402       | 14''      | $1.7 \pm 0.8$                  | 9    | $0.84 \pm 0.37$  | $0.05 \pm 0.40$  | 502  | 1.3                        |
| 110219.6 + 022836       | 15''      | $1.8 \pm 0.8$                  | 11   | $0.43 \pm 0.51$  | $0.07 \pm 0.50$  | 423  | 1.3                        |
| 122344.6 + 373015       | 15''      | $2.8 \pm 1.1$                  | 11   | $-0.35 \pm 0.29$ | $0.60 \pm 0.58$  | 490  | 1.6                        |
| $130547.2 + 641252^{b}$ | 9''       | $16.7 \pm 2.1$                 | 122  | $-0.82 \pm 0.06$ | $-0.62 \pm 0.28$ | 544  | 2.4                        |
| 131400.1 + 072312       | 15''      | $1.8 \pm 1.0$                  | 8    | $-0.32 \pm 0.41$ | $1.00 \pm 0.68$  | 333  | 1.3                        |
| 141428.5 + 601707       | 14''      | $1.4 \pm 0.7$                  | 9    | $0.03 \pm 0.46$  | $1.00 \pm 0.75$  | 630  | 1.3                        |
| 151855.1 + 355543       | 9''       | $3.3 \pm 0.9$                  | 32   | $-0.21 \pm 0.26$ | $0.14 \pm 0.43$  | 518  | 1.3                        |
| $160518.8 + 324907^{c}$ | 7''       | $87.5 \pm 4.1$                 | 1140 | $-0.70 \pm 0.03$ | $-0.58 \pm 0.10$ | 566  | 3.4                        |

<sup>&</sup>lt;sup>a</sup> Outside of optical cluster catalogue footprint; <sup>b</sup> Rejected as an INS by Rutledge et al. (2003);

## Table 3.1: The 11 RASS candidate INS fields

Listed for each RASS candidate are the catalogue name according to Voges et al. (1999) and Voges et al. (2000), the quoted  $1\sigma$  positional error p.e. (including systematic error), the count rate, detection likelihood DL, ROSAT hardness ratios HR1 and HR2, as well as the  $\log(f_X/f_g)$  for the brightest SDSS object within  $4\sigma$  positional error, corresponding to the minimum reached  $\log(f_X/f_g)$  for the optical counterpart of the X-ray source.

<sup>&</sup>lt;sup>c</sup> Known INS among the M7

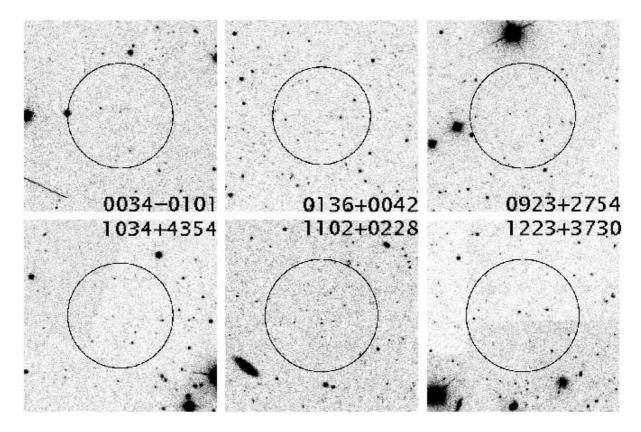
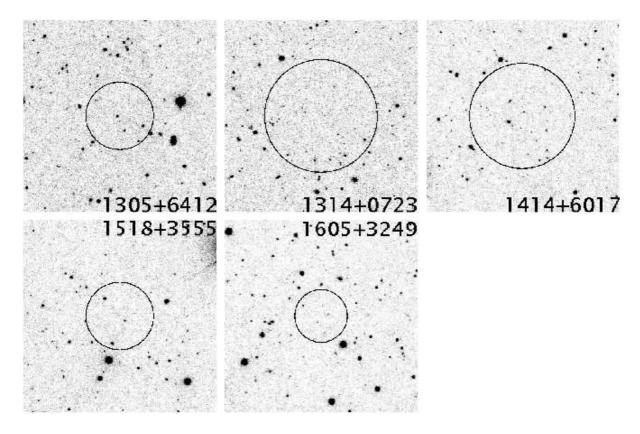


Figure 3.1: SDSS composite g, r, i images of the RASS INS candidates SDSS composite g, r, i images of the RASS fields, with the stretch being the same for all. The  $4\sigma$  RASS positional error circle is shown in each image. The brightest SDSS object seen within any of the error circles is g = 21.66 mag. North is up and East is to the left and the images are roughly 3.5' on a side. Taken from Agüeros et al. (2006).



**Figure 3.2:** (Continued) J130547.2+641252 was rejected as an INS by Rutledge et al. (2003). J160518.8+324907 is a known INS. The brightest SDSS object within any of the  $4\sigma$  positional error circles is g=21.04 mag. Taken from Agüeros et al. (2006).

It is interesting to compare our selection procedure and results with other searches for isolated neutron stars using the RASS. An important recent effort was that of Rutledge et al. (2003) who correlated the RASS Bright Source Catalogue (BSC) with NRAO VLA Sky Survey (NVSS), the IRAS Point Source Catalogue, and the United States Naval Observatory (USNO) A2.0 catalogue. Of their initial 32 candidates, 11 fall within the DR4 footprint. Three of these 11 remained after Rutledge et al. (2003) visually inspected the POSS images and considered available ROSAT HRI pointings. One of them is the previously known RX J1605.3+3249. The algorithm described above excluded automatically many of the 11 sources by Rutledge et al. (2003) at a very early stage. Thanks to the depth of the SDSS and the applied cuts, fields were removed which have e.g. SDSS quasars (confirmed or candidate ones) within the  $4\sigma$  X-ray positional errors. Other candidates have rather bright objects or possible radio counterparts in their error circles. We identified one of the three fields on the final list by Rutledge et al. (2003), 1RXS 115309.7+545636, as probably extended source from the ROSAT X-ray images. We excluded the second source, 1RXS J145234.9+323536, because of a possible association to a galaxy cluster. Both objects were observed with Chandra by Rutledge et al. (2003) and they did not detect an X-ray source in either case. After being processed by our algorithm, there is only one survivor of the 11 Rutledge et al. (2003) initial candidates in the SDSS DR4 footprint – the previously known RX J1605.3+3249.

We conclude that the exclusion of confusing sources based on the algorithm described above works well at this stage. We cannot exclude transient sources, however, from our final object list as only the RASS observations were available for those. Checking for variability is one of the main purposes of the on-going Chandra observations. We note furthermore, that our list of INS candidates in the SDSS DR4 footprint is not complete, as unrelated neighbouring SDSS objects may have led to rejection of fields with an actual isolated neutron star in them. At a magnitude limit of roughly 21 mag (POSS, g) there are already on average three optical sources within each ROSAT Bright Source Catalogue error circle (Rutledge et al., 2003). Due to the large positional errors of the RASS and the high sensitivity of the SDSS, which can reach 24 mag in deep exposures, there is a good chance of excluding isolated neutron star fields with unrelated SDSS DR4 objects in them. This has to be considered if the candidate number is compared to the expected number of isolated neutron stars, derived, for example, from the population synthesis by Popov et al. 2000b, 2003, 2005 or in Chapter 2. Of our initially selected 9500 RASS sources 80% have count rates  $\leq 0.017$  counts s<sup>-1</sup>. We adapt this count rate as rough lower limit to our search sensitivity. The predicted NS number by our improved population synthesis model (see Chapter 2, especially Fig. 2.7) for this minimal count rate is 21 (analytical ISM model) to 26 (ISM model based on extinctions by Hakkila et al. 1997) over the whole sky. Thus,

the naive approximation to the DR4 footprint (6670 square degrees sky coverage) yields 3 to 4 expected isolated NSs. The RASS candidate number presented here is roughly three times larger. Additionally, we note again the probable incompleteness of our candidate list due to the relatively large RASS positional errors. One has to consider that the candidates are all at high galactic latitudes (see Fig. 3.3), where firstly one would expect less observable neutron stars than for the same area in the galactic plane and secondly source confusion by extragalactic sources is high. As mentioned above soft X-ray-selected AGNs represent around one third of the overall soft X-ray sources (e.g. Hasinger et al. 2005 or Grupe 1996) which is relevant for our two soft RASS candidates (HR2 < 0; but note the large errors for the other RASS candidates). Furtheremore, we cannot exclude those AGNs, which are mainly present in hard X-rays above 2 keV and which may reach  $\log (f_X/f_g) \approx 4$  according to Mushotzky (2004). Therefore, we also expect confusion for the other objects. However, only follow-up observations, such as the scheduled Chandra observations, can further clarify the nature of the candidates.

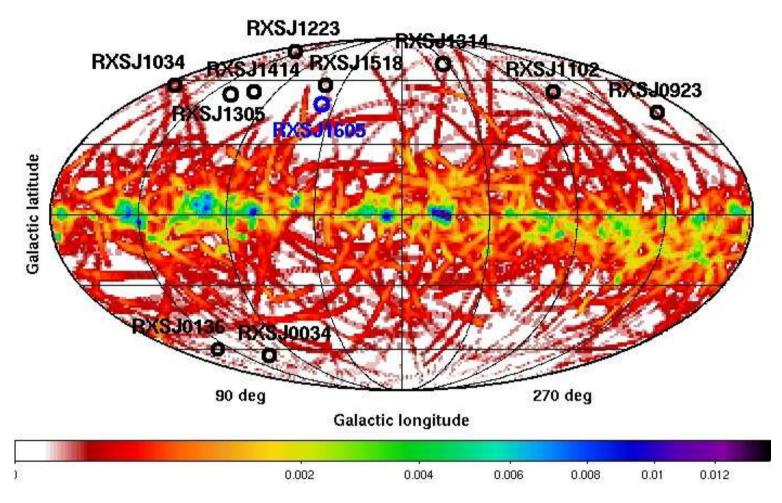


Figure 3.3: RASS candidate positions on the sky

Shown are the galactic locations of the RASS candidates which passed all the selection process well (black). Among them is RX J1605.3+3249, which is marked in blue. The background image correponds to the predicted neutron star number per square degree as derived in Chapter 2. The image is a Mollweide projection in galactic coordinates (positive galactic latitudes are up). It is the same result as Fig. 2.18, obtained for an inhomogenous progenitor distribution and the 3D-ISM model based on the extinction study by Hakkila et al. (1997) to consider the interstellar absorption (for detailed description and discussion see Chapter 2). All candidates are situated at high galactic latitudes where source confusion with extragalactic sources (e.g. AGNs) is more likely than in the galactic plane. See also Sec. 3.1.

# 3.2 The ROSAT pointed observations

The ROSAT PSPC and HRI pointed observations are in general deeper than the RASS. The positional errors of the detected sources are usually smaller than those of RASS objects. One disadvantage is the poor sky coverage -  $\approx 17\%$  for PSPC pointings and only  $\approx 2\%$  for the HRI pointings (ROSAT Scientific Team, 2000a,b). The probability that these are covered by SDSS is small (see Fig. 3.4). Another problem is related to the faintness of the sources. The faintest reliable sources of the PSPC pointings have a count rate of  $7.5 \cdot 10^{-4}$  cnts s<sup>-1</sup>, those of the HRI pointings have a count rate of  $4 \cdot 10^{-4}$ cnts s<sup>-1</sup>. Applying formula 3.1, count rate to flux conversions of  $10^{-11}$  [erg cm<sup>-2</sup> cnt<sup>-1</sup>] for PSPC pointings, and  $3 \cdot 10^{-11}$  [erg cm<sup>-2</sup> cnt<sup>-1</sup>] for the HRI<sup>1</sup> pointings (Voges et al., 1999, Sasaki et al., 2000), as well as g = 22.2 mag, the SDSS 95% completeness limit in the g-band (Stoughton et al., 2002), we derive a maximal limiting  $\log (f_X/f_g) \approx 0.1$  and  $\log (f_X/f_g) \approx 0.3$  for the faintest X-ray sources in case of the PSPC and HRI pointings respectively. These numbers show that even for optically blank fields we can exclude only stars as possible counterparts for such faint X-ray sources, but no AGN for example. That is the reason why our search strategy for the ROSAT pointings is slightly different than the one applied for the RASS. This strategy is based on the X-ray properties of the sources, namely we select only soft sources for further analysis. As outlined above, this is a good criterion to find M7-like objects. However, we may miss highly absorbed sources. While for ROSAT PSPC sources count rates and hardness ratios are available from catalogues (2RXP sources, ROSAT Scientific Team 2000b, Voges et al. 1999), there are no hardness ratios reported in the ROSAT HRI catalogue (1RXH sources, ROSAT Scientific Team 2000a). Considering the optical SDSS photometry we do a less stringent selection than applied for the RASS, namely the exclusion of AGN-typical  $\log (f_X/f_g)$  is not done as initial cut, but must be discussed individually.

<sup>&</sup>lt;sup>1</sup>While a factor 5 would be used for soft X-ray sources the factor 3 is used for hard sources. These factors have been found by comparison of HRI with PSPC data since there is nearly no energy resolution in case of the HRI (Sasaki et al., 2000). A factor 3 is used to avoid overestimation of the flux.

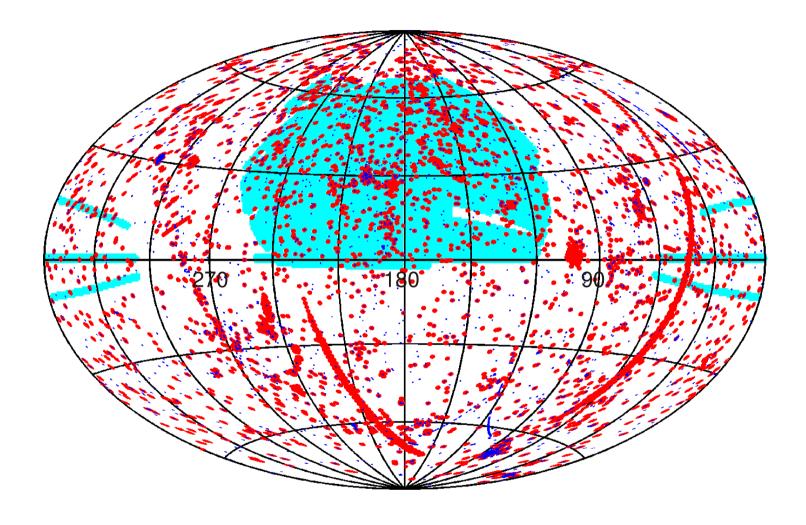


Figure 3.4: The Sky coverage of the SDSS DR5 and the positions of the ROSAT pointings This Aitoff plot is in **RA-DEC coordinates** with positive DEC up. The cyan area marks the covered sky by the SDSS DR5. The ROSAT PSPC pointings (having a field of view with a radius of  $\approx 1^{\circ}$ ) are plotted in red, the ROSAT HRI pointings (smaller field of view with  $r \approx 20'$ ) in blue.

## 3.2.1 ROSAT PSPC Pointings

The ROSAT PSPC was the instrument which was applied to conduct the RASS. The energetic resolution of the PSPC pointed observations is therefore as good as for the RASS, though the obtained source measurements as counts or hardness ratios are much more accurate (for comparably bright sources) due to longer exposures and better photon statistics. The available hardness ratios HR1 and HR2 are defined in the same way as in case of the RASS sources (ROSAT Scientific Team, 2000b, Voges et al., 1999). As can be seen in table E.2, HR1 and HR2 are negative for all of the M7 neutron stars, and HR2 in particular is much smaller than zero. The initial 2RXP candidates are selected in the following way: (i) To expand at least to slightly more absorbed sources we consider the full HR1 range and select the sources satisfying  $HR2 - \triangle HR2 < -0.5$  where the error of HR2,  $\triangle HR2$ , should be lower than 0.25; (ii) The X-ray source extent found has to be < 15" and the likelihood that the source is extended must be below 10; (iii) The positional errors of the 2RXP sources are larger than 0" (to exclude unlikely detections) and below 15". This is the  $1\sigma$  error without the systematic error of the PSPC instrument  $(1\sigma_{sus}=6'')^1$ ; (iv) We consider only exposures longer than 10 ksec as we are especially interested in new faint sources; (v) We take into account only off-axis angles larger than 2', because the actual targets of the pointings are certainly well analysed.

We note that by applying our criteria we cannot recover the only known NS among the M7, which is situated in the sky covered by the SDSS DR5 footprint and observed by the ROSAT PSPC pointings. RX J1605.3+3249 is excluded as we consider only sources with off-axis angles > 2'.

 $246~2\mathrm{RXP}$  sources lie within the SDSS data release 5 (DR5, Adelman-McCarthy et al. in preparation) footprint. Excluding the 32 fields with bright stars or galaxies, we obtain the g PSF magnitudes of all the SDSS DR5 objects within the PSPC  $3\sigma$  positional errors, considering also the  $3\sigma$  systematic error of 18'' as conservative limit. All fields including any SDSS DR5 object classified as 'galaxy' (Stoughton et al., 2002) are neglected in the further analysis. The star/galaxy classification algorithm works on the 95% confidence level up to r=21 mag and even fainter (Stoughton et al., 2002). In case of much fainter SDSS sources one has to visually check whether the pre-selected sources are indeed not extended. This is done at the end of our selection process. Querying the SIMBAD and NED databases within 1' around the X-ray position results in the exclusion of three further fields of 24 (e.g. close QSOs). For the remaining  $21~2\mathrm{RXP}$  sources we estimate the u-g colors for the SDSS objects classified as 'stars'. We exclude fields with any UV-excess object satisfying u-g<0.6 mag and  $u\leq2.0$  mag, the SDSS 95% completeness limit in

<sup>&</sup>lt;sup>1</sup>e.g. http://agile.gsfc.nasa.gov/docs/rosat/ruh/handbook/node34.html and references therein, e.g. Kürster & Hasinger (1993)

the u-band (Stoughton et al., 2002). According to Richards et al. (2002) this cut removes candidate quasars, white dwarfs and cataclysmic variables. The remaining fields without any object of u-g < 0.6 mag are classified as 'class A'. Richards et al. (2002) tested their cuts only down to the SDSS 95% completeness limit of u = 22.0 mag. Furthermore, the color magnitude error can be as high as 1.5 mag for a 24 mag SDSS object. For this reason we classify fields with an object having u-q < 0.6 mag, but u > 22.0 mag as 'class B' and consider them in further analysis. There are two 2RXP sources of class B and one 2RXP source of class A left. Since stars are possible counterparts up to  $\log f_X/f_{opt} = 0$ , the two class B X-ray sources cannot be taken into account as good candidates for INSs, given the negative  $\log (f_X/f_{opt})$  (= -1 and -0.43) of the SDSS objects within their X-ray positional errors. These fields are excluded from further analysis. The remaining field is visually inspected, especially the ROSAT X-ray images (hard and soft band). The source is further classified as '1', because there is a sure X-ray detection and there are no confusing sources. (For completeness we note the other possible classification we would have chosen: '2', if there would be doubts about the X-ray detection or there would be confusing other sources; and '3' (excluded) if the source would turn out to be a bad candidate for an isolated neutron star). The properties of the final 2RXP source are listed in Table 3.2, a short description is given below together with the X-ray images (Fig. 3.5) and the optical SDSS g image (Fig. 3.6).

| Name 2RXP        | RA       | DEC     | p.e. | DL | CR                                | exp          | HR1              | HR2              | oax | class | $\log \left( f_X/f_g \right)^*$ | $\log (f_X/f_g)^{MAX}$ | XMM |
|------------------|----------|---------|------|----|-----------------------------------|--------------|------------------|------------------|-----|-------|---------------------------------|------------------------|-----|
|                  | deg      | $\deg$  | //   |    | $10^{-3} {\rm cnts} {\rm s}^{-1}$ | $\mathbf{s}$ |                  |                  | /   |       |                                 |                        |     |
| J102736.4+533725 | 156.9017 | 53.6236 | 20.1 | 76 | $6.1 \pm 0.8$                     | 14964        | $-0.61 \pm 0.08$ | $-0.48 \pm 0.20$ | 9   | A1    | 0.5                             | 2.8                    | no  |

## Table 3.2: The candidate field found with the ROSAT PSPC pointings

Listed are the position (RA, DEC) and the  $3\sigma$  positional error (p.e.) including  $3\sigma$  systematic error, the source detection likelihood DL, the count rate CR, the exposure of the pointing, the PSPC hardness ratios HR1, HR2 and the off-axis angle oax of the source. Furthermore we classify the source according to its optical and X-ray properties (see text) and give the logarithmic X-ray-to-optical flux ratios:  $\log (f_X/f_g)^*$  is the minimum value obtained for the brightest SDSS DR5 star within the X-ray positional error; and  $\log (f_X/f_g)^{MAX}$  the  $maximal\ reached\ ratio$ , which was derived from the faintest SDSS DR5 object within 1' around the X-ray source. We note that the error of  $\log (f_X/f_g)$ -values can reach 0.4 considering the magnitude errors of the faint SDSS DR5 sources. The last column reports about a known detection in archival XMM-Newton data, e.g. the second XMM-SSC catalogue.

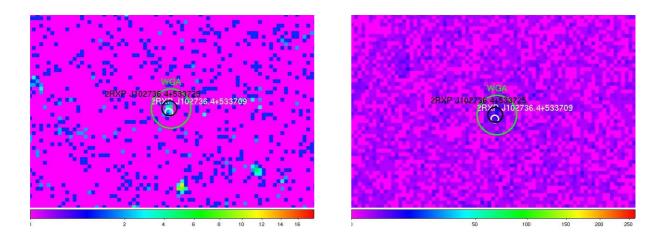


Figure 3.5: ROSAT images of the PSPC candidate 2RXP J102736.4+533725 On the left side the hard band, [0.5, 2.0] keV, of the ROSAT PSPC pointed observation is shown, on the right side the soft band, [0.1, 0.4] keV.

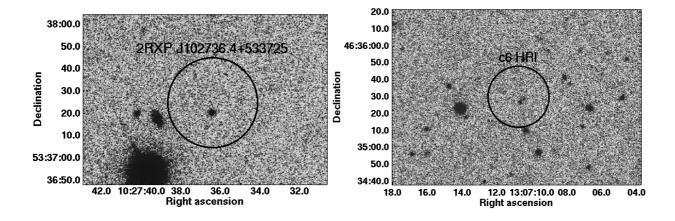


Figure 3.6: ROSAT candidate fields in the SDSS (1) Shown are the SDSS g-band fields of the PSPC candidate 2RXP J102736.4+533725 on the left side and the HRI candidate  $c6_{HRI}$  on the right side. The  $3\sigma$  X-ray positional uncertainties are indicated by the circles. The star in the field of 2RXP J102736.4+533725 has a g-band magnitude of 21.0 mag. The faintest of the three stars within the field of  $c6_{HRI}$  has a g-band magnitude of 24.3 mag.

**Discussion** We discuss in the following the properties of the found candidate in more detail.

**2RXP J102736.4+533725** is clearly detected in the hard and soft band of the PSPC. The other 2RXP source nearby has its origin in a very short exposure so that count rates etc. are not comparable due to huge errors. There are no confusing X-ray sources. The only SDSS DR5 star within the X-ray positional error has u-g=0.6 mag, just above the color cut by Richards et al. (2002). The star has  $\log{(f_X/f_g)}=0.5$ . According to our classification scheme 2RXP J102736.4+533725 is a class A1 source. Whether the X-ray spectrum of this source corresponds to an absorbed blackbody is unclear at this stage, as more counts would be needed for a source spectrum. Variability can be checked only with more X-ray observations since the faint source is not among the RASS, HRI pointings or archival XMM-Newton observations. In further investigations one should check for possible X-ray variability and determine with higher precision the X-ray spectrum of the candidate, as well as the optical spectrum of the SDSS DR5 object.

At the given source location in the sky (Fig. 3.18) one would expect a high probability to detect actually an extragalactic source. On the one hand, the predicted number of observable neutron stars with thermal emission is low and on the other hand, there are many confusing extragalactic sources due to less absorption comparing e.g. to the galactic disk. However, this can be checked only by deep archival or follow-up observations for the found faint PSPC pointing sources.

### 3.2.2 ROSAT HRI Pointings

The High Resolution Imager (HRI) of ROSAT was built to achieve good spatial resolution and the positional uncertainties are very small: the statistical source positional error is often below 1" (1 $\sigma$ ). The systematic error of around 6" (1 $\sigma$ )<sup>1</sup> can sometimes be reduced by boresight correction if there are enough known X-ray sources which also are optically identified in the observed field. The cost of this good spatial resolution is a poor energy resolution. Therefore, no hardness ratios are reported by ROSAT Scientific Team (2000a) for the HRI. However, one can nominally define a hardness ratio based on the 16 energy channels provided by the HRI. This was done by R. Supper and W. Voges at the MPE (Garching) when analyzing the HRI pointings. They used the first four channels as energy band 1 ([0.1, 0.4] keV), the channels 4 to 15 as band 2 ([0.5, 2.0] keV). By these two bands one can derive a hardness ratio  $HR_{HRI}$  defined in the same way as in case of the PSPC observations. R. Supper and W. Voges applied the maximum likelihood detection method (similar to the method used for the PSPC pointings) in contrast to the detections in the 1RXH-catalogue by the ROSAT Scientific Team (2000a), who used the sliding window detection algorithm.

Five of the Magnificent Seven were observed by the ROSAT HRI, and for most of them several HRI pointings are available. The obtained  $HR_{HRI}$  for the different exposures are listed in Table E.1 in the Appendix. Considering only the longest exposures, three of the M7 have negative  $HR_{HRI}$ . For RBS1223 (longest exposure) and RX J1605.3+3249 (only one exposure), however the values are positive. While the spectra of these two neutron stars are indeed slightly harder than those of the remaining three (RX J0420.0-5022, RX J0720.4-3125, RX J1856.5-3754), this is most probably not the reason for the positive  $HR_{HRI}$  of these two actually very soft X-ray sources. Instead, a more convincing explanation is the very low energy sensitivity of the HRI, which additionally suffered often from a large background produced by Solar UV-photons. This large background is also responsable for the relatively small errors of the listed hardness ratios as this error is proportional to the inverse number of detected photons (W. Voges, personal communication). Because of this highly uncertain  $HR_{HRI}$  we consider below a relatively large  $HR_{HRI}$  range for very long exposures only to select nearly all sources which could be soft X-ray sources. In the following, we make use of the unpublished catalogue by R. Supper and W. Voges (personal communication).

The following selection criteria have been applied: (i)  $HR_{HRI} \leq 0.2$  and  $\triangle HR_{HRI} \leq 0.2$  to select preferably soft sources and to take into account the sometimes relatively large flux errors for the faint sources; (ii) an X-ray source extent < 15'', the likelihood that the

 $<sup>^{1}{\</sup>rm e.g.}$  http://agile.gsfc.nasa.gov/docs/rosat/ruh/handbook/node34.html and references therein, e.g. Kürster & Hasinger (1993)

source is extended has to be below 10; (iii) positional errors < 18". The errors listed in the catalogue by R. Supper and W. Voges are the  $1\sigma$  positional errors including the  $1\sigma$  systematic error of the HRI instrument (assuming  $1\sigma_{sys}=6$ " as conservative limit); (iv) We consider only exposures longer than 10 ksec because we are especially interested in new faint sources; (v) We take into account only off-axis angles between 2' and 18', the first because the actual targets of the pointings are certainly well analysed already, the latter because two "hotspots" (defective pixels) are appearing often in HRI pointings at larger off-axis angles.

Around 210 HRI sources fullfilling these conditions lie within the SDSS DR5 footprint. Roughly half of them have no known counterpart sources listing, and are in SDSS fields without apparent sources confusion due to bright stars or galaxies. We obtained all SDSS DR5 objects within  $3\sigma$  positional errors (including the systematic HRI positional error). All 23 fields devoid of any SDSS objects classified as 'galaxy' are analysed further. In the rare case of no SDSS DR5 sources within the HRI positional error we take the faintest objects within 1' to get an idea of the depth reached in the SDSS, which is usally better than the quoted completeness limit of g = 22.2 mag. Thus, higher flux ratios can be derived. In case of the SDSS DR5 sources classified as 'stars' the u-q color was estimated. We exclude fields with any UV-excess object, and classify the fields as done in case of the PSPC pointings (Sec. 3.2.1). Visual inspection of the X-ray images allow us to exclude further fields. We check in particular the correpondance between the source position listed in the catalogue by R. Supper and W. Voges and the position of the published HRI catalogue (ROSAT Scientific Team, 2000a). After X-ray screening and a search for possible radio/optical counterparts, sources are eliminated if a possible counterpart is identified, classified as 'class 2' if there are doubts about the source (e.g. concerning the position) but no obvious counterparts, or as 'class 1' if there are no obvious counterparts and the source is fine.

One ROSAT-object detection is excluded as unlikely detection (although it has a source likelihood of 14) by visual inspection. Checking the NED database within 1' around the X-ray positions we exclude one field with a known radio source at an angular separation of 0.4'. This radio source, GB6 B0955+6848, has a 95% confidence radius of about 50" and cannot be excluded as possible counterpart. Around another X-ray source there is also a radio source at an angular separation of 0.7'. The NVSS point source, however, has a better positional error (max. 7", Condon et al. (1998)) and is probably not a counterpart. A third field can be excluded by visual inspection of the X-ray image and the use of NED, because a known galaxy cluster is very close to the X-ray detection. For some other sources, source confusion can be possible. We note that in one case the target of the HRI observation was a galaxy cluster which is only 4' away. Another possible confusing target

was NGC 4631, a bright galaxy which is also around 4' away. These two fields remain in the sample and are discussed individually below. The list before considering archival X-ray data consists of six candidates, the three best are 'class B1' sources; all six are listed in Table 3.3. The individual sources are discussed below considering also available archival XMM-Newton data. The accompanying figures of X-ray images are Fig. 3.7 and 3.8, the optical SDSS g images are Fig. 3.6 and 3.9. Two candidates can be excluded by the archival XMM-Newton observations (see discussion below). We end with two good candidates and two of lower priority.

Table 3.3: Candidate fields found with the ROSAT HRI pointings

Listed are for each candidate the position (RA, DEC) and the  $3\sigma$  positional error (p.e.), the source detection likelihood DL, the count rate CR, the exposure of the pointing, the determined hardness ratio (see text)  $HR_{HRI}$  and the off-axis angle oax of the source. We classify the sources according to their optical and X-ray properties (see text) and give the logarithmic X-ray-to-optical flux ratios as noted in Table 3.2. The last column reports about a known detection in archival XMM-Newton data, e.g. the second XMM-SSC catalogue. If the source is known (Y) in the XMM-SSC2 or detected in the archival data with our method, it is indicated whether the XMM-Newton data support the interpretation as INS candidate (1), are not constraining (2) or lead to exclusion of the candidate (3).

| Name       | RA      | DEC     | p.e.            | DL | CR                            | exp          | $\mathrm{HR}_{HRI}$ | oax  | class | $\log \left( f_X/f_g \right)^*$ | $\log (f_X/f_g)^{MAX}$ | XMM |
|------------|---------|---------|-----------------|----|-------------------------------|--------------|---------------------|------|-------|---------------------------------|------------------------|-----|
|            | $\deg$  | $\deg$  | //              |    | $10^{-4} {\rm cnts \ s^{-1}}$ | $\mathbf{S}$ |                     | ′    |       |                                 |                        |     |
| $c1_{HRI}$ | 140.003 | 45.7108 | 20.6            | 19 | $17 \pm 4$                    | 26563        | $0.20 \pm 0.05$     | 12.6 | B1    | 1.0                             | 2.2                    | N   |
| $c2_{HRI}$ | 152.997 | 53.1799 | $18^{\rm a}$    | 64 | $18 \pm 3$                    | 22522        | $-0.08 \pm 0.14$    | 6.3  | B1    | 0.9                             | 1.8                    | Y2  |
| $c3_{HRI}$ | 170.882 | 1.7109  | $18^{\rm a}$    | 38 | $14 \pm 3$                    | 17320        | $0.14 \pm 0.15$     | 4    | B1    | 1.0                             | 2.6                    | Y3  |
| $c4_{HRI}$ | 140.185 | 45.7746 | 20.6            | 10 | $7 \pm 2$                     | 27398        | $0.20 \pm 0.07$     | 8.7  | A2    | • • •                           | 1.5                    | N   |
| $c5_{HRI}$ | 190.492 | 32.4799 | $18^{a}$        | 22 | $12 \pm 4$                    | 11812        | $0.20 \pm 0.20$     | 4.1  | A2    | 1.1                             | 1.7                    | Y3  |
| $c6_{HRI}$ | 196.795 | 46.5917 | 18 <sup>a</sup> | 16 | $8 \pm 2$                     | 17972        | $0.00 \pm 0.17$     | 4    | B2    | 0.6                             | 1.5                    | N   |

<sup>&</sup>lt;sup>a</sup> the positional error listed in the HRI pointing catalogue by R. Supper and W. Voges corresponds to the systematic error only because the statistical positional error was very small compared to the systematic one. We adapt  $3\sigma_{sys} = 18''$  as conservative positional error limit.

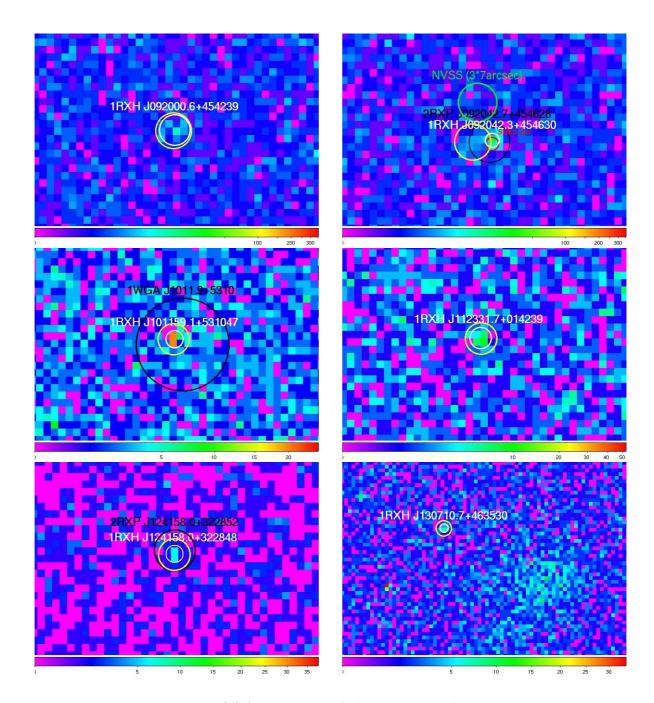


Figure 3.7: ROSAT images of the HRI candidates

Shown are from upper left to lower right the available ROSAT HRI images:  $c1_{HRI}$ ,  $c4_{HRI}$ ,  $c3_{HRI}$ ,  $c5_{HRI}$ , and  $c6_{HRI}$ . The source position of the HRI candidates from the catalogue by W.Voges and R. Supper are marked in yellow, 1RXH-sources in white, 2RXP and WGA sources in black, the NVSS source in green and the SDSS DR5 star in case of  $c4_{HRI}$  is marked red. Despite for the SDSS star all circle radii correpond to the  $3\sigma$  positional errors.

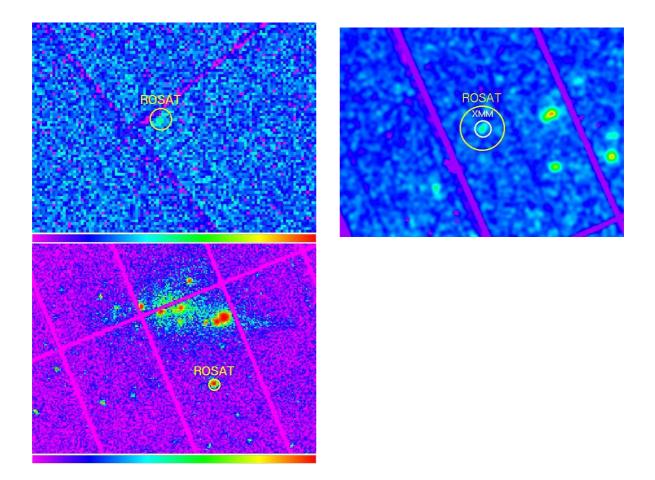


Figure 3.8: XMM-Newton images of the HRI candidates

Shown are the XMM-Newton EPIC-pn images (Full Frame mode) in the X-ray energy interval ranging from 150 eV to 1 keV (see sec. 3.3 for method) for the following HRI pointing objects: **upper left side:**  $c2_{HRI}$  (coincident with 1RXH J101159.1+531047) EPIC-MOS1 (Full Frame mode , thin filter, [0.2 keV to 12 keV], XMM-Newton Science Archive (XSA) image); **upper right side:**  $c3_{HRI}$  (coincident with 1RXH J112331.7+014239) EPIC-pn (Full Frame mode , thin filter, analysis from 150 eV to 1 keV as outlined in sec. 3.3); **lower left side:**  $c5_{HRI}$  (coincident with 1RXH J124158.0+322848) EPIC-pn (extended Full Frame mode , thin filter, [0.2 keV to 12 keV], XSA image). For better visibility, the radius of the source circles do not correspond to the positional errors. 1RXH J101159.1+531047 is detected in the MOS1-image, but it is situated close to the CCD gap. 1RXH J112331.7+014239 is clearly detected. 1RXH J124158.0+322848 is a strong source not far away from NGC4631.

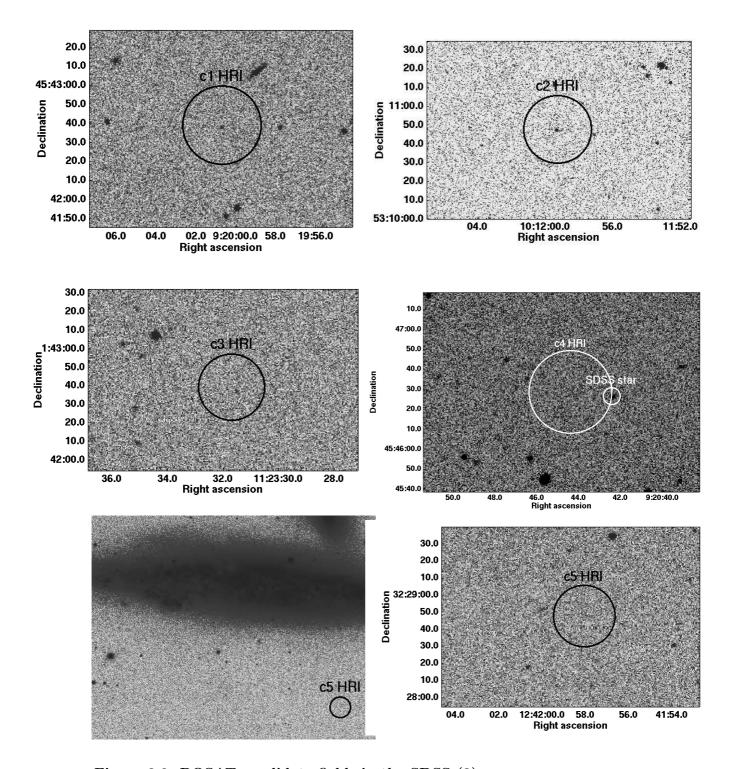


Figure 3.9: ROSAT candidate fields in the SDSS (2)

Shown are the SDSS g-band fields of the HRI candidates:  $c1_{HRI}$ ,  $c2_{HRI}$ ,  $c3_{HRI}$ ,  $c4_{HRI}$ ,  $c5_{HRI}$  (overview with nearby galaxy), and  $c5_{HRI}$ . The candidate source positions and their  $3\sigma$  uncertainties are indicated by the circles. There are two SDSS stars within the positional uncertainty of  $c1_{HRI}$  and one SDSS star in the fields of  $c2_{HRI}$ ,  $c3_{HRI}$ , and  $c5_{HRI}$  (small field). The brightest of these objects is g=21.9 mag (in the field of  $c2_{HRI}$ ). The g=20.6 mag star near  $c4_{HRI}$  is separated from the candidate position (uncertainty  $3\sigma=19.3$  mag) by 21''. For  $c6_{HRI}$  see Fig. 3.6.

**Discussion** In the following we discuss first the individual sources and then the aspects of the whole search for HRI candidates of X-ray thermal neutron stars in general.

 $c1_{HRI}$  is coincident with the catalogued 1RXH J092000.6+454239 and the X-ray detection is weak, but reasonable. There are two SDSS DR5 sources classified as 'stars' at 0.02' and 0.08' within the X-ray  $3\sigma$  positional error. The logarithmic X-ray-to-optical flux ratios are 1.1 and 1.9. Thus, it is unlikely that one of these objects is the X-ray counterpart if they are indeed stars. The one with  $\log (f_X/f_g) = 1.9$ , however, has a UV-excess given its color: u - g = -1.6 mag. However, the u magnitude of u = 22.9 mag is larger than those considered in the study by Richards et al. (2002). We classify this object as 'class B1'.

Besides a variability check at X-rays, the next step will be the closer investigation of at least the UV-excess object at optical wavelengths, e.g. by spectroscopy. There are no archival XMM-Newton observations.

 $c2_{HRI}$  is coincident with the catalogued 1RXH J101159.1+531047. The X-ray inspection shows a strong source. There is one SDSS DR5 source classified as 'star' at 0.01' and having a  $\log(f_X/f_g)$  of 0.9. Its u-g color is 0.53 mag, the u magnitude is 22.4 mag. Thus this object is a 'class B1' source. There are archival XMM-Newton observations for this source. Unfortunately EPIC-pn was in timing mode, only EPIC-MOS1 and EPIC-MOS2 images are available. Therefore, it is not possible to consider energies down to 150 eV for EPIC-pn as it is done in Sec. 3.3 where a algorithm dedicated to the EPIC-pn instrument is applied to remove the noise at such low energies. While the source is detected in the MOS-images (see Fig. 3.8), it is not included in the second XMM-Newton Serendipitous Source Catalogue (XMM-SSC2; pre-released 20.7.2006 by the XMM-Newton Survey Science Centre Consortium)<sup>1</sup>. From the EPIC source list (XMM Science Archive (XSA)<sup>2</sup>) we obtain the following hardness ratios in case of e.g. the EPIC-MOS1  $HR1_{MOS1} = 0.7^3$ ,  $HR2_{MOS1} = -0.7$ ,  $HR3_{MOS1} = -0.9$ ,  $HR4_{MOS1} = -0.5$  for count rates within [0.2, 12] keV of  $CR1_{MOS1} = 0.001$  cnts s<sup>-1</sup>,  $CR2_{MOS1} = 0.06$  cnts s<sup>-1</sup>,  $CR3_{MOS1} = 0.01$ cnts s<sup>-1</sup>,  $CR4_{MOS1} = 0.0008$  cnts s<sup>-1</sup>, and  $CR5_{MOS1} = 0.0002$  cnts s<sup>-1</sup>. Thus, the source seems to be a moderately soft source. One can convert the ROSAT count rate to a XMM-Newton count rate applying WebPIMMS<sup>4</sup> (Mukai, 1993). As a model spectrum for the conversion we use here and in the following a blackbody (50 eV or 90 eV) with interstellar absorption  $(N(H) = 2 \cdot 10^{20} \text{ cm}^{-2} \text{ or } 5 \cdot 10^{20} \text{ cm}^{-2})$ .

<sup>&</sup>lt;sup>1</sup>http://xmmssc-www.star.le.ac.uk/

<sup>&</sup>lt;sup>2</sup>http://xmm.vilspa.esa.es/external/xmm\_data\_acc/xsa/index.shtml

<sup>&</sup>lt;sup>3</sup>no errors listed by the XSA EPIC source list

<sup>&</sup>lt;sup>4</sup>http://heasarc.gsfc.nasa.gov/Tools/w3pimms.html

The overall XMM-Newton MOS count rate agrees with that of ROSAT HRI following WebPIMMS and considering error bars, e.g. of the assumed (blackbody) model temperature or absorbing column density. There are slightly less counts in the first band than predicted by WebPIMMS for a blackbody model. We note, however, that not all source photons may be collected due to the location near to a CCD gap. The source detection algorithm does take into account such overlapping sources by the exposure maps and the point spread function, but the derived values are nevertheless only an approximation.

Since the source is situated near a CCD gap, new XMM observations (preferably with EPIC-pn) would be a reasonable next step to be sure about the source characteristics. Optical spectroscopy would be important in order to investigate the nature of the SDSS object within the X-ray error circle.

 $c3_{HRI}$  is coincident with the catalogued 1RXH J112331.7+014239. Visual inspection shows a weak but reasonable X-ray source detection (Fig. 3.7). The SDSS DR5 object within its X-ray  $3\sigma$  positional error is a u=22.8 mag star, which has  $\log(f_X/f_g) = 1$  and u - g = 0.4 mag. We classify this source as 'class B1'. The archival XMM-Newton observations, which cover this sky region, are available for EPIC-pn Full Frame mode (thin filter). We investigate the data from 150 eV to 1 keV as decribed in Sec. 3.3, and obtain a count rate of  $0.0033 \pm 0.0005$  cnts  $s^{-1}$  and  $HR_{XMM} = 0.04 + / - 0.16$  (for bands [150, 500] eV, [0.5 keV,1 keV]; see Sec. 3.3 and Fig. 3.8). The XMM-SSC2 lists the following values for the energy range [0.2, 12] keV :  $CR_{PN} = 0.0107 \pm 0.0011$  cnts s<sup>-1</sup>, and  $HR1_{PN} = 0.30 \pm 0.14$ ,  $HR2_{PN} = -0.03 \pm 0.12$ ,  $HR3_{PN} = -0.37 \pm 0.14$  and  $HR4_{PN} = 0.15 \pm 0.21$ . The predicted XMM-Newton count rate, derived by WebPIMMS from the ROSAT count rate, differs by a factor of three from the actually measured values in the XMM-SSC2 energy range and by a factor of ten for the count rate in the energy band [0.15,1.0] keV, which is investigated in this work. This difference cannot be explained by different blackbody temperatures or absorbing column densities as checked by WebPIMMS. Furthermore, the countrates in the third to fifth band of the XMM-SSC2 are expected to be one or two orders of magnitudes lower than in the first two energy bands. The actually measured values are:  $CR1_{PN} = 0.0016 \pm 0.0004$  cnts  $s^{-1}$ ,  $CR2_{PN} = 0.0030 \pm 0.0005$  cnts  $s^{-1}$ ,  $CR3_{PN} = 0.0029 \pm 0.0005$  cnts  $s^{-1}$ ,  $CR4_{PN}=0.0013\pm0.0004~{\rm cnts~s^{-1}},~{\rm and}~CR5_{PN}=0.0018\pm0.0006~{\rm cnts~s^{-1}}~{\rm in}$ the five EPIC-pn energy bands used in the XMM-SSC2. This source does not seem to be a good candidate for a soft, absorbed blackbody spectrum and is therefore no good candidate for a M7-like object.

c4 $_{HRI}$  has no SDSS DR5 object within its positional errors. Visual inspection of the X-ray image (Fig. 3.7), however, gives rise to some doubts about the position of the X-ray source. There is positional coincidence with the catalogued 1RXH J092042.3+454630 within the errors, also with 2RXP J092042.7+454628. Yet, 1RXH J092042.3+454630 could be the counterpart of a star which is situated within the error circle of the 1RXH source. This star has  $g=20.609\pm0.033$  mag and it is just 1.7" outside the positional error of c4 $_{HRI}$ . The log  $f_X/f_{star_g}$  for c4 $_{HRI}$ , 1RXH J092042.3+454630 and 2RXP J092042.7+454628 are -0.06, 0.49 and 0.23 respectively (because of slightly different fluxes). The star is unlikely to be the counterpart to the 1RXH and 2RXP source, even if we take into account the errors in the X-ray flux and SDSS magnitude. It remains unclear whether two X-ray sources (c4 $_{HRI}$  and 1RXH J092042.3+454630) are observed or only one which is extended. Because of this uncertainty we classify c4 $_{HRI}$  as class '2' from X-ray screening. A deeper X-ray observation of higher spatial resolution could clarify this uncertainty.

 $c5_{HRI}$  is coincident with the catalogued sources 1RXH J124158.0+322848 and 2RXP J124158.0+322852 ( $HR1 = 0.48 \pm 0.59$ ,  $HR2 = -0.30 \pm 0.87$ , agreeing count rates). The only present SDSS DR5 source, classified as star, has u-g=1.2 mag, u=24.1 mag and  $\log(f_X/f_g) = 1.1$ . If indeed it is a star, it is unlikely to be the counterpart of the X-ray object, and it is also not a (photometric) quasar candidate. The source is uncomfortably close to NGC4631 (around 4'). However, in the archival XMM-Newton observation it seems to be clearly separated from NGC4631. Due to the extended Full Frame mode of EPIC-pn, an analysis following Sec. 3.3 is not possible. The XMM-SSC2 reports the following values in the energy range [0.2, 12] keV:  $CR_{PN} = 0.0012 \pm 0.009$  cnts s<sup>-1</sup>, and  $HR1_{PN} = 0.35 \pm 0.05$ ,  $HR2_{PN} =$  $0.11\pm0.04$ ,  $HR3_{PN}=-0.15\pm0.04$  and  $HR4_{PN}=-0.53\pm0.06$ . The XMM-Newton count rate for an absorbed blackbody, predicted by WebPIMMS from the ROSAT count rate, is an order of magnitude larger than the measured value listed in the XMM-SSC2. This indicates that a soft blackbody may not be the best model for the spectrum of this source. Since the source has sufficient counts (around 1100) we obtain a spectrum for its position from the EPIC-pn data and tested different model spectra in XSPEC for consistency. A blackbody turns out to be a bad model. We derive better agreements with the obtained source spectrum for a powerlaw model; a thermal bremsstrahlung spectrum is also more likely than an absorbed blackbody. Therefore,  $c5_{HRI}$  seems to be rather an AGN than a candidate for an M7-like object.

 $c6_{HRI}$  is coincident with the catalogued source 1RXH J130710.7+463530. As can be seen in the X-ray image, the object is relative close ( $\approx 4'$ ) to the targeted galaxy

cluster A1682 and an extragalactic counterpart seems more likely than a neutron star counterpart. Within the X-ray positional error there are three SDSS DR5 sources classified as stars. All are fainter than u=22.0 mag, two of them show UV-excess with u-g=-0.8 mag and 0.2 mag. We classify  $c6_{HRI}$  as 'class B2'. There are no archival XMM-Newton observations.

Chieregato et al. (2005) also searched for blank field sources in the ROSAT HRI dataset. In contrast to us they used the Brera Multiscale Wavelet catalogue (BMW-HRI; Panzera et al. 2003) which is based on a wavelet transform detection algorithm (Lazzati et al., 1999, Campana et al., 1999). This algorithm is particularly powerful in dealing with extended sources. Chieregato et al. (2005) reported a final blank field list of three transient sources and one persistent source. None of our identified candidate fields was found by Chieregato et al. (2005) because they searched only for sources brighter than  $2.7 \cdot 10^{-13}$  erg s<sup>-1</sup> cm<sup>-2</sup> while our candidate sources have X-ray fluxes of around  $10^{-14}$  erg s<sup>-1</sup> cm<sup>-2</sup>. On the other hand we do not find their steady candidate 1BMW042142.4-571541 because we apply a hardness ratio cut, while there are no hardness ratios in the BMW-HRI. 1BMW042142.4-571541 has a hardness ratio of  $HR_{HRI} = 0.51 \pm 0.04$  in the HRI catalogue by R. Supper and W. Voges. Thus, it is excluded from our initial selection. This source is also not in the SDSS DR5 footprint.

Applying our search criteria we do not recover the only known member of the M7 situated in the area of the sky covered by the SDSS DR5 footprint and which was observed by the ROSAT HRI. RX J1605.3+3249 is excluded since we consider only sources with off-axis angles above 2'. Furthermore, RX J1605.3+3249 has a hardness ratio above our  $HR_{HRI}$  cut; see Table E.1 in the Appendix. This example shows the drawback of applying the often unreliable  $HR_{HRI}$ . We therefore plan to expand the search to the remaining HRI point sources with  $HR_{HRI} > 0.2$ .

Interestingly, available archival XMM-Newton observations lead to the exclusion of two of three candidates. For the remaining one, even deeper X-ray observations are needed to get more constraints on its nature. Given the source locations on the sky at high galactic latitudes (see Fig. 3.18) it is not surprising that there is a large amount of confusion, most likely from extragalactic sources. Only further X-ray and optical observations can clarify the spectral properties of the X-ray candidate isolated neutron stars.

## 3.3 XMM-Newton pointed observations

The modern X-ray satellites XMM-Newton and Chandra (see Appendix A.1 for more information on both) provide the opportunity to find even fainter X-ray sources than with ROSAT. Thanks to its larger collecting area the XMM-Newton satellite is more sensitive than Chandra, especially at the soft energies interesting for the search for M7-like objects. Here, EPIC-pn is the most sensitive and stable instrument, thus the instrument of choice for a candidate search. The energy interval, supported by the standard reduction with the Science Analysis System (SAS¹), ranges from 0.2 keV to 12 keV for XMM observations. For example, this energy range was applied for the first XMM-Newton Serendipitous Source Catalogue (1SSC²). We started by quering this catalogue for soft sources with comparable hardness ratios as the M7, e.g. RX J0720.4-3125. However, visual inspection of the X-ray images revealed all new candidates to be artefacts from bright sources, unlikely detections or extended sources. In the following we describe our started program to identify soft sources in the deepest XMM-Newton EPIC-pn pointings. In contrast to the standard analysis we start the data reduction at an energy of 150 eV instead of 200 eV.

Data processing Unfortunately, the EPIC-pn X-ray data below 200 eV are considerably affected by detector effects, which increase towards the lowest transmitted energies. Dennerl et al. (2004) reported about the detector noise, which becomes significant for energies below 200 eV. Additionally they pointed out the role of incorrect offset maps resulting in bright patches in the low energy images. Dennerl et al. (2004) developed a method to overcome these problems, the task epreject, which is implemented in SAS starting from version v6.0 on. Applying epreject in the pre-processing step epchain results in a correction of the energy scales in specific pixels and in flagging, on a statistical basis, the amount of events which correspond to the expected detector noise. The pre-processing of the XMM-data in the internal MPE archive is done by M. Freyberg (MPE). We start in the following from this internal archive with epreject-pre-processed data.

While in principle it is possible to consider now the lowest transmitted energy at 120 eV, tests showed that a lower energy limit of around 150 eV is an acceptable choice considering the still present noise features in the data. We note that it may be possible to go to even lower energies than 150 eV if the epreject noise parameters are adapted individually for each observation. For our data the standard noise parameters of epreject have been used as listed in XMM-Newton SAS documentation. The whole work was done with

<sup>&</sup>lt;sup>1</sup>see e.g. http://xmm.vilspa.esa.es/sas/

<sup>&</sup>lt;sup>2</sup>e.g. on ViZier: http://vizier.u-strasbg.fr/viz-bin/Cat?IX/37

XMM-Newton SAS 6.1.0. We define two bands to use in the following for our search: the 'soft' band1 ranges from 150 eV to 500 eV, the 'hard' band2 ranges from 500 eV to 1 keV. One has to consider carefully bad pixels in band1. While most bad pixels are known in the standard energy range, this is not the case at these low energies. Mostly, the bad pixels are hot pixels. To find prominent hot pixels we merged several deep exposures without bright sources and treated each of the 12 CCDs individually. The hot pixels found in this way have been checked for occurrence in the individual exposures. Hot pixels present in nearly all observations (usually with different strength) are flagged as bad pixels in all following observations (see Table E.4 in the Appendix). However, we find also pixels which are only 'hot' in one exposure. Therefore, we apply the task badpixfind additionaly to the bad pixel mask of permanent hot pixels. To derive the best result we estimate the threshold and the noise for each CCD individually by the corresponding background CCD image. Overall, the steps in data analysis can be summarised as below: (i) XMM-Newton observations longer than 10 ksec are selected. Those with expected high source confusion are excluded, e.g. with M31 as target. In this work we analyse 42 pointings. (ii) Noise events, flagged according to epreject in the pre-processed data, are removed in the two bands. We consider only single events in band1 [150, 500] eV, singles and doubles in band2 [0.5, 1.0 keV. (iii) The background map is computed for each CCD individually, the mean value contributes to the threshold parameter in badpixfind, as well as the noise found in the background map. The bad pixels found by badpixfind and by our bad pixel mask are flagged and neglected in further analysis. (iv) The science X-ray images in both bands are derived taking into account good time intervals, vignetted exposure maps and out-oftime events. Background maps are created for the following source detection. The SAS tasks evselect, eexmap, emask, eboxdetect, esplinemap and HEASARC's Ftools<sup>1</sup> (Blackburn, 1995) have been applied for this purpose. (v) Sources are detected in the the science X-ray images using also the background maps, the vignetted exposure maps and the SAS-tasks eboxdetect, emldetect. Only sources with detection likelihoods larger than 10 have been considered further. A hardness ratio is defined by emldetect in the usual way  $HR_{XMM} = (band2 - band1)/(band1 + band2)$ . (vi) Visual inspection of all sources with  $HR_{XMM} < 0.0$  is necessary due to still present noise features. The sources are flagged as noise or hot pixel, apparent extended source, artefact; possible, but very faint detection (flag 2), detection of high probability (flag 1). (vii) The source catalogues of the individual 42 observations are merged to one catalogue.

Of the 152 XMM-sources with  $HR_{XMM} < 0.0$  and visual inspection flags 1 or 2 (bright and possible faint detections) 70 are covered by the SDSS DR5 footprint (17 pointings). The search for SIMBAD-objects or SDSS DR5 galaxies within the  $3\sigma$  XMM-Newton po-

<sup>&</sup>lt;sup>1</sup>http://heasarc.gsfc.nasa.gov/ftools/

sitional error (including  $3\sigma_{sys}=6''$  systematic error)<sup>1</sup> reduced the number to 25 candidate fields. The photometry of the objects classified as 'stars' in SDSS DR5 is used to calculate the u-g-color and the  $\log{(f_X/f_g)^*}$ . Similarly to the ROSAT pointings we exclude fields with probable UV-excess objects satisfying u-g<0.6 mag and  $u\leq22.0$  mag. To exclude at least stars as probable counterparts we apply the cut of  $\log{(f_X/f_g)^*}<0$  as found e.g. by Zickgraf et al. (2003). These two conditions exclude all but one field with SDSS DR5 objects present. The star in the one exceptional field has g=24.5 mag, but u-g=-0.1. Thus this field is classified as 'class B'. The 13 remaining blank fields are classified as 'class A'. The faintest SDSS DR5 objects within 1 arcmin around the X-ray position are taken to derive the reached  $\log{(f_X/f_g)}$ , which ranges from 0.3 to 1.7 for the 13 fields. Thus, AGNs cannot be excluded as possible counterparts in most cases and deeper optical observations would be definitely needed to constrain the nature of these candidate fields.

A summary of the fields' properties can be found in Table 3.4, the correponding X-ray images for the bands 150 eV to 500 eV ('soft band'), and 500 eV to 1 keV ('hard band') in Fig. 3.10 to 3.15 as well as the SDSS g images of the candidates in Fig. 3.16 and 3.17. In tab. 3.4 the sources are also classified according to their X-ray properties (hardness ratios, detection likelihood) by visual inspection. We discuss each candidate briefly in the following, especially the correspondence of the sources identified to those detected also in the XMM-SSC2, which covers all the relevant exposures.

 $<sup>^1</sup>$ the quoted  $1\sigma_{sys}$  is <2'' for the XMM SSC2, see also http://xmmssc-www.star.le.ac.uk/newpages/UserGuide\_2xmmp.html#Abstract

#### Discussion

- XMMc1 is a rather weak detection in a noisy image (Fig. 3.10). It is detected only in the soft band with a relatively high count rate. Other X-ray observations are needed to establish the existence of this source. No source is reported at this location by the XMM-SSC2 in the energy range from 200 eV to 12 keV. There are no SDSS DR5 objects within the X-ray  $3\sigma$  positional error circle.
- XMMc2 is detected only in the soft band in a noisy image (Fig. 3.10). It seems likely that this source is actually a noise detection. However, other X-ray observations may confirm also its existence. No source is reported by the XMM-SSC2 in the energy range from 200 eV to 12 keV. There are no SDSS DR5 objects within the X-ray  $3\sigma$  positional error circle.
- XMMc3 has a detection likelihood of around 20 and it is clearly visible in the soft band in Fig. 3.11. However, the pattern of illuminated pixels around the source is similar to the noise pattern, which is especially likely at the CCDs inner short border (the short border is pointing towards the center of the instrument, situated opposite to another CCD; the CCD is in a row with five other CCDs). Therefore, a noise detection cannot be excluded and should be checked by another X-ray exposure. No corresponding source is reported by the XMM-SSC2 in the energy range from 200 eV to 12 keV. There are no SDSS DR5 objects within the X-ray  $3\sigma$  positional error circle.
- XMMc4 seems to correspond to a noise detection given the pattern of the illuminated pixels and its location close to the inner short CCD border (see Fig. 3.11). Therefore, we currently regard this source as a bad candidate. However, other X-ray observations may confirm this source. No corresponding source is reported by the XMM-SSC2 in the energy range from 200 eV to 12 keV. There are no SDSS DR5 objects within the X-ray  $3\sigma$  positional error circle.
- XMMc5 has a low detection likelihood just as the previous sources, but it is more distant from the CCD border (see Fig. 3.12). Noise patterns are less pronounced there and the source seems to be a reasonable soft detection according to our visual inspection. Its hardness ratio ( $-0.58 \pm 0.28$ ) points to a soft source. Interestingly, there is a correponding XMM-SSC2 source known (coincidence within the  $3\sigma$  positional errors), but only from an observation we did not analyse before (Revolution 666 instead of revolution 665 reported here) The reported EPIC-pn parameters for the very faintly detected 2XMMp J140055.3+030006 are: detection likelihood of only

- 8.2, an on-time of 43 ks,  $CR_{PN} = 0.0022 \pm 0.0006$  cnts s<sup>-1</sup>,  $HR1_{PN} = -0.07 \pm 0.31$ ,  $HR2_{PN} = -0.13 \pm 0.36$ ,  $HR3_{PN} = -0.31 \pm 0.50$  and  $HR4_{PN} = 0.35 \pm 0.53$ . There are no SDSS DR5 objects within the X-ray  $3\sigma$  positional error circle of XMMc5. Further X-ray observations and deeper optical images would be the next steps in investigating the properties of this source.
- XMMc6 is a faint source, detected mainly in the soft band (see Fig. 3.12). There is a strong source closeby and other X-ray sources around XMMc6. It is not clear whether we see point sources or extended emission. XMMc6 may belong to the extended emission and must be regarded as a rather uncertain isolated neutron star candidate. No corresponding source is reported by the XMM-SSC2 in the energy range from 200 eV to 12 keV. There are no SDSS DR5 objects within the X-ray  $3\sigma$  positional error circle.
- XMMc7 is a weak, but reasonable source according to our visual inspection, fairly well detected in the soft band (see Fig. 3.13). The XMM-SSC2 reports also a detection at this position. 2XMMp J130553.6+175213 has the following values in the energy range [0.2,12] keV with the EPIC-pn instrument:  $CR_{PN} = 0.0035 \pm 0.0007$  cnts s<sup>-1</sup>, detection likelihood of 24.5,  $HR1_{PN} = -0.01 \pm 0.21$ ,  $HR2_{PN} = -0.29 \pm 0.24$ ,  $HR3_{PN} = -0.07 \pm 0.34$   $HR4_{PN} = -0.03 \pm 0.53$ . Two thirds of the counts are in the first two bands up to 1 keV. So, this source may have indeed a relatively soft spectrum and would be therefore a good candidate for a M7-like object. However, the X-ray source is rather faint and further deeper obervations are needed to verify the indication of a soft spectrum. There are no SDSS DR5 objects within the X-ray 3 $\sigma$  positional error circle.
- XMMc8 is a faint source, but is detected in the soft and in the hard band (see Fig. 3.13). While its existence seems likely if visually inspected, further deeper X-ray observations would be useful for verification and spectrum determination. There are no sources known in the XMM-SSC2 within the  $3\sigma$  positional uncertainties. This could be an indication of a very soft spectrum, since we detect this source with a relatively high likelihood of around 20 for the energy interval [0.15,1] keV, while the XMM-SSC2 operates at [0.2,12] keV and does not even list the source with a likelihood of 10. Therefore, XMMc8 seems to be a reasonable candidate for an M7-like neutron star.
- XMMc9 is detected in the soft band, but not in the hard band. From its location close to the inner short CCD border and the present noise pattern on this CCD in this observation (see Fig. 3.14), it is likely that XMMc9 is actually a noise detection.

Therefore it is not a good candidate for an isolated neutron star. No corresponding source is reported by the XMM-SSC2 in the energy range from 200 eV to 12 keV. There are no SDSS DR5 objects within the X-ray  $3\sigma$  positional error circle.

XMMc10 is very faintly detected in the soft and hard X-ray band (see Fig. 3.14). While its existence must be considered with caution, this source is also reported in the XMM-SSC2 for two observations. One of them is analysed here – the revolution number (REVID) 734 (detection likelihood in XMM-SSC2: 13), the other was observed at REVID= 623 in the same mode but in half of the time (detection likelihood in XMM-SSC2: 11). As the obtained parameters agree within the errors, we list here only the values of 2XMMp J104418.6+212403 obtained in REVID=734 with EPIC-pn from 200 eV to 12 keV:  $CR_{PN} = 0.0015 \pm 0.0004$  cnts s<sup>-1</sup>,  $HR1_{PN} = 0.07 \pm 0.24$ ,  $HR2_{PN} = -0.32 \pm 0.28$ ,  $HR3_{PN} = -1.00 \pm 0.69$ , no reported  $HR4_{PN}$ . This source may be indeed a relatively soft X-ray source. Deeper X-ray observations would be the next step in constraining the source spectrum. There are no SDSS DR5 objects within the X-ray 3 $\sigma$  positional error circle.

XMMc11 is detected only in the soft X-ray band (see Fig. 3.15). From its location at the inner short border of the CCDs and its pattern of illuminated pixels, it seems likely that XMMc11 is actually a noise detection. Therefore, it is regarded as a bad candidate for a M7-like object. No corresponding source is reported by the XMM-SSC2 in the energy range from 200 eV to 12 keV. There are no SDSS DR5 objects within the X-ray  $3\sigma$  positional error circle.

XMMc12 lies in a region of high X-ray background (see Fig. 3.15). Furthermore it is located close to the inner short border of a CCD, where weak noise is also present. Its pattern of illuminated pixels, however, is not typical for a noise structure. Currently it is not clear whether this source exists; more X-ray observations are needed. No corresponding source is reported by the XMM-SSC2 in the energy range from 200 eV to 12 keV. XMMc12 is the only source with a SDSS DR5 object, classified as star, within its  $3\sigma$  positional error circle. This SDSS star shows UV-excess, but it fainter than the SDSS 95% completness limit u=22 mag, up to which Richards et al. (2002) tested their color cuts. Because of these optical properties XMMc12 is classified as class B.

In conclusion, we identify three of these 12 sources as good INS candidates for further investigation. The X-ray properties of four are rather uncertain and it is difficult to decide whether we are dealing with good or bad candidates. Five sources are excluded as likely noise detections. We note that due to the high galactic latitudes of the candidates (see

Fig. 3.18) it is very probable that the source list is confused by extragalactic sources. In particular, we cannot exclude AGNs as counterparts due to the faintness of the X-ray sources and the limited sensitivity of the SDSS, thus low limiting values of  $\log (f_X/f_q)$ .

We identified with our method new soft sources (XMMc8, c6, and c12) that are not likely to be noise and are not found by the standard reduction in the energy range 200 eV to 12 keV (as documented by the XMM SSC2). Source confusion with a noise pattern is still a problem when applying the new SAS task epreject. Definitely, visual inspection and often longer X-ray observations for the faint sources are needed to verify these objects. It may be useful to include energies higher than the here cosidered 1 keV for completeness in future versions of our catalogue of soft sources.

Table 3.4: Candidate fields found with XMM-Newton EPIC-pn FF pointings

Listed for each candidate are: the J2000 position (RA, DEC), the positional error (p.e.), the source detection likelihood SL, the count rate CR, the collected counts and the hardness ratio between the bands 150 eV-500 eV and 500 eV-1 keV. The candidates are classified as A or B according to their SDSS properties (see text). The number in the classification scheme refers to the X-ray properties and stands for 1-good candidate for a M7-like NS, because detection and hardness ratios are OK for a candidate, 2 - X-ray detection is still uncertain, and 3 - probable noise detection or unfavourable properties (e.g. hardness ratios). The column SDSS DR5 lists the g magnitude of the faintest object (preferably classified stars) within 1' around the X-ray source, if there are no SDSS DR5 sources present within the X-ray positional error. The  $maximal\ reached\ \log\ (f_X/f_g)^{MAX}$  is estimated by these faint SDSS DR5 objects and noted in the next-to-last column. The last column lists whether the candidates are known from the XMM-SSC2 (Y/N). In all cases, the known XMM-SSC2 sources do not exclude the interpretation of the X-ray detection as an INS candidate.

| Name   | RA       | DEC     | p.e.   | SL   | CR                            | counts        | $HR_{XMM}$       | class | SDSS DR5   | $\log (f_X/f_g)^{MAX}$ | SSC2 |
|--------|----------|---------|--------|------|-------------------------------|---------------|------------------|-------|------------|------------------------|------|
|        | deg      | $\deg$  | arcsec |      | $10^{-3} {\rm cnts \ s^{-1}}$ | $\mathbf{s}$  |                  |       | mag        |                        |      |
| XMMc1  | 334.5990 | 0.3959  | 8.0    | 10.9 | $1.64 \pm 0.42$               | $36 \pm 9$    | $-1.0 \pm 0.2$   | A2    | 26.1       | 1.0                    | N    |
| XMMc2  | 334.3508 | 0.3320  | 8.0    | 10.8 | $0.52 \pm 0.18$               | $28 \pm 10$   | $-1.0 \pm 0.5$   | A3    | 25.4       | 0.27                   | N    |
| XMMc3  | 207.3378 | 26.3034 | 7.7    | 19.2 | $2.13 \pm 0.43$               | $54 \pm 11$   | $-0.9 \pm 0.1$   | A3    | 26.5       | 1.3                    | N    |
| XMMc4  | 223.5344 | 3.5303  | 7.7    | 10.9 | $1.89 \pm 0.49$               | $47 \pm 12$   | $-0.51\pm0.26$   | A3    | 24.9       | 0.6                    | N    |
| XMMc5  | 210.2293 | 3.0019  | 9.1    | 10.4 | $1.38 \pm 0.42$               | $32 \pm 10$   | $-0.58 \pm 0.33$ | A1    | 25.7       | 0.8                    | Y    |
| XMMc6  | 203.6518 | 37.9582 | 7.9    | 10.6 | $0.62 \pm 0.17$               | $38 \pm 10$   | $-0.58\pm0.28$   | A2    | 25.5       | 0.4                    | N    |
| XMMc7  | 196.4735 | 17.8705 | 8.3    | 15.8 | $1.85 \pm 0.40$               | $48 \pm 10$   | $-0.25\pm0.22$   | A1    | 24.6       | 0.5                    | Y    |
| XMMc8  | 193.3594 | 15.4948 | 8.7    | 19.7 | $3.46 \pm 0.73$               | $52 \pm 11$   | $-0.49\pm0.22$   | A1    | 25.9       | 1.3                    | N    |
| XMMc9  | 161.1598 | 21.5177 | 6.6    | 74.4 | $1.90 \pm 0.23$               | $114\pm14$    | $-1.00\pm0.04$   | A3    | 25.4       | 0.8                    | N    |
| XMMc10 | 161.0790 | 21.4008 | 7.9    | 16.0 | $1.65 \pm 0.37$               | $57 \pm 12.6$ | $-0.17\pm0.22$   | A2    | 26.1       | 1.1                    | Y    |
| XMMc11 | 163.5209 | 57.3294 | 7.1    | 20.3 | $5.73 \pm 1.17$               | $50 \pm 10$   | $-1.00\pm0.06$   | A3    | 26.2       | 1.63                   | N    |
| XMMc12 | 46.5510  | -0.0112 | 12.1   | 12.5 | $1.30 \pm 0.33$               | $49 \pm 12$   | $-0.74 \pm 0.23$ | B2    | $24.8^{1}$ | $0.4^{1}$              | N    |

 $<sup>^1</sup>$  corresponds to the only SDSS DR5 object (classified as star) within the positional error (u-g=-0.1<0.6 mag, but u=24.7 mag)

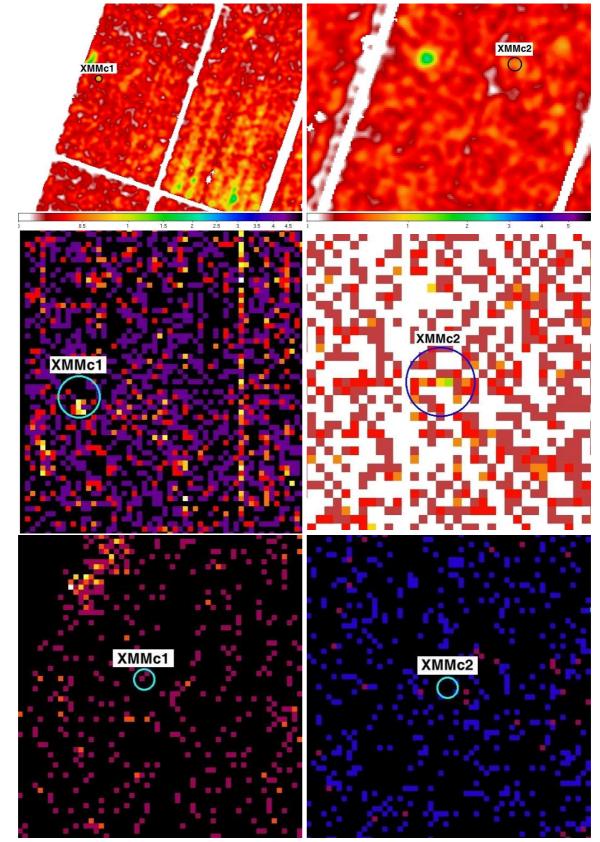


Figure 3.10: The X-ray images of the XMM-Newton candidates (1)

The first row shows the smoothed broad band [0.15,1] keV XMM-Newton images to illustrate the source locations comparing to the overall background and the noise pattern in the source neighbourhood. The radius of the sources corresponds to the  $3\sigma$  positional uncertainty (see Table 3.4). The second row shows the soft band [0.15,0.50] keV images of the particular CCDs, where the sources are located on. These images are plotted in RAWX-RAWY-CCD coordinates to identify easier the typical noise pattern of the soft band. The third row represents the corresponding hard band [0.5, 1.0] keV images of these CCDs (in usual sky coordinates). For better visibility no coordinates are plotted. The color scales for the second and third row are also skipped as a higher number of counts is usually easy to identify by neighbouring sources or deviating count patterns.

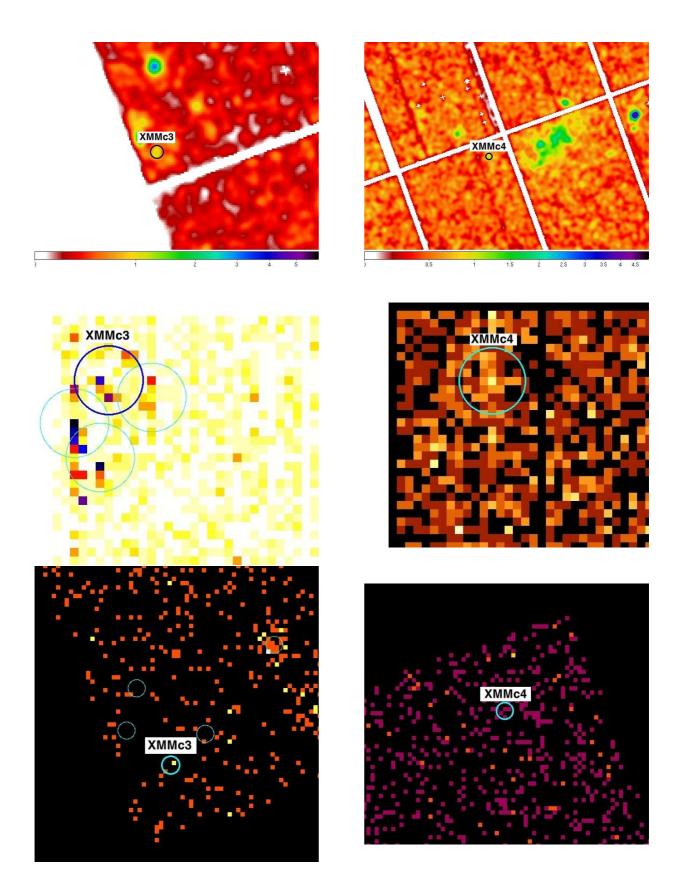


Figure 3.11: The X-ray images of the XMM-Newton candidates (2) see Figure 3.10 for description.

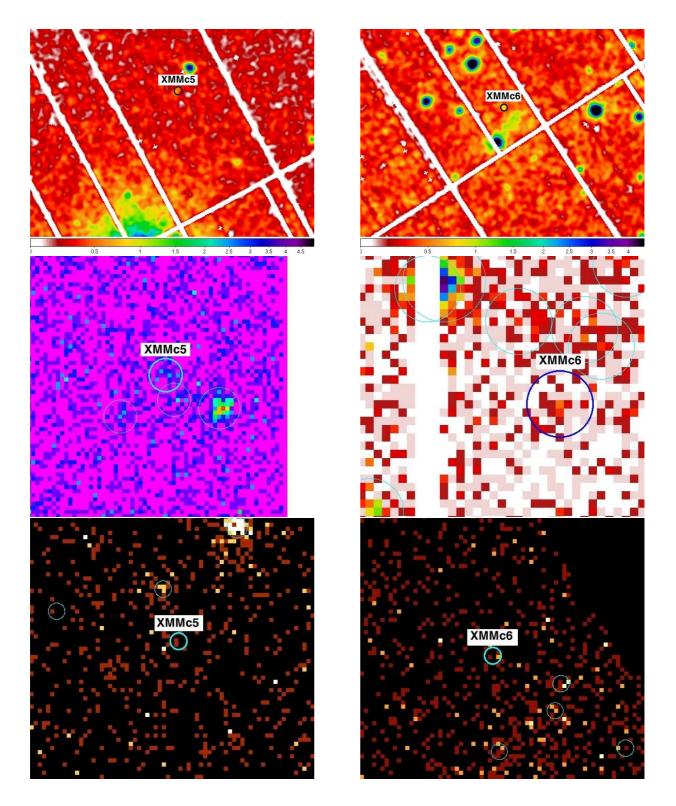


Figure 3.12: The X-ray images of the XMM-Newton candidates (3) see Figure 3.10 for description.

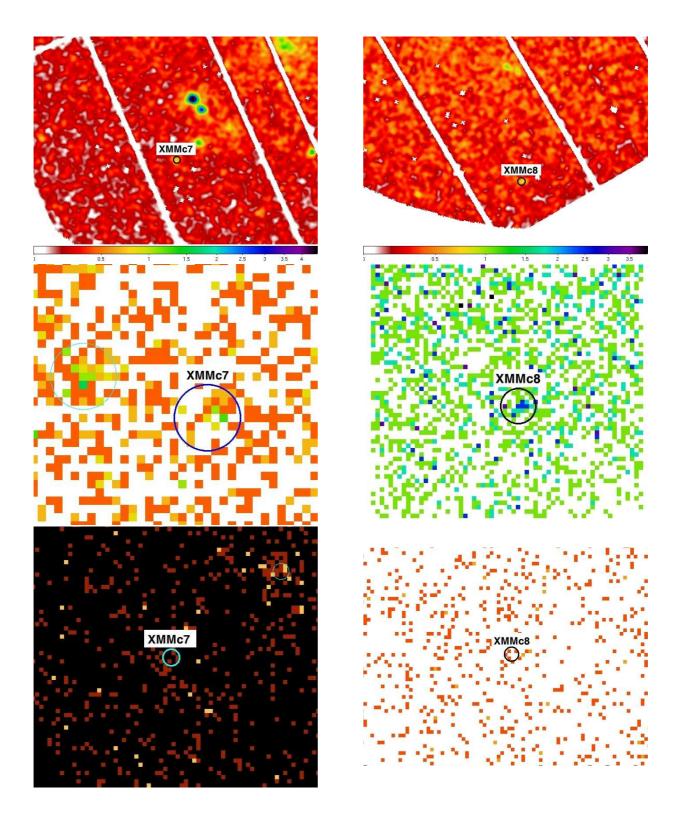


Figure 3.13: The X-ray images of the XMM-Newton candidates (4) see Figure 3.10 for description.

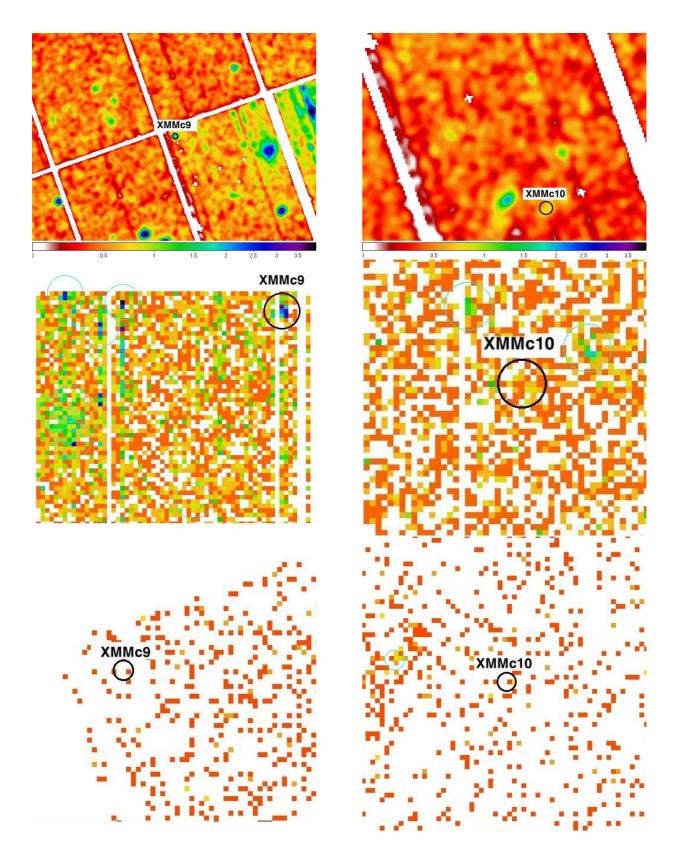


Figure 3.14: The X-ray images of the XMM-Newton candidates (5) see Figure 3.10 for description.

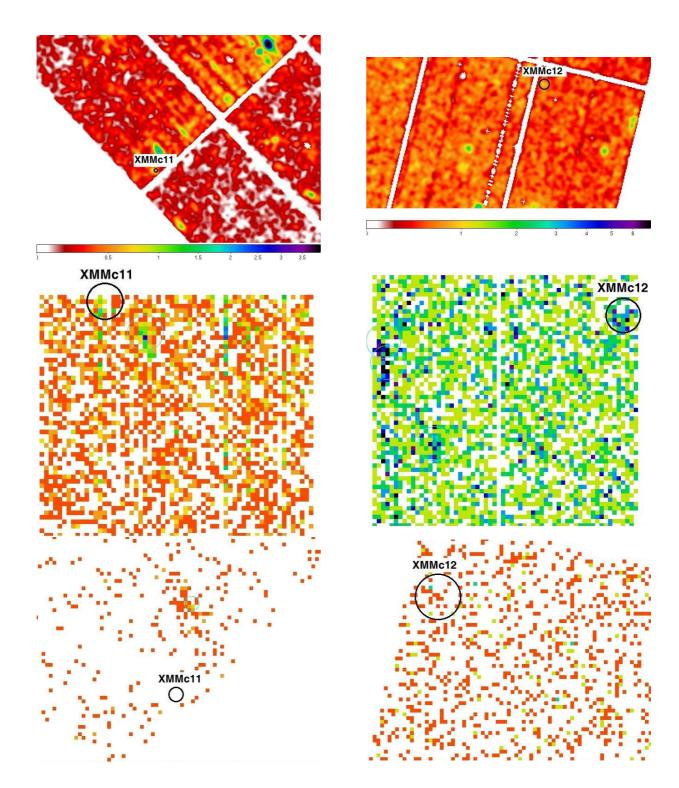


Figure 3.15: The X-ray images of the XMM-Newton candidates (6) see Figure 3.10 for description.

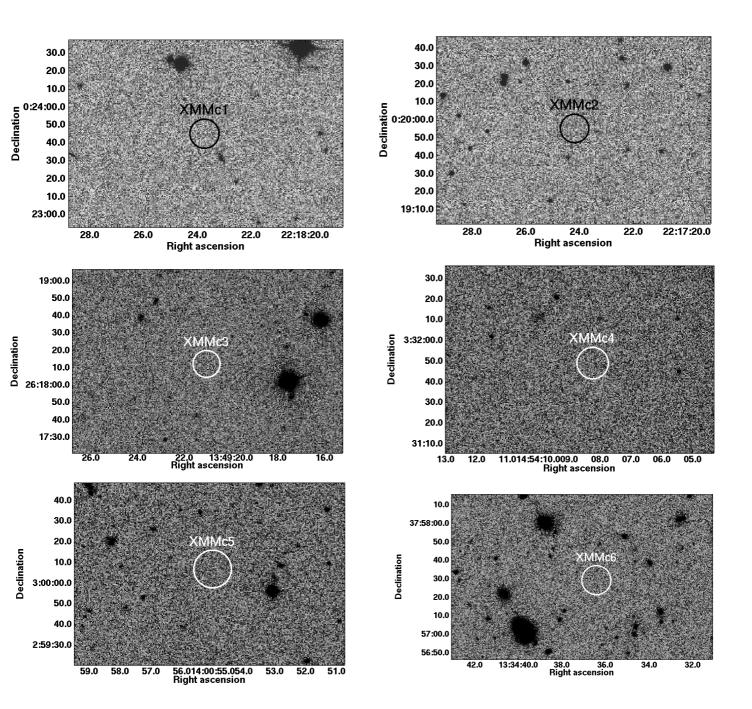


Figure 3.16: XMM-Newton candidate fields in the SDSS (1) Shown are the SDSS g-band fields of the theXMM-Newton candidates: The candidate source positions and their  $3\sigma$  uncertainties are indicated by the circles. There are no SDSS objects with the positional error of the XMM candidates or close to.

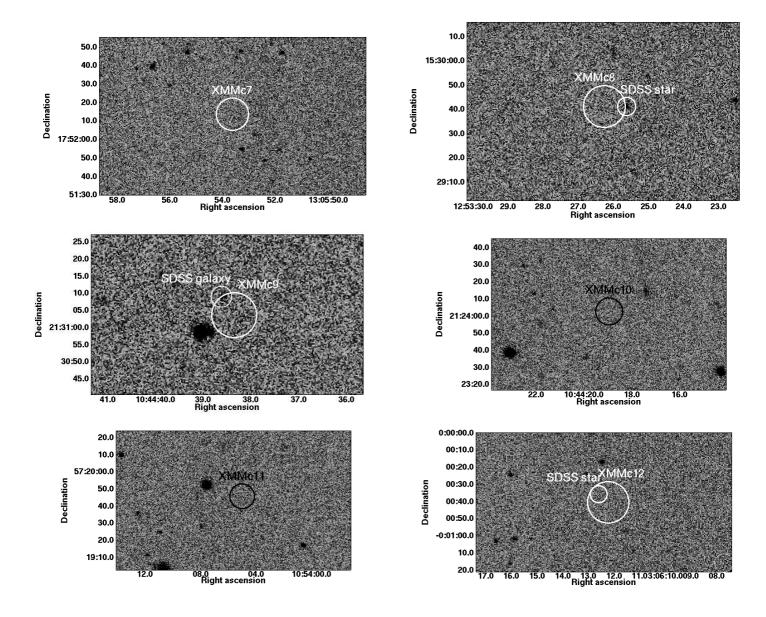


Figure 3.17: XMM-Newton candidate fields in the SDSS (2) Shown are the SDSS g-band fields of the theXMM-Newton candidates: The candidate source positions and their  $3\sigma$  uncertainties are indicated by the circles. The SDSS star just outside (8.9") the error circle of XMMc8 has g=22.0 mag, the SDSS galaxy just outside (6.7") the error circle of XMMc9 has g=22.7 mag, and the SDSS star in the error circle of XMMc12 has g=24.8 mag.

## 3.4 Conclusions

We presented several candidate isolated neutron stars selected from the ROSAT All Sky Survey, the ROSAT PSPC and HRI pointings as well as some of the deepest XMM-Newton observations. As outlined in Sec. 3.1 the number of RASS candidates is larger than the expected number of neutron stars following our population synthesis models (Sec. 2). However, it is very likely that we miss isolated neutron stars in fields where unrelated optical SDSS sources are present. The confusion rate by AGNs, especially those with high X-ray to optical flux ratios, is expected to be relatively high given the galactic latitudes of the candidates (Fig 3.18). The ROSAT and XMM-Newton pointings cover only a small region of the sky which was investigated by the SDSS. Furthermore they have each different exposures, thus the detected X-ray sources can reach different count rates. So, we have no homogenous sample to compare with predictions. One can test only very crudely whether the candidate number is above or below the expectation. For ROSAT HRI pointings we consider the mean count rate of the listed six candidates (including those two which are finally excluded),  $12.7 \cdot 10^{-4}$  cnts s<sup>-1</sup>, and apply a factor of five (for soft sources (Sasaki et al., 2000)) to derive the PSPC count rate, which is plotted in our  $\log N$ - $\log S$  curves (Sec. 2). The SDSS DR5 covers around 19% of the sky, the HRI only 1.9%. Assuming a homogenous distribution of the HRI pointings within the SDSS data, one would expect 0.3% of the predicted neutron star number for the full sky at a PSPC count rate of  $6.3 \cdot 10^{-3}$  cnts s<sup>-1</sup>. This corresponds to an expected NS number of 0.13 for the extinction ISM model and 0.08 in case of the analytical ISM model (see Fig. 2.7). So it is rather unlikely that an INS is detected in the HRI pointings covered by the SDSS, especially when taking into account the spatial distribution of the predicted neutron stars in comparison to the candidate locations (see Fig. 3.18). Our high HRI candidate number will be probably reduced by follow-up observations. We note that while RX J1605.3+3249 is located within the SDSS area, it is excluded by our off-axis cut. With this cut the area covered by each HRI pointing is slightly smaller (by one percent) than assumed above. Applying the same procedure on the ROSAT PSPC pointing (sky coverage 17.3%) sources, the expected values are 3.3% of the predicted neutron star number at  $2.8 \cdot 10^{-3}$  cnts s<sup>-1</sup>. This corresponds to 1.0 expected M7-like neutron star in case of the analytical ISM model and 1.6 objects in case of the ISM model based on the extinction study by Hakkila et al. (1997). Here, our one good candidate is in agreement with the expectations. However, firstly one has to consider again the already known RX J1605.3+3249 which we miss only because of our off-axis cut; secondly the predicted neutron stars are inhomogenously distributed and the candidates are situated at high galactic latitudes (see Fig. 3.18).

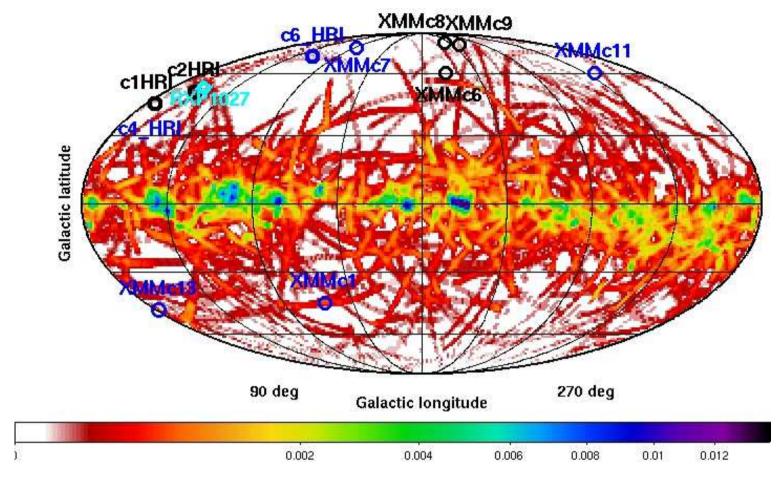


Figure 3.18: Pointing candidate positions on the sky

Shown are the locations of the HRI, PSPC and XMM pointing candidates which passed the screening process as class 1 (black and cyan) and those which are more uncertain due to unconstraining X-ray detections (class 2, blue). The background image correponds to the predicted neutron star number per square degree as derived in Chapter 2. The image is a Mollweide projection in galactic coordinates (positive galactic latitudes are up). It is the same result as Fig. 2.18, obtained for an inhomogenous progenitor distribution and the 3D-ISM model based on the extinction study by Hakkila et al. (1997) to consider the interstellar absorption (for detailed description and discussion see Chapter 2). All candidates are situated at high galactic latitudes where source confusion with extragalactic sources (e.g. AGNs) is more likely than in the galactic plane. For further discussion, see Sec. 3.2 and 3.3.

Due to the smaller overlap between deep XMM-Newton EPIC-pn observations and SDSS DR5, we can expect even fewer INS candidates here: Of the 42 considered deep XMM pointings only 17 are in principle within the SDSS DR5 footprint (tested only for one coordinate pair per pointing). Thus, only 0.006% of the predicted NS number at  $CR_{XMM} = 2.2 \cdot 10^{-3}$  cnts s<sup>-1</sup> could be expected to be found. This correponds to an expected candidate number of 0.003 (analytical ISM model, Fig 2.20). Taking into account the inhomogenity of the predicted neutron star distribution and the candidate locations it remains unclear whether there is actually any new isolated NS among the XMM candidates (see Fig. 3.18).

The relatively large positional error circle of ROSAT usually includes many possible optical counterparts. The method of identifying 'optically blank' fields, developed by M. Agüeros for the RASS, is able to identify many of those sources as 'unlikely' counterparts. However, many X-ray sources may have been excluded, which have an unrelated optical source with unfavourable properties within their positional errors. Therefore, we may miss good candidates and certainly will finally underestimate the number of observable isolated neutron stars within the SDSS DR4 footprint and the RASS. Better X-ray positions play a key role to avoid the problem of confusing optical sources. While there is only one of the discussed seven ROSAT pointing candidates without any optical source within its positional error, all except one discussed XMM-Newton candidate fields are devoid of any SDSS DR5 object thanks to the better spatial resolution of XMM-Newton. However, here we have the problem of very faint X-ray fluxes and poor sky coverage. Considering the ROSAT data, the SDSS DR5 has been proven to be a powerful accompanying optical survey which can be used to exclude many unlikely candidates, on the one hand by optical colors and on the other hand by X-ray-to-optical flux ratios. However, the fainter the X-ray candidates the deeper the optical observations that are needed. In case of the faint XMM-Newton candidates, even the SDSS DR5 is only capable to exclude stars as possible counterparts by the X-ray-to-optical flux ratios. Thus, deeper follow-up observations in the optical wavelength regime are definitely needed to get better constraints on the flux ratios. A future search strategy for faint Magnificent-Seven-like objects may be more successful by cross-correlating X-ray data of high spatial resolution with archival optical data even deeper than SDSS DR5, e.g., from the HST, VLT or Keck telescope. We note here the planned X-ray All Sky Survey of eROSITA which is expected to have an angular resolution of < 25'' and to be 30 times more sensitive than the RASS (Predehl et al., 2006). eROSITA's CCD technology is based on an improved concept of the successful XMM-Newton EPIC-pn CCDs. While the noise at low X-ray energies is expected to be much lower compared to the EPIC-pn CCDs (Meidinger et al., 2006) the influence of the eROSITA filter actually reduces the sensitivity to or below that of ROSAT in case of energies lower than 0.2 keV (P. Predehl, personal communication). Using a preliminary eROSITA response matrix one can estimate that source detections are possible with approximately one eighth of the RASS count rate after the 4 years of planned survey observations (F. Haberl, personal communication). Thus, one would expect roughly two times more detectable NSs with strong thermal X-ray emission in comparison to the RASS (using 0.017 counts s<sup>-1</sup> as RASS limit and Fig. 2.7 as described in Sec. 3.1). A more definite number of expected objects will be obtained in the near future by applying our population synthesis from Chapter 2 with implemented recent eROSITA effective area measurements.

In Sec. 3.3, we presented a method to utilize lower energies from the XMM-Newton EPIC-pn instrument for source detection. The noise is reduced significantly in the usually excluded energy range of 150 eV to 200 eV. However, there are still many noise patterns, especially e.g. on CCD 11. We could identify sources which are not detected in the standard energy range (200 eV to 12 keV, e.g. in the recently pre-released XMM SSC2), but seem to be reasonable detections by visual inspection. However, most of these sources are very faint and have to be confirmed in follow-up observations. Furthermore, there are still many noise detections and one has to be very careful with the sources provided by the automatic source detection. Considering our search for isolated neutron stars and the determined soft source list, it may be useful for future catalogue versions to additionally take into account energies higher than 1 keV in the source detection process. The comparison with the XMM SSC2 showed for some candidate sources a rise of the XMM SSC2 PN hardness ratios towards higher energies, which was unexpected from our one negative hardness ratio defined by the two bands [0.15, 0.5] keV and [0.5, 1.0] keV. While in principle the XMM SSC2 can provide the data at higher energies, it would be especially interesting for the soft sources, which are not known in the XMM SSC2, to have the spectral properties up to e.g. 4 keV in hand.

## Chapter 4

# Searching for substellar companions to neutron stars

(partially published, Posselt et al. 2005, IAUC200)

For a long time planets around neutron stars have not been expected due to the powerful supernova giving birth to the compact object. Astonishingly however, the first planetary mass companions ever discovered around other stars were neutron star companions. Four such objects are known around the old millisecond(ms)-pulsar PSR 1257+12 (Wolszczan & Frail, 1992, Konacki & Wolszczan, 2003, Wolszczan, 2005). They have up to four Earth masses and are very close to the primary – 0.2 AU to around 3 AU. Interestingly, for three of them nearly circular orbits are reported (Konacki & Wolszczan, 2003). Another planetary system around a neutron star is the binary system of the ms-pulsar PSR 1620+10 and its white dwarf companion (Sigurdsson et al., 2003, Sigurdsson & Thorsett, 2005). A 2.5 Jupiter mass object is orbiting the white dwarf at 23 AU and thus also the neutron star. Currently we do not know of any brown dwarf companion around a neutron star. Planetary mass and brown dwarf companions are usually referred to as substellar companions.

The unexpected discoveries raised several questions about the formation of these companions. Did they form before the supernova and how did they survive this event? If they formed after the supernova, how did they form? Have they been captured from other planet host stars? For PSR 1620+10 in the globular cluster M4, it is suspected that the white dwarf together with its companion replaced the original binary companion (Sigurdsson & Thorsett, 2005); however, this is extremely unlikely in the case of PSR 1257+12 because four planetary mass objects with nearly circular orbits are present. Apart from capturing there are several other models to explain planets around neutron stars either by assuming supernova survival or by planet formation after the supernova. We summarize these models shortly in the following and refer for a detailed description to

Podsiadlowski (1995) and references therein. If the planets around a neutron star survived the supernova, an initial orbital separation larger than 4 AU (to survive the giant stage) and asymmetric supernovae are needed. Eccentric orbits of the companions would be expected. The nearly circular orbits of its planets make this survival scenario unlikely for PSR 1257+12. For planet formation after the supernova, the supernova fallback model, the circumbinary disk model, and the disrupted companion model are currently discussed (e.g. Podsiadlowski 1995). In any case a proto-planetary disk is formed first, either from an evaporated or gravitationally destroyed companion, or from the bound supernova material. For PSR 1257+12 the circumbinary disk model and the disrupted companion model are currently favoured (Podsiadlowski, 1995). The disks of the different formation scenarios have different properties, e.g. masses, sizes and chemical compositions. The planet formation from these disks could differ from those around solar-like stars. Thus, the study of neutron star planetary systems in comparison to those around solar-like stars can be very fruitful for the understanding of planet formation in general.

But substellar companions of neutron stars are not only interesting for planet or brown dwarf formation theory. They could also provide insights into the supernova event and maybe the composition and final stages of the progenitor star(s). Studying low-mass companions around neutron stars, especially the companion masses and their orbital characteristics, can determine also the dynamical masses of the neutron stars applying Kepler's 3rd law. These masses, together with the star radii, constrain the equation of state of matter in the neutron stars. Currently no radius and mass of a neutron star are known precisely for the same object and the equation of state of ultradense matter in the universe is one of the big questions in astrophysics. Whereas masses of neutron stars can be derived for binary systems (e.g. Jonker et al. 2003), the best radius estimation comes from the radio-quiet X-ray thermal neutron stars, which are isolated without stellar companions (e.g. Trümper et al. 2004).

We present here the first steps of our project to find new substellar companions around neutron stars including the especially interesting radio-quiet X-ray thermal neutron stars. In Section 4.1 the method and source selection are described. Section 4.2 gives some details about observations and data reduction, while in Section 4.3 the first results are presented.

## 4.1 Methods and sample selection

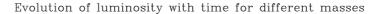
## 4.1.1 First epoch observations

The two planetary systems around the ms-pulsars have both been found by the radio pulse timing technique, which measures variations in the pulse arrival times. This technique is

most sensitive to very stable ms-pulsars and requires much observing time. For ordinary radio pulsars the timing noise hinders the accurate measurements needed. Radio-quiet neutron stars are not covered. The radio pulse timing technique can detect only relatively close companions like in radial velocity planet searches among normal solar-like stars. Therefore, wide substellar companions cannot be detected with this method. As neutron stars are very faint (fainter than 25 mag in the optical), the commonly used radial velocity method or the search for astrometric wobbling should preferably be done in X-rays where neutron stars are bright. Unfortunately the spectral and spatial resolution in X-ray astronomy is currently not good enough for these methods. Furthermore, companions are expected to be larger than the primary, which rules out the transit method.

Substellar companions of all possible separations can be detected only by direct imaging, primarilly in the near infrared (NIR)<sup>1</sup> if the companions are young. They are several magnitudes fainter in the optical. The companions are brighter than the neutron stars in the NIR, even though lower in mass, because they are larger in size and still contracting when young. Direct detection of very close (even few AU) and faint substellar companions is currently possible only around neutron stars. Wide faint substellar companions can be detected too. However, we are restricted to young objects at small distances from the sun. The magnitudes of substellar objects (brown dwarfs and giant planets) with at least few up to tens of Myrs age can be predicted following the non-gray theory of substellar objects by Burrows et al. (1997), who have computed IR magnitudes of substellar objects depending on age and mass. At an age of 100 Myrs and a distance of 300 pc, a companion at the Deuterium burning mass limit ( $\sim 13 \, \mathrm{M_{jup}}$ ) would have an H-band magnitude of 22 mag (Burrows et al. (1997), see also Fig. 4.1).

<sup>&</sup>lt;sup>1</sup>usually the J, H, K bands are meant by near infrared



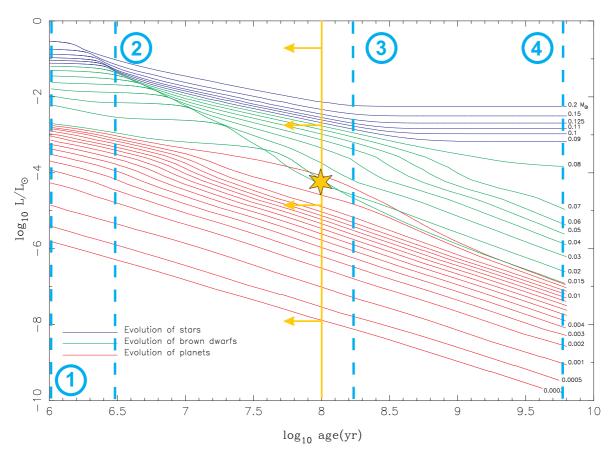


Figure 4.1: Expected *H*-band luminosities of substellar companions

This draft is based on Fig. 7 by Burrows et al. (1997) and shows the calculated bolometric luminosity L versus age for low mass objects. By the use of the luminosity-magnitude relation with a bolometric correction one can derive the expected H-band magnitude. Our initial selection criterion of younger than 100 Myrs is indicated by the yellow line, a 100 Myrs old object at the Deuterium burning mass limit and at a distance of 300 pc is represented by the yellow star corresponding to an H-band magnitude of 22 mag. The updated assumed ages of some exemplary neutron stars of our sample (see individual descriptions in the text) are shown by the cyan lines and numbers: 1 - RX J1856.6-3754 and the other XTINSs; 2 - PSR J1932+1059; 3 - PSR J0108-1431; and 4 - PSR J2124-3358.

If substellar companions to the neutron stars formed before the supernova, their age is the sum of the age of the progenitor star and the time elapsed since the neutron star was born in the supernova. The former is negligible compared to the latter for most of the known neutron stars, especially if no supernova remnant is present. Therefore, all neutron stars younger than 100 Myrs and closer than 300 pc were chosen as the initial

sample by R. Neuhäuser in 2000 for the first NIR-observations. Within 300 pc seven radio pulsars have been selected from the pulsar catalog of Taylor et al. (1993). They were thought to be ordinary radio pulsars, thus still young as radio emission from non-recycled neutron stars is expected to last only at most 10 Myrs (Lorimer & Kramer, 2004). To that sample, the seven radio-quiet X-ray thermal neutron stars have been added. As noted above these neutron stars are especially interesting to constrain the equation of state due to their blackbody-like spectra resulting in the best radius estimation currently available (Trümper et al., 2004). They also represent nearly half of the local young neutron star population (for reviews, see e.g. Neuhäuser & Trümper (1999), and Haberl (2004) and also Introduction and Sec. 3). No co-moving companions down to substellar masses have been identified in deep optical observations. All stellar companions would have been detected.

The ages of the radio pulsars in our sample are known roughly from the characteristic spin-down age. Assuming magneto-dipole braking the characteristic age  $\tau$  is estimated by  $\tau = P/(2\dot{P})$ , where P is the measured period and  $\dot{P}$  the measured period derivative of the neutron star. However, radio pulsars are multipoles rather than pure dipoles. Therefore, the characteristic age is only a very coarse estimation of the true neutron star age. For the well known Crab pulsar the spin-down age exceeds the true age by about 25%. Initally assumed to be younger than 100 Myrs, some of our selected radio pulsars seem to be older from newer data, so that possible substellar companions would be fainter (see individual discussion in Section 4.3). The additional radio-quiet neutron stars found as soft ROSAT sources are most probably also young neutron stars, indicated by large proper motion together with their likely origin, and high magnetic fields. They are probably several Myrs old, with cooling surfaces which emit the X-ray emission. For all seven radio-quiet X-ray thermal neutron stars, it appears unlikely that they are old with their X-ray emission due to accretion from the interstellar medium. First, they have constant X-ray emission over years with one notable exception where precession is likely (Haberl et al., 2006). Neuhäuser & Trümper (1999) quoted also statistical reasons for excluding accretion from the ISM. Furthermore, three radio-quiet X-ray thermal neutron stars have known proper motions, which are so high that they imply too low Bondi-Hoyle accretion efficiencies to describe these stars as old neutron stars re-heated by accretion from the ISM. The dependence of the expected bolometric luminosity from the age, is shown in Fig. 4.1 which is based on Burrows et al. (1997). The infrared magnitudes resulting from these expected luminosities are noted individually for each object in Section 4.3.

Most of the 14 neutron stars are at relatively high galactic latitudes, and for all fields we know that the absorbing column densities are quite low. For the radio pulsars, rough distance estimates are available from the dispersion measure, which indicates the electron

column density towards the pulsar (Taylor et al., 1993, Manchester et al., 2005). For the radio-quiet X-ray thermal neutron stars, the determination of a parallax is available only in one case, namely RX J1856.5-3754 for which Walter & Lattimer (2002) determined a distance of  $\sim 117$  pc with the HST. Recently van Kerkwijk & Kaplan (2006) reported an improved distance estimation with RX J1856.5-3754 being at  $161^{+18}_{-14}$  pc. The other X-ray thermal neutron stars appear to be very similar. The measured column densities from the X-ray spectra are smaller than the galactic values (towards the respective direction of sight), which means that these neutron stars are also quite nearby. One can assume the same order of magnitude for the distance as for RX J1856.5-3754, i.e. roughly 100 to 300 pc. Taking into account absorption by the inhomogenously distributed interstellar medium, the estimated distances for three XTINS support this assumption (see Sec. 2.3.2).

Given the age and distance d of the neutron star the expected H-band magnitude to find brown dwarfs and massive gas planets can be calculated using the luminosity ratio  $L \cdot L_{\odot}^{-1}$  of the companions, where  $L_{\odot}$  is the bolometric luminosity of the sun.  $L \cdot L_{\odot}^{-1}$  depends on the companion mass, following Burrows et al. (1997) and the luminosity magnitude relation:

$$m_H = BC + 5 \log d [pc] - 0.26 - 2.5 \log \frac{L}{L_{\odot}}.$$
 (4.1)

The bolometric correction (BC) varies only little for L and T dwarfs. BC<sub>K</sub>, the bolometric correction in the K-band for example, has a reported range from  $\approx 1.5$  to  $\approx 3.5$  (Golimowski et al., 2004, Leggett et al., 2002). BC<sub>H</sub> for the neighbouring H-band is assumed to be roughly the same as for the K-band. We use a BC=BC<sub>H</sub>  $\approx$ B<sub>K</sub> of 3.46 for a L3.5 dwarf (Golimowski et al., 2004).

In the following, orbital separations of up to 5000 AU are inspected for objects fainter than the magnitude obtained by equation 4.1 at the brown dwarf mass limit. The wide separations take into account recently found wide substellar companions at roughly 4000 AU around main sequence stars and possible widening of orbits due to the mass loss of the primary during the supernova. The faint sources found are then cross-correlated to sources in available optical observations obtaining optical-NIR-colors. This is usually done with the help of archival or kindly provided optical observations. Many first-epoch-objects can be rejected as possible substellar companion candidates due to these colors being typical for normal stars according to Kenyon & Hartmann (1995). The given optical and optical-NIR-colors by Kenyon & Hartmann (1995) go down to spectral type M6. As an example, one would expect the R-H color to be lower than 5 mag for normal stars down to M6 V, while L and T dwarfs usually have higher values of around 6 mag. This can be seen in Fig. 1 of Kirkpatrick et al. (1999) shown for the R-K color (the H-K colors are around

0.6 mag for most L and T dwarfs, see e.g. Fig. 14 of Kirkpatrick et al. 1999). However, we can not exclude ultra-cool M-dwarfs (M8) at this stage. We note the use of a conventional magnitude error of usually 1 mag up to exceptionally 2 mag for the optical-NIR-colors considering variations in the magnitudes of the reference optical observations as well as errors in the magnitude estimation of the NIR-objects. By this, all potentially interesting sources should be included.

At the positions of the neutron stars we check also for faint NIR-objects which could be unexpected possible counterparts of the neutron stars themselves. We determine an upper limit for the IR counterpart of the neutron star in cases of no such objects within the positional errors.

#### 4.1.2 Second epoch observation

By the known proper motions of the neutron stars it is possible to calculate the expected shifts in pixel coordinates. First and second epoch observations are compared regarding object detections, magnitudes and position errors. Due to the chosen time span it should be possible to distinguish clearly the expected shifts for co-moving objects from position errors. However, because of scheduling at another telescope and instrument, additional errors have to be considered, discussed in Sec. 4.3.2. We check whether we reach deeper NIR-limits at the position of the neutron stars by combining first and second epoch observations.

#### 4.2 Observations and data reduction

### 4.2.1 First epoch observations

The first observations of five interesting southern neutron star fields were obtained by R. Neuhäuser with the European Southern Observatory's (ESO's) New Technology Telescope (NTT) equipped with SOFI in H-band (1.65  $\mu$ m) in December 2000 (66.D-0135). These observations have been reduced using ESO's Eclipse (version 4.8.1). However, comparing to the Very Large Telescope (VLT) ISAAC observations obtained later, the SOFI ones are generally less deep and suffer from worse seeing conditions. As it turned out the faintest objects were the most interesting ones, so we analyse and discuss only the VLT ISAAC observations in the following.

Of the 14 selected young nearby neutron stars, twelve were observed in H or K-band using the VLT (ISAAC), the Keck telescope (NIRSPEC) or the 2.2 m telescope of the University of Hawaii (QUIRC, deep imaging). We neglect here the analysis and discussion

of the Keck and 2.2 m observations as they have been analysed and presented by Andreas Schmidt in the frame of his bachelor thesis (Schmidt, 2004).

The first epoch observations for eight southern neutron stars were obtained in 2003/4 (P71, P72) and one in 2005 (P74) in the *H*-band with *ISAAC* mounted on UT1 of ESO's VLT in service mode. We concentrate here on these data in the following. For more information on the telescope and instrument see Appendix A.2.1. The VLT observation times ranged from two to three hours. The seeing was usually better than 0.8" and the airmass in most cases below 1.5 (for comparison, the airmass at zenith is defined to be 1). The *jitter*-Mode was used with individual exposures of 12 sec and a jitter box width of 20".

The data have been reduced with ESO's *Eclipse* (version 4.8.1 and 5.0.) (Devillard, 1999, 2001). Individual images with poor seeing or high airmass have been excluded. Multiple observations of the same object have been reduced individually. The results have then been combined using IRAF (Tody, 1986, 1993) if observing conditions were similar. We obtained the astrometry for the first epoch observation with the 2MASS point source catalogue  $(PSC)^1$  using GAIA (Draper et al., Starlink project). GAIA was also applied for object detection provided that a signal-to-noise ratio (SNR) of at least three is reached. GAIA makes use of the Source Extractor by Bertin & Arnouts (1996). In this program one can choose several detection parameters like the used filters (e.g. gaussian), or how to handle overlapping sources. We tested several sets of parameters and applied individually the apparently best suited one for each observational field. We then estimated the H-band magnitude by calibrating with the (preferably faint) 2MASS PSC sources. The achieved SNR for a 22 mag object is around three (for details see Section 4.3), magnitude errors are around 0.4 mag. We checked the positional accuracy reached by 2D-Gaussfits using IDL. For the interesting – usually faint – objects, three times the mean positional uncertainty is  $3\sigma \approx 80$  mas, but can also reach exceptionally 230 mas for the faintest. The pixel scale of ISAAC is  $\approx 147$  mas. Brighter objects have usually better determined positions.

### 4.2.2 Second epoch observations

Second epoch observations will be or have already been proposed depending on the positional accuracies reached in the first epoch observations and the known proper motions. In May 2006, we did the second epoch observations for two objects: RX J1856.6-3754 and PSR J1932+1059. Both have large proper motions. Unfortunately, ESO moved the run to the alternative instrument SOFI at the NTT (more on the telescope and instrument,

 $<sup>^{1}</sup>$ see Appendix A.3 for more information on 2MASS

see Appendix A.2.2). Although SOFI is, in principle, very similar to ISAAC the use of a different instrument at the second epoch causes additional positional errors which have to be taken into account. Additionally, the seeing conditions on La Silla were worse than on Paranal for the northern target PSR J1932+1059.

The two fields were observed for around three to four hours during each of the four nights. The seeing was usually better than 1", and during the second and third night most of the time even better than 0.8", and in the last night very variable. The airmass of RX J1856.6-3754 was usually below 1.5, while for PSR J1932+1059 the airmass was only below 2.0 for most of the observations. The *jitter*-mode was used with a jitter box width of 20" and individual exposures of 15 sec and 12 sec for RX J1856.6-3754 and PSR J1932+1059, respectively. The observations have been reduced by applying the SOFIpipeline procedures at the telescope. They have been written by the instrument scientist of SOFI, V. Ivanov (ESO). We cross-checked the result by reducing individual runs also with Eclipse. The following data reduction procedure was the same as for the first epoch observations applying IRAF, GAIA and IDL. The second epoch SOFI observations are up to 1 mag less deep than the ISAAC observations. Only objects detected with a SNR of at least three in both - ISAAC and SOFI observations - are considered for the search for co-moving objects. We derive the positional shifts for a large number of objects being present in both observations. By this, we find a systematic shift in the pixel scale, which is different for the two used instruments. We consider this effect by a linear fit of the ISAAC pixel scale to derive the SOFI pixel scale (see Sec. 4.3.2). This implies an additional error for the found positional shifts.

#### 4.3 First results

#### 4.3.1 First epoch observations

Table 4.1: Results of the first epoch ISAAC H-band measurements for ten neutron stars Listed are for each object: the month of the observation, the distance D, the proper motion in Right ascension  $(\mu_{\alpha})$  and Declination  $(\mu_{\delta})$  if known (n.k. stands for not known).  $H_{lim}$  indicates the faintest H-magnitude with a detection SNR of three, which one could measure at the position of the neutron star. The error of  $H_{lim}$  is around 0.4 mag.  $N_{Obj}$  is the number of interesting objects for a second epoch observation found within 5000 A.U. around the neutron star at the given distance.

| Object                      | Obs. Date      | $H_{lim}$      | D                              | $\mu_{\alpha}$               | $\mu_{\delta}$               | $N_{Obj}$ |
|-----------------------------|----------------|----------------|--------------------------------|------------------------------|------------------------------|-----------|
|                             |                | [mag]          | [pc]                           | $[\text{mas yr}^{-1}]$       | $[\text{mas yr}^{-1}]$       |           |
|                             |                |                |                                |                              |                              |           |
| PSR J0108-1431              | Jun 2003       | 21.5           | $130^{1}$                      | $< 26^{1}$                   | $< 78^{1}$                   | 0         |
| RX J0420.0-5022             | Jan 2004       | 21.5           | $300^{\mathrm{ass}}$           | $< 138^2$                    | $< 138^2$                    | 2         |
| Geminga                     | Dec 03/ Jan 04 | 22.0           | $157^{+59}_{-34}$ <sup>3</sup> | $138 \pm 4^{3}$              | $-97 \pm 4^{3}$              | 33        |
| RX J0720.4-3125             | Jan 2004       | 22.3           | $240^{\mathrm{ass}}$           | $-47 \pm 16^{4}$             | $85 \pm 16^{4}$              | 5         |
| RX J0806.4-4123             | Dec 2004       | 22.3           | $255^{\mathrm{ass}}$           | $< 76^{2}$                   | $< 76^{2}$                   | 45        |
| RX J1856.6-3754             | May 2003       | 22.1           | $117\pm12$ $^{5}$              | $326.7 \pm 0.8$ <sup>5</sup> | $-59.1 \pm 0.7$ <sup>5</sup> | 58        |
| PSR J1932+1059              | Jun 2003       | 18.5           | $361^{+10}_{-8}$               | $94.03 \pm 0.14^6$           | $43.37 \pm 0.29^6$           | 10        |
| PSR J2124-3358              | May/Jun 2003   | 22.0           | $270 \pm 20^{7}$               | $-14 \pm 1^{8}$              | $-47\pm1^{8}$                | 0         |
| RBS 1774 <sup>a</sup>       | Jun 2003       | $21.7^{\rm p}$ | $300^{\mathrm{ass}}$           | n.k.                         | n.k.                         | 5         |
| PSR J2144-3939 <sup>s</sup> | Jul 2003       | 22.2           | n.k.                           | n.k.                         | n.k.                         | s         |

<sup>&</sup>lt;sup>a</sup> RXS J214303.7+065419

PSR J0108-1431 is one of the closest radio pulsars according to its very low dispersion measure  $(2.38\pm0.01~{\rm cm^{-2}}, {\rm D'Amico}~{\rm et}~{\rm al.}~1998)$ . The faint pulsar has a distance of 130 pc and seems to be older (170 Myrs, Mignani et al. 2003) than we assumed initally. This is probably due to refined measurements of the period and period derivative. No X-ray detection is reported for this object. The proper motion is below 82 mas/yr (Mignani et al., 2003). Possible brown dwarfs around PSR J0108-1431 should have H-band magnitudes fainter than 20.8 mag (see equation 4.1 and used bolometric correction), and

<sup>&</sup>lt;sup>1</sup> Mignani et al. (2003), <sup>2</sup> Motch et al. (2006), <sup>3</sup> Caraveo et al. (1996, 1998), <sup>4</sup> Motch et al. (2003), <sup>5</sup> Walter & Lattimer (2002), <sup>6</sup> Chatterjee et al. (2004), <sup>7</sup> Gaensler et al. (2002), <sup>8</sup> Toscano et al. (1999)

s suspicous source, mentioned once by Taylor et al. (1993) and Manchester et al. (1996), but no new parameters in recent catalogues, see individual discussion

<sup>°</sup> old neutron star, see individual discussion

ass assumed distance as estimated from X-ray measured hydrogen column density

<sup>&</sup>lt;sup>p</sup> a source with this magnitude is present within the positional uncertainty of the neutron star, see individual discussion

planets should be fainter than 25.0 mag. There are only two relatively bright 2MASS point sources in the observed field. They are used for astrometry and zeropoint determination. The obtained photometric magnitudes for the objects of interest have large error bars due to the availability of only two bright 2MASS sources for the zeropoint determination. Astrometric positions have been refined using USNO B1 point source positions. Within 5000 AU there is only one source fainter than H=20.8~mag having H=21.0mag. We obtained the archival VLT FORS1 images in the V-band, reduced the data applying bias subtraction and flat fielding and calibrated the source V-band magnitudes with the tabulated values of Mignani et al. (2003). The faint NIR-object is detected in the V-band with 25.6 mag. Therefore, the V-H-color is 4.6 mag. This color is typical for spectral type M2 V or M3 V according to Kenyon & Hartmann (1995). Even when taking an error of 1 mag into account the source is a bad candidate for a substellar companion around PSR J0108-1431. Thus, there are no substellar companion candidates for second epoch observations from our VLT ISAAC image within 5000 AU around PSR J0108-1431.

At a SNR of three magnitudes of H=21.5 mag are reached for detected NIR-sources. However, magnitudes are uncertain to approximately 1.5 mag due to only two present 2MASS sources for zeropoint determination. There is no source at the position of the neutron star within 1".

RX J0420.0-5022 is one of the X-ray thermal isolated neutron stars. Neither its distance nor its proper motion have been measured. The hydrogen column density fitted in the X-ray spectrum indicates a distance of roughly 300 pc. Assuming a similar age as that of the better known XTINSs like RX J0720.4-3125 and RX J1856.6-3754 one would expect substellar companions having H-band magnitudes larger than 19.04 mag at this distance. Planets would be fainter than 22.8 mag. Only two objects are present within 5000 AU around the neutron star position for a distance of 300 pc. They are brighter than possible planetary companion candidates. There are optical archival observations with ESO's VLT equipped with FORS1 (66.D-0128). The three B-band observations have been added and the photometry was calibrated with the USNO B1 catalogue. The scatter of the obtained zeropoint was quite large. The difference between USNO B1 (B2mag) and the roughly calibrated FORS1 B-band image could reach 2 mag. At the position of the two interesting sources there are no optical sources down to the  $\approx 26$  mag limit of the FORS1 B-band observations. Thus, the NIR-sources could not be excluded as possible substellar companions by their B-H color. Only the second epoch observation, as soon as the proper motion is constrained, can clarify possible companionship.

At a detection SNR of three magnitudes, a H = 21.9 mag object is found to be the faintest source. Near the position of the neutron star objects are detected with 21.5 mag. There are only few 2MASS PSC objects within the field of view, only three being fainter

than 15 mag. Photometry obtained by calibrating with these 2MASS PSC objects is less reliable than if it could have been done with fainter objects. The magnitude error in this field is therefore suspected to be around 0.6 mag instead of the 0.4 mag obtained by combining the errors of the 2MASS calibration and the object photometry. The upper limit for the undetected neutron star in the H-band is therefore  $21.5 \pm 0.6$  mag.

Geminga is one of the rare  $\gamma$ -ray pulsars, also detected in X-rays and at optical wavelengths. The distance of Geminga is still under discussion. Faherty (2006), Walter (2006) reported a newly estimated parallactic distance of  $254^{+111}_{-59}$  pc. However, this is still in agreement with the here adopted value of  $157^{+59}_{-34}$  pc by Caraveo et al. (1996, 1998). Therefore, possible substellar companions around Geminga should have H-band magnitudes fainter than 17.6 mag, and planets fainter than 20.5 mag. There are 86 interesting sources within 5000 AU down to 21.9 mag with a minimal SNR of three. From the ESO-archive we retrieved NTT SUSI1 observations of a part of the field. We obtain V-band magnitudes down to a limit of only 24.5 mag with relatively large errors. For the unobserved part of the field we use the USNO B1 catalogue and its limit of B=21 mag. The derived V-H or B-H colors reject many of the objects. We end up with a list of 33 interesting objects.

An H-magnitude of  $22.0 \pm 0.4$  mag has been found to correspond to a detection SNR of three. There are several clearly detected objects at this limit in the image, also in the field close around the neutron star. As there is no NIR-object at the position of the neutron star an upper limit of 22.0 mag applies for an H-band magnitude of Geminga.

RX J0720.4-3125 is the second brightest of the X-ray thermal neutron stars and recently a precession with a period of roughly seven years has been reported (e.g. Haberl et al. 2006). The exact distance is unknown. The hydrogen column density fitted in the X-ray spectrum indicates a distance of 240 to 270 pc taking into account the local imhomgenously distributed ISM (see Sec. 2.3.2). At a distance of 240 pc possible substellar companions around this neutron star should have H-band magnitudes fainter than 18.6 mag, planets would have H-band magnitudes fainter than 21.9 mag. We find around 50 interesting sources within 5000 AU down to 22.3 mag with a minimal SNR of three. C. Motch kindly provided us with his deep VLT FORS1 observations of 2001 and 2003 (Motch et al., 2003). For most of the objects we can obtain the B-H color, for non-detected NIR-objects only lower limits (taken FORS1 limit of B=28 mag). Within 5000 AU the final list consists of five interesting objects having all H-band magnitudes fainter than 20.9 mag. At a detection limit of  $2\sigma$  one more object appears which seems to be real by visual inspection.

An H-magnitude of  $22.6 \pm 0.4$  mag has been found to correspond to a detection SNR of three. However, (non-)detections at this level are sometimes suspious. In the field close

around the neutron star a safe limit seems to be 22.3 mag comparable to the faintest detection. The magnitude error is around 0.4 mag for such faint objects. At the position of the neutron star there is no NIR object down to 22.3 mag.

RX J0806.4-4123 is one of the faintest of the seven X-ray thermal neutron stars. Neither the proper motion nor the distance have been measured due to a still missing optical counterpart. The hydrogen column density fitted in the X-ray spectrum indicates a distance of  $240 \pm 25$  pc taking into account the local imhomgenously distributed ISM (see Sec. 2.3.2). Possible substellar companions around RX J0806.4-4123 should have H-band magnitudes fainter than 18.6 mag, planets would be expected to have H-band magnitudes fainter than 21.9 mag at this distance. We find around 50 interesting NIR-sources within 5000 AU down to H = 22.0 mag having a minimal SNR of three. We observed the very crowded field in the V-band using ESO's NTT equipped with SUSI in December 2004. The data have been reduced applying dark field subtraction and flat fielding. Bias subtraction was negelected. Astrometry of the optical observation has been obtained by fitting with the USNO B1 point source positions. The photometry was obtained by a standard field observation reduced in the same way. The derived limit for  $3\sigma$  detections is V=24.8 mag. A few NIR-sources could be excluded as possible substellar companions due to their low V-H-color. However, most of the interesting objects are not detected in the V-band. All the final 45 objects will have to be investigated in the second-epoch observation as soon as the proper motion of this neutron star is known.

There are NIR-objects detected down to a H-magnitude of  $22.6 \pm 0.4$  mag at a SNR of three. In the field close around the neutron star a safe lower limit seems to be 22.3 mag representing the faintest detection there. The magnitude error is around 0.4 mag. At the position of the neutron star there is no NIR-object down to 22.3 mag.

RX J1856.6-3754 is the brightest of the X-ray thermal neutron stars and especially remarkabe because of its featureless spectrum and one of the best NS radius estimations (e.g. Trümper 2005, Burwitz et al. 2003). The HST-determined parallax and thus the distance is still under discussion and refining. While Kaplan et al. (2002b) reported  $142^{+58}_{-39}$  pc we use here a distance of  $117 \pm 12$  pc as determined by Walter & Lattimer (2002) being still in correspondence with the former within error bars. We note the very recently reported distance of  $161^{+18}_{-14}$  pc by van Kerkwijk & Kaplan (2006). The age of RX J1856.6-3754 is assumed to be around 1 Myr given the proper motion and the birth place in Upp Sco (Neuhäuser, 2001). Following Burrows et al. (1997) possible substellar companions around this very close neutron star should have H-band magnitudes fainter than 16.5 mag. Planets would be expected to be fainter than 20.6 mag. There are 201 sources of interest within 5000 AU down to 22.1 mag having at least a detection SNR of three. For many of these objects we can obtain the B - H and/or V - H color using

avaiable deep VLT FORS1 observations by Neuhäuser (2001), HST observations (Walter & Matthews, 1997, Walter, 2001) with  $F_{606} \approx V$  and tabulated values (e.g. Neuhäuser et al. 1997).

The limiting magnitudes are taken as B=24.6 mag, and V=26.4 mag, both given by the faintest detected objects in the B- or V-band observations. These limits are applied for non-detected NIR objects if these sources have positions in the field of the optical observations. The field of the deep V band observations is particularly small and does not cover the whole interesting area of 5000 AU around the neutron star. Many objects can be rejected as possible substellar companion candidates due to their colors being typical for normal stars according to Kenyon & Hartmann (1995). Seven interesting objects have at least one detection in B- or V-band, the derived colors are not typical for stars up to M6. However, there are 51 NIR objects not detected in B or V. They will be also considered in the second epoch observation.

We end up with a list of 58 sources, seven of them being especially interesting due to their optical-NIR-colors.

An H-magnitude of  $22.1 \pm 0.4$  mag has been found to correspond to a detection SNR of three in the field close around the neutron star. At the position of the neutron star there is no NIR object down to 22.1 mag.

PSR J1932+1059 is a radio pulsar. New VLBI measurements put this neutron star at a distance of  $361 \pm 10$  pc (Chatterjee et al., 2004), further away than previously thought. Therefore, only brown dwarfs could be detected as possible substellar companions given its spin down age of  $3.1 \cdot 10^6$  years (Hobbs et al., 2004), and following the models by Burrows et al. (1997). Planet candidates would be fainter than H=23.5 mag. PSR J1932+1059 lies unfortunately in a crowded field with a very bright source (H=8.8 mag) causing source confusion and large photometric errors in the immediate vicinity. There are about 20 sources of interest within 5000 AU around PSR J1932+1059 having at least a SNR of three. R. Mignani (ESO/MSSL UK) kindly provided us with his deep VLT FORS1 observations from 1999 which cover the whole field of interest. For many of the objects we can obtain the R-H color, for optically non-detected NIR-objects lower limits (taken FORS1 limit of R=25 mag) are used. We end up with a list of 10 interesting objects within 5000 AU having all H-band magnitudes fainter than 19.5 mag, the brightest magnitude possible for brown dwarf companions.

At the position of the neutron star there is strong contamination from the nearby ( $\approx 2.5''$ ), bright H=8.8 mag source. There are many objects with the same spatial distance from the bright object towards other directions. None of them are fainter then H=18.5 mag, but some are not easy to distinguish from the background. Therefore, the limit for the non-detection of the neutron star is not better than 18.5 mag. The

magnitude error, however, is suspected to be around 1 mag due to the contamination.

**PSR J2124-3358** is a millisecond radio pulsar. The up-to-date ATNF pulsar catalogue (Manchester et al., 2005) indicates an age of  $5.86 \cdot 10^9$  years which is considerably longer than we thought when selecting this source some years ago from Taylor et al. (1993) in its latest online version. At this age and a distance of 270 pc, cooling substellar companions would have magnitudes fainter than H = 24.9 mag following Burrows et al. (1997). Our  $ISAAC\ H$ -band observations are not deep enough to detect such objects.

For  $3\sigma$  detections the limit is H=22.0 mag. The magnitude error is around 0.6 mag due to only few 2MASS point sources within the observed field used for zero point determination. There is no object detected within 1" around the position of the neutron star.

RXS J214303.7+065419 is the X-ray thermal isolated neutron star found last. We do not know of an optical counterpart down to B=26 mag (Komarova, 2006). The most recent X-ray position by XMM has an uncertainty radius of 3" (Zane et al., 2005). Interestingly, Malofeev et al. (2006) reported a (weak) radio detection which has still to be confirmed. A distance of 300 pc is assumed, motivated by the absorption in the X-ray spectra. Assuming an age similar to that of the better known XTINSs like RX J0720.4-3125 and RX J1856.6-3754 one would expect substellar companions having H-band magnitudes larger than 19.04 mag at this distance. Planets would be fainter than 22.8 mag. There are nine interesting objects within 5000 AU around the neutron star position. The needed magnitudes for planets are not reached. Due to the availability of only three relatively bright and clustered 2MASS point sources the photometric error of the sources is around 1 mag, especially for faint objects. The 2MASS obtained astrometry was improved by using additional USNO B1 point source positions.

The archival ESO EMMI R-band observations by Zampieri et al. (2001) have a limit of R=23 mag. EMMI detected objects, some also present as USNO B1 point sources, provide the R-H color for the NIR-sources. For five NIR-sources only the limit of R=23 mag could be applied and thus no statement of a color in favour for substellar companionship is possible. The four sources with a known R-band magnitude can be excluded as possible substellar companions due to their R-H color even considering a color magnitude error of 2 mag. Two of the sources are elongated and are probably galaxies. Whether the remaining three sources are co-moving objects can only be constrained with the knowledge of the still unknown proper motion.

There are sources down to H=21.6 mag at  $3\sigma$  close to the neutron star position. Within the r=3'' uncertainty circle one can identify a faint source by eye. This source can be detected above  $2\sigma$  with H=21.7 mag. As mentioned above the magnitude error is around 1 mag.

PSR J2144-3939 was selected by us from the pulsar catalogue of Taylor et al. (1993) in its latest online version. Only the period was given there, not the period derivative (no characteristic age determination possible). There are no new publications investigating this pulsar and the up-to-date ATNF pulsar catalogue (Manchester et al., 2005) does not know this radio pulsar at all while in an old version (Manchester et al., 1996) it was present. It seems likely that the detection by Taylor et al. (1993) could not be confirmed and the source was rejected. Therefore, as well as for missing parameters like age and proper motion it is not reasonable anymore to search for substellar companions around this source.

Nevertheless we present here the limit at the suspected neutron star position. Sources are detected at  $3\sigma$  up to H = 22.2 mag. Due to only five relatively bright 2MASS point sources the maximal expected magnitude error is 1 mag. There is no NIR source within 1" of the pulsar position reported by Manchester et al. (1996).

Table 4.2: Coordinates and box sizes used in Fig. 4.2 and 4.3
Given are the position of the neutron stars with reference and the epoch applied to

consider proper motions if known. If the proper motions are not known or only as upper limits, this is indicated by " $\cdots$ " (see also Table 4.1). Furthermore, the box sizes of the images shown in Fig. 4.2 and 4.3 are given.

| Object                      | RA           | DEC          | REF | epoch  | $\triangle \alpha_{box}$ | $\triangle \delta_{box}$ |
|-----------------------------|--------------|--------------|-----|--------|--------------------------|--------------------------|
|                             | hh:mm:ss     | dd:mm:ss     |     |        | ["]                      | ["]                      |
| PSR J0108-1431              | 01:08:08.317 | -14:31:49.35 | 1   |        | 26.9                     | 18.1                     |
| RX J0420.0-5022             | 04:20:01.950 | -50:22:48.10 | 2   |        | 22.5                     | 15.3                     |
| Geminga                     | 06:33:54.237 | +17:46:13.73 | 3   | 2003.9 | 35.5                     | 29.0                     |
| RX J0720.4-3125             | 07:20:24.924 | -31:25:50.90 | 4   | 2004.0 | 29.0                     | 26.7                     |
| RX J0806.4-4123             | 08:06:23.400 | -41:22:30.90 | 2   |        | 24.6                     | 18.1                     |
| RX J1856.6-3754             | 18:56:35.714 | -37:54:36.44 | 5   | 2003.4 | 22.5                     | 15.3                     |
| PSR J1932+1059              | 19:32:13.950 | +10.59:32.42 | 6   | 2003.5 | 22.6                     | 15.3                     |
| PSR J2124-3358              | 21:24:43.855 | -33:58:44.61 | 7   | 2003.5 | 41.7                     | 30.3                     |
| RBS 1774 <sup>a</sup>       | 21:43:03.300 | +06:54:17.00 | 8   |        | 25.1                     | 17.0                     |
| PSR J2144-3939 <sup>s</sup> | 21:44:12.000 | -39:39:00    | 9   |        | 22.5                     | 15.2                     |

<sup>1:</sup> Mignani et al. (2003), 2: Haberl et al. (2004a) *Chandra* positional uncertainty is 0.6", 3: Caraveo et al. (1998), 4: Kulkarni & van Kerkwijk (1998), 5: Kaplan et al. (2002b), 6: Chatterjee et al. (2004), 7: Gaensler et al. (2002), 8: Zane et al. (2005), 9: Taylor et al. (1993)

s suspicous source, mentioned once by Manchester et al. (1996) but no new parameters in other articles, see individual discussion

<sup>&</sup>lt;sup>a</sup> RXS J214303.7+065419

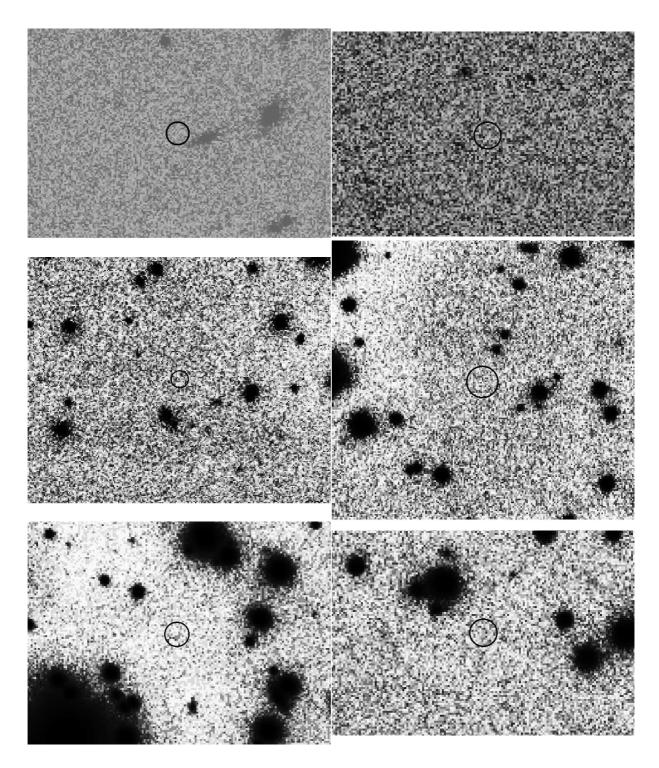


Figure 4.2: **Neutron star detection limits in the H-band (1)** Moving left to right, top to bottom the H-band fields of the following neutron stars are shown: PSR J0108-1431, RX J0420.0-5022, Geminga, RX J0720.4-3125, RX J0806.4-4123, and RX J1856.6-3754. North is up, east is to the left. Each circle has a radius of 1". The used neutron star coordinates as well as the box sizes can be found in Table 4.2. The values of the *H*-band limit are listed in Table 4.1.

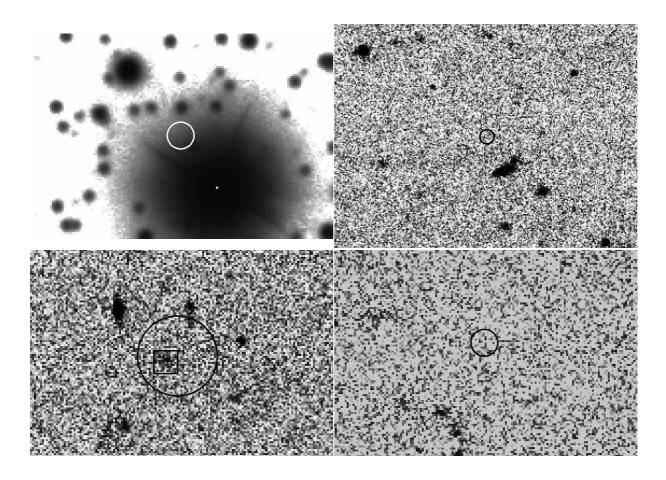


Figure 4.3: Neutron star detection limits in the H-band (2) Moving left to right, top to bottom the H-band fields of the following neutron stars are shown: PSR J1932+1059, PSR J2124-3358, RXS J214303.7+065419 and PSR J2144-3939. North is up, east is to the left. With the exception of the RXS J214303.7+065419-field each circle has a radius of 1". In case of RXS J214303.7+065419 the circle has a radius of 3" due to the very uncertain position of the neutron star. The small box in this neutron star's positional error circle marks a faint source visible by eye ( $2\sigma$  detection); see individual discussions. The applied neutron star coordinates as well as the box sizes can be found in Table 4.2. The values of the H-band limit are listed in Table 4.1.

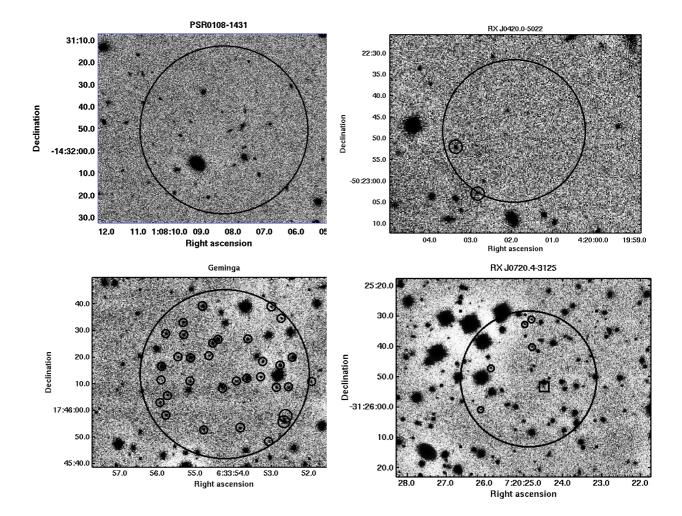


Figure 4.4: Interesting NIR-objects around the neutron stars (1) Each big circle has a radius of 5000 AU at the distance of the neutron star. The small circles highlight the final object list to be considered for the second epoch observation of each neutron star. These faint objects have at least a detection SNR of three. In the case of RX J0720.4-3125 an additional probably real  $2\sigma$  detection is indicated by the box. Faint objects being present within 5000 AU, but not highlighted are either not detected with sufficient SNR or excluded by optical-NIR-colors as described in the text. The number of finally interesting objects in each field can be found in Table 4.1, see text for in the indvidual descriptions.

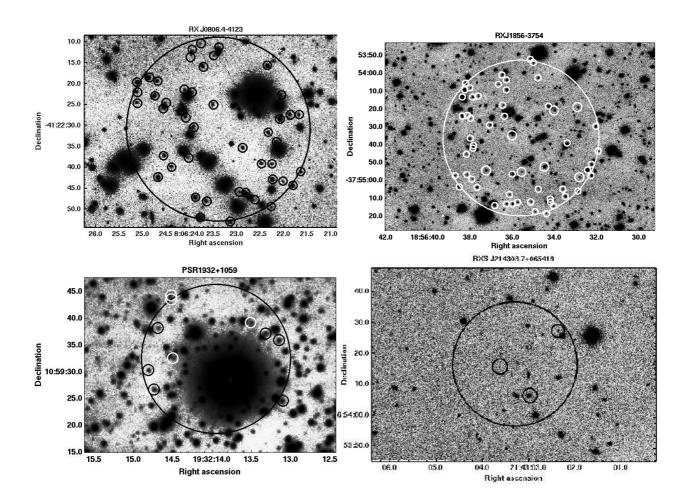


Figure 4.5: Interesting NIR-objects around the neutron stars (2) see Fig. 4.4 for description

#### 4.3.2 Second epoch observations

RX J1856.6-3754 was observed the second time in May 2006 using SOFI at the NTT. The epoch difference to the VLT ISAAC observations is 3.0 years. The expected shifts of possible co-moving objects are 980 mas in Right ascension (parallel to pixel coordinate x) and -177 mas in Declination (parallel to pixel coordinate y). At the nominal pixel scale of 147 mas for ISAAC which is the same for SOFI, this corresponds to 6.7 pixels in x and -1.2 pixels in y respectively.

The combined SOFI observations seem to be slightly less deep than the ISAAC observation given the magnitudes and number of detected objects. One of the 58 first-epoch-candidates with H=20.6 mag is not detected in the second epoch with a SNR of at least three. This is very likely due a close neighbouring source and more noise in the SOFI image at this position. All other 57 objects are detected, especially the interesting seven sources with determined optical-NIR-color(s). The photometric zeropoint calibration was done with 2MASS point sources like in the case of the first epoch observation. The faintest solitary object, which is detected with at least a SNR of three in the SOFI image, has  $H=21.6\pm0.4$  mag. This faintest object is also detected in the ISAAC observation having a magnitude of 21.1 mag. While the magnitudes agree well within the suspected error bars, this example shows the roughness of the photometric calibration by using 2MASS point sources.

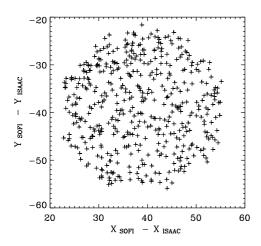


Figure 4.6: Pixel shifts between SOFI and ISAAC source positions around RX J1856.6-3754

All sources are detected with at least a SNR of three in both images. The x and y axes (pixel coordinates) are aligned with R.A. and negative DEC. respectively. For discussion of the found large pixel shifts, see text.

We compare the positions of a large number of objects detected in both observations to get an estimation of the scatter in positional shifts. The sources include those of the 57 objects, which are also detected with SOFI. We excluded apparent galaxies or source detections which are confused by nearby other sources. By this procedure, additional three of the 57 first-epoch-sources were excluded from the analysis described below. However, we made sure by visual inspection that these sources have no apparent positional shifts. In this way we checked also the 58th source, which is undetected but visible by eye in the SOFI-image.

The differences found in the source positions of the first and second epoch observations are large as can be seen in fig 4.6. The scatter is much larger than the expected shift for a possible co-moving object. However, in the left part of Fig. 4.7 a systematic shift between the SOFI and ISAAC positions is apparent taken the coordinate axes individually. This difference is suspected to be due to differing pixel scales in both instruments. Indeed, in the frame of the astrometric calibration by 2MASS PSC positions we find pixel scales of about 148 mas and 143 mas for the ISAAC and SOFI observations, respectively.

By a linear regression fit one can derive 'new' ISAAC positions without systematic shifts:  $x_{ISAAC}^{new} = 1.0321 \cdot x_{ISAAC} + 20.97$  and  $y_{ISAAC}^{new} = 1.0326 \cdot y_{ISAAC} - 59.73$ . The ascents have  $3\sigma$ -uncertainties of 0.0008, the zeropoints of 0.47 pixels in x and 0.55 pixels in y. The coordinates of the interesting objects are within [380, 800] for x and [400, 730] for y. The additional positional error, which is caused by the pixel scale transformation,

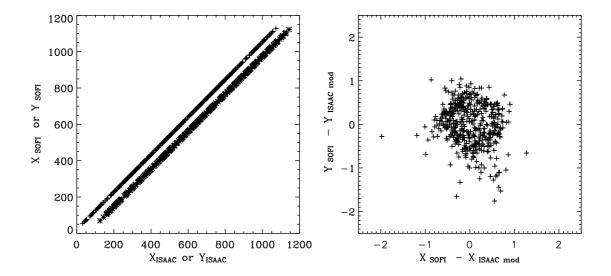


Figure 4.7: Harmonizing the pixel scale of ISAAC and SOFI observations

The systematic pixel shifts between the ISAAC and SOFI source positions are shown in the left figure. The upper simple crosses represent  $x_{SOFI}$  versus  $x_{ISAAC}$ , the lower stars  $y_{SOFI}$  versus  $y_{ISAAC}$  for sources detected in both observations. The systematics are due to different pixel scales. The derived linear transformation equations of the ISAAC pixel scale to the SOFI pixel scale lead to much smaller shifts between source positions in the first and second epoch observation (right image) in comparison to Fig. 4.6. Due to the linear regression fit the pixels shifts are now grouped around (0,0). There is no co-moving source having a +6.7 pixels shift in x or even +2.3 pixels considering the worst case error. For detailed discussion, see text. The object having a shift of around -2 pixels corresponds to a detection of actually two neighbouring sources, confusing the source detection algorithm.

is 1.1 pixels for x and 1.2 pixels for y in the worst case. This error has to be taken into account in addition to the positional errors of the source detections in both observations. Individual positional errors are usually  $3\sigma \approx 1$  pixel, for brighter objects the errors are even better. These errors were derived by spot checks of the GAIA detections via 2D-Gauss-fits in IDL. We note here the barycenter source detection algorithm of GAIA and positional errors expressed as the 2nd statistical moment, giving usually much smaller errors than the Gauss-fit errors. Keeping in mind that the source detection algorithm of GAIA was developed mainly for galaxies, the Gauss-fit errors seem to be more trustworthy for our point sources, especially as upper limits. Three times the largest positional gaussfit uncertainty of the interesting objects is  $3\sigma = 220$  mas or 1.6 pixels for the ISAAC observation. An error of the same order can be assumed in case of the SOFI observations. In the worst case, one has to consider an overall positional error of 4.4 pixels in x or y. As can be seen in the right part of Fig. 4.7 the individual positional shifts are much smaller. Given the large proper motion of 6.7 pixels in x for the neutron star one would expect at least a shift of 2.3 pixels in x for co-moving objects considering the worst case error. None of the interesting objects nor any other object in the image has such a fast motion, let alone 6.7 pixels. Therefore one can exclude co-moving objects around RX J1856.6-3754 down to the SOFI  $3\sigma$  detection limit of H=21.6 mag. At a distance of 117 pc and an age of 1 Myr this correponds to the exclusion of objects heavier than 0.007  $M_{\odot}$  or 7.3 Jupiter masses following equation 4.1 and Burrows et al. (1997). At the recently reported distance of 161 $^{+18}_{-14}$  pc by van Kerkwijk & Kaplan (2006), objects heavier than 0.01  $\rm M_{\odot}$  or 10.5 Jupiter masses are excluded.

One can think to combine both deep H-band observations to get an estimate for a deeper upper NIR-limit at the position of the neutron star. Even in case of comparable observerving conditions with the same noise, the overall noise decreases only with  $\sqrt{2}$  resulting in a magnitude gain of only 0.38 mag, probably too small to note in our rough magnitude estimates. However, we transformed the ISAAC image array to the SOFI pixel scale by the formulae noted above using IDL. By this transformation we get gaps in the enlarged image which were filled with the average of the neighbouring pixels. Then we combined this result with the SOFI image using IRAF. Astrometry and rough photometry were obtained again with the help of the 2MASS point sources using GAIA. The source having H=21.1 mag and H=21.6 mag in the ISAAC and SOFI observations, respectively, has H=21.2 mag in the combined image. The faintest reliable objects have H=22.6 mag at a detection SNR of at least three. As the magnitude error from the source algorithm is large for these sources (around 0.3 mag), an error of around 0.5 mag applies. The new NIR limit of  $H=22.6\pm0.5$  for the neutron star is in agreement with the ISAAC ( $H=22.1\pm0.4$ ) value of the first epoch within the error bars.

**PSR J1932+1059** was also observed the second time in May 2006 using SOFI at the NTT. The epoch difference to the VLT ISAAC observations is 2.9 years. The expected shifts of possible co-moving objects are therefore 272 mas in Right ascension (antiparallel to pixel coordinate x) and 126 mas in Declination (parallel to pixel coordinate y). At the nominal pixel scale of 143 mas for SOFI, this corresponds to -1.9 pixels in x and 0.9 pixels in y respectively.

The combined SOFI observations are less deep than with ISAAC due to the observing conditions (small visibility time window, not so good weather on the last night). Of the 10 interesting objects found in the first epoch, only four are detectable with a SNR of at least three in the SOFI observation.

We compared the positions of a large number of objects detected in both observations

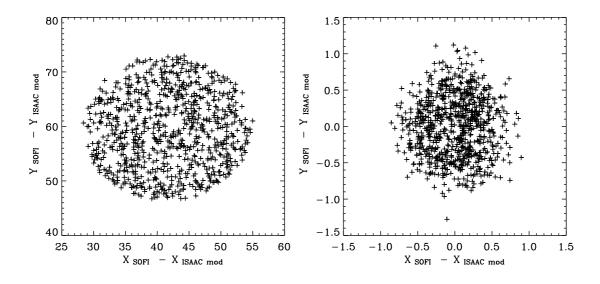


Figure 4.8: Pixel shifts between sources positions of two epochs in the field of PSR J1932+1059. The left figure shows the differences between the source positions without considering the different pixel scales of SOFI and ISAAC. The right figure was obtained by transforming the ISAAC image to SOFI pixel scale first, then the pixel shifts were obtained between SOFI and this transformed ISAAC image. Thanks to the linear regression done for harmonizing the pixel scales, the pixel shifts are now grouped around (0,0), and are much smaller than in the left image. One would expect differences of -1.9 pixels in x and 0.9 pixels in y for possible co-moving objects. There is no source with such high shifts in x. However, substellar companions are not excluded completely due to large positional error bars, see text.

to get an estimation of the scatter in positional shifts. We excluded apparent galaxies or source detections which are confused by nearby other sources except when these sources are within 5000 AU around the neutron star. The positional shifts found from the first to the second epoch observation are large as can be seen in the left part of fig 4.8. The scatter is much larger than the expected shift for a possible co-moving object and can be related to the different pixel scales. The found systematic shifts between the SOFIand ISAAC coordinates can be described by a linear relation individually for x and y in a similar way as given above for RX J1856.6-3754. By a linear regression fit one can derive 'new' ISAAC positions without systematic shifts:  $x_{ISAAC}^{new} = 1.0331 \cdot x_{ISAAC} + 24.23$ and  $y_{ISAAC}^{new} = 1.0333 \cdot y_{ISAAC} + 42.61$ . The ascents have  $3\sigma$ -uncertainties of 0.001, the zeropoints of 0.56 pixels in x and 0.60 pixels in y. The coordinates of the interesting objects are within [440, 650] for x and [480, 690] for y. The additional positional error, which is caused by the pixel scale transformation, is 1.2 pixels for x and 1.3 pixels for y in the worst case. This error of at least 1 pixel has to be taken into account in addition to the positional errors of the source detections in both observations. Individual positional errors are usually  $3\sigma \approx 1$  pixel, even better for bright objects. These errors were derived by spot checks of the GAIA detections via 2D-Gauss-fits in IDL, similar to the case of RX J1856.6-3754. Three times the largest positional gauss-fit uncertainty of the interesting objects is  $3\sigma = 180$  mas or 1.3 pixels for the ISAAC observation. In the theoretic case of the same pixel scale for both epochs one could discuss the interesting sources individually, whether their positional errors are small enough to be sensitive to a possible 1.9 pixels common proper motion shift. Here, for most sources we cannot exclude an error of the same order as the possible common proper motion shift due to the extra positional uncertainty considering the different pixel scales. In the right part of Fig. 4.8 there is no source with a shift larger than 1 pixel. The sources are clustered relatively closely together. These small shifts indicate pleasingly lower errors than derived by the 2D-gauss-fits. It also shows that there is no exceptional source to discuss. While it seems likely that there is no co-moving object down to the limit of the faintest interesting source we cannot completely rule out a misinterpretation due to possible large errors for some detections, which could 'hide' a co-moving object. If one could confirm the sources as non co-moving with later observations with a larger epoch difference, this would correspond to an exclusion of brown dwarfs around PSR J1932+1059 down to  $0.05~{\rm M}_{\odot}$  or 52 Jupiter masses for an age of 3.1 Myr and a distance of 361 pc.

The combination of the ISAAC and the SOFI images leads to a deeper upper NIR-limit for the neutron star. However, the detection limit at the position of PSR J1932+1059 is still determined by the nearby bright object. The faintest object close to the bright source near the neutron star has H = 19.5 mag. This object was detected together with

a neighbouring source as only one object in the first epoch observation before. Two other objects, situated very close ( $\approx 3''$ ) to the bright object and having around H=17 mag in the first epoch observation, are not detected in the combined image with a SNR of at least three. This could be due to the very noisy SOFI observation. While the H-band magnitudes of the first epoch and the combined image agree well within error bars for sources lying away from bright objects, a comparision shows differences of up to 0.8 mag for the H-band magnitudes of sources close to the bright object. Usually the sources are fainter by around 0.3 mag in the combined image. This effect illustrates the uncertainty of the magnitude estimation in the vicinity of the H=8.8 mag bright source. Therefore, the new NIR limit of PSR J1932+1059 is H=19.5 mag, but a large magnitude error is likely and suspected to be around 1 mag.

#### 4.4 Conclusions

Of the ten southern young neutron stars, eight are interesting for second-epoch observations considering the NIR-optical colors and faintness of possible substellar objects within 5000 AU around the neutron star. Currently we know only the proper motion of four of them. Two of them have been observed already for a second time, the two others are sheduled in winter 2006 at the VLT. In the case of the already re-observed RX J1856.6-3754 we can exclude co-moving substellar companions heavier than 10.5 Jupiter masses (at an assumed age of 1 Myr and a distance of 161 pc). Probably, there are also no substellar companions heavier than 52 Jupiter masses for PSR J1932+1059 (3.1 Myrs, 361 pc). However, due to the large positional errors this has to be confirmed with repeated observations, preferably with the same instrument as used for the first epoch observation. We derived upper NIR-limits for all observed neutron stars, except for RXS J214303.7+065419, where the positional error is still large and a NIR object is present within its positional uncertainity. However, the achieved H-band magnitudes are not deep enough to test, for example, the extraploation of the optical spectrum of RX J1856.6-3754.

# Chapter 5

# **Summary and Outlook**

## 5.1 Summary

This thesis concentrates on the X-ray thermal isolated neutron stars like the Magnificent Seven one the one hand, and on substellar companions around the M7 and other young neutron stars on the other hand. In both cases candidate searches based on new methods and new data are important parts of the thesis.

Considering the X-ray thermal isolated neutron stars, the interesting M7 are rather diverse in detail and a larger statistical basis is necessary to address for example geometrical viewing effects, and furthermore to study the differences and connections between this neutron star population and others like radio pulsars or the objects thought to be magnetars. Apart from a candidate list for follow-up observations we present predictions for the observable number of neutron stars with strong thermal emission from a population synthesis model considering for the first time the inhomogeneous distribution of the progenitor stars and of the X-ray absorbing interstellar medium. Both distributions strongly influence the number of X-ray thermal isolated neutron stars we can expect to observe towards a given direction in the Galaxy.

Considering substellar companions to young neutron stars, we apply for the first time the direct imaging method in constrast to the indirect radio pulse timing technique used before for old radio pulsars. Our method is sensitive to find brown dwarfs and gas planets around the young neutron stars. In principle, it will be possible to directly study the companion spectra afterwards. Substellar companions found would be also interesting to obtain the masses of the neutron stars by Keplerian motion. Together with the possible radius determination in case of the M7 this may constrain the equation of state of the neutron stars. We present the first results of the search for substellar companions around two neutron stars with sufficiently high proper motion (one M7-member, one radio pul-

sar). In case of the other eight investigated neutron stars, half of them M7-members, only first epoch observations are available, and interesting companion candidates still need to be confirmed by second epoch observations.

In the following the main details are individually summarized for each subject investigated in this thesis.

The absorption of soft X-rays by the ISM The interstellar absorption of soft X-rays can be addressed mainly by quantifying the hydrogen column density if one assumes the same abundances and cross sections of the elements along the line of sight. As there was no 3D model of the hydrogen column density which would have covered distances from the Local Bubble to kiloparsec scale at sufficient detail, we developed two 3D models of the hydrogen column density up to distances of 4.5 kpc. This was done by combining and harmonizing the very detailed Natrium column density data by Lallement et al. (2003) with a large scale extinction study by Hakkila et al. (1997) one the one hand, and an analytical description of the ISM distribution on the other hand. For consistency we tested our models with open cluster data, where distances are known and hydrogen column densities can be obtained from reddening measurements. Open clusters provide reliable averaged values, included in our models. Furthermore, a few other objects like neutron stars with known hydrogen column densities from X-ray observations and parallactic distances have been tested. The results indicate that the models are well-suited for statistical studies like the intended population synthesis. They may also be used to estimate distances towards sources where only hydrogen column densities are available. Of course the obtained distances are not as accurate as for example parallactic distances, but the estimations applying our ISM models are much more realisitic than in case of the usually applied approximation of the hydrogen column density increasing linearly with distance. We obtained reasonable estimates towards two of the Magnificent Seven with hitherto unknown distances. Here, the values obtained by applying both of our ISM models agree with each other in case of RX J0720.4-3125 at  $250 \pm 25$  pc and RX J0806.4-4123 at  $240 \pm 25$  pc. The recent preliminary paralleletic distance of RX J0720.4-3125,  $330^{+170}_{-80}$  pc, by van Kerkwijk & Kaplan (2006) is in agreement with our estimation. The main advantage of the extinction model is the consideration of (large) local ISM inhomogeneities for distances above 230 pc, its weakness is the bad sampling resulting in unlikely, nearly constant values of the hydrogen column density over long distance ranges. The analytical model tends to overpredict the absorption in case of the open cluster data at distances larger than 1 kpc. Based on averaging over galactocentric radii, this model is furthermore not sensitive to local inhomogeneities of the ISM at distances above 230 pc. In contrast to the extinction model the analytical model has no obvious data 'holes' and seems to be the better choice at locations of badly sampled data in the extinction model. We stress the influence of different sets of elemental abundances and cross-sections on the interstellar absorption of soft X-rays by comparing two sets commonly used in the analysis and interpretation of X-ray spectra. At high hydrogen column densities the obtained flux differences can be as high as a factor of two.

Population synthesis of young nearby isolated neutron stars The population synthesis started by Popov et al. (2000b, 2003) and Popov et al. (2005) was significantly improved by including OB associations as locations of the neutron star progenitors and considering also approximate ages of these OB associations. As a result, the predicted observable young cooling neutron stars appear concentrated towards the directions of the closest OB associations and not only along the Galactic and Gould Belt disk as it was found before.

Apart from minor improvements like a more realistic observing energy range for ROSAT, a better sampling of the instrumental response, or inclusion of newer abundance and cross sections of the elements, we implemented the two 3D column density models we developed in order to consider also the local inhomogeneities of the ISM. This reduced the observable number of young cooling NSs in the direction of strongly absorbing material, e.g. in or behind the Taurus dark cloud. The derived  $\log N$ - $\log S$ -curves, which represent the numbers of expected neutron stars at given ROSAT count rates, differ for the two ISM distributions, especially at the bright and faint end, which emphasizes the importance of realistic absorption models.

The results of the population synthesis motivate precise searches for new M7-like candidates towards favourable lines of sight. The comparison of the obtained  $\log N$ - $\log S$ -curves with the actually observed number of NSs with strong thermal emission shows that our initially chosen parameters and models (e.g. birth rates, cooling curves, initial NS masses) are reasonable but can still be improved. We want to stress that currently one can evaluate certain assumptions in the population synthesis model only with restrictions by comparing the simulated results with the observations. The uncertainties in the different ingredients are still large and the observed small number of NSs is certainly biased towards faint objects. Thus, although it is possible to exclude rather unlikely assumptions, this is only a starting point and one has to be careful concerning an identification of a set of most promising parameters and underlying models.

New candidates of X-ray thermal neutron stars Utilizing the deep optical Sloan Digitial Sky Survey (SDSS) we searched for new Magnificent Seven (M7)-like objects in the ROSAT All Sky Survey (RASS), the ROSAT pointings with the PSPC and HRI instrument as well as in deep XMM-Newton pointings. We found nine good RASS candidates, one good ROSAT PSPC pointing candidate, two good and two uncertain ROSAT HRI

pointing candidates as well as three good and four uncertain XMM-Newton candidates for M7-like neutron stars. Unfortunately, the candidates are all at high galactic latitudes where the predicted number of observable X-ray thermal neutron stars is rather small and the expected confusion by extragalactic sources rather large. In particular, extragalactic counterparts cannot be excluded in case of the faint ROSAT or XMM-Newton pointing sources because the respective limiting X-ray to optical flux ratios are not constraining enough. Only follow-up observations can clarify the nature of these X-ray sources. The nine good RASS sources found are scheduled in the on-going *Chandra* observation cycle. In the framework of finding soft X-ray sources in the XMM-Newton EPIC-pn pointings we tested a method to consider counts at low energies down to 150 eV in contrast to the lower energy border of 200 eV, which is usually applied because of noise at lower energies. Next to the noise pattern we also consider the hot pixels which newly appear at these low energies. We identified several likely soft X-ray sources which are not known as detections in the standard energy bands. The noise contribution among the initial detections, however, is still very strong. Visual inspection is definitely needed as well as follow-up observations to confirm very faint sources.

Substellar companions around young neutron stars Ten young and close NSs have been observed in the near infrared (NIR) with ESO's Very Large Telescope to obtain the first epoch images for our continuing substellar companion search. In case of eight NS fields, many interesting candidates have been pre-selected by their NIR-optical colors. The limiting H-band magnitudes at the positions of the neutron stars have been derived for all objects. They are, however, only upper limits and thus weak constraints on the spectra of the NSs. For two neutron stars with sufficiently high proper motion we have already obtained the second epoch images by NIR-observations with ESO's New Technology Telescope. In case of RX J1856.6-3754 we can exclude co-moving substellar companions heavier than 10.5 Jupiter masses assuming a neutron star age of 1 Myr and a distance of 161 pc. Probably, there are also no substellar companions heavier than 52 Jupiter masses in case of PSR J1932+1059 (3.1 Myrs, 361 pc).

### 5.2 Future Plans

In the following we summarize follow-up projects resulting directly from the investigations presented in this thesis. The projects are ordered as the chapters before. At the end we mention an additional project which has already been started during the last year, but did not lead to results due to technical problems.

The absorbing ISM distribution It is planned to test and further refine our 3D-models of the ISM, firstly by new data (e.g. the infrared color excess data obtained with

the help of 2MASS by Marshall et al. 2006) and secondly by more X-ray detected (test) objects with determined hydrogen column densities and known distances.

Population synthesis of young isolated neutron stars In collaboration with S. B. Popov we started to work on including and discussing different NS cooling curves. Furthermore, the role of the initial mass spectra for newly born neutron stars and the age of the observable NSs are in the focus of started discussions. It is also planned to investigate the inclusion of further details as hot spots on the surface of the NSs or possible atmospheres in our simulations.

To overcome the problem of poor statistics in our galactic maps which show the predicted neutron star number we will increase the run number significantly.

For the upcoming All Sky Survey with MPE's eROSITA we intend to estimate the expected observable number of isolated neutron stars emitting thermal X-rays by introducing eROSITA's instrumental response into our code.

New candidates of X-ray thermal isolated neutron stars It is planned to investigate our X-ray thermal isolated neutron star candidates by X-ray and optical follow-up observations. The RASS candidates are already scheduled for *Chandra* observations in collaboration with M. Agüeros. But also in case of the faint pointing candidates, X-ray observations are needed to confirm the candidate detections and the suspected soft X-ray source spectra as well as to check for X-ray variability. Optical observations are necessary to derive more constraining X-ray to optical flux ratios.

A promising future search strategy for new X-ray thermal isolated neutron stars candidates is the utilization of deep optical archival data in combination with X-ray pointings of good spatial resolution and the concentration on galactic regions with an expected high number of NSs emitting thermal X-rays.

A catalogue of soft XMM-Newton X-ray sources It has been shown that it is possible to consider lower energies than the standard low energy border of 200 eV regarding source detections in XMM-Newton EPIC-pn observations. Faint soft sources have been identified that are not known from the XMM-Newton Serendipitous Source Catalogue (XMM-SSC2, pre-released 20.7.2006). For the XMM-SSC2 the standard energy range (0.2 keV to 10 keV) was used for the source detection algorithm. We will continue the work to find soft X-ray sources in deep XMM-Newton EPIC-pn pointings and to compare the result with the final XMM-SSC2 entries. From our X-ray thermal isolated neutron stars candidate search it seems useful to additionally provide the counts in harder X-ray energy bands for each identified soft source. One may exclude unwanted spectral behaviour in the hard X-ray bands by these additional data. In case of sources missed by the XMM-SSC2 this would be especially useful as there is likely no other XMM-Newton catalogue with this information.

Substellar companions around young neutron stars The next second epoch NIR-observations are scheduled at ESO's VLT for Geminga and RX J0720.4-3125 in the observing period P78. As the *H*-band images will be done with the same instrument as the first epoch observations, smaller positional errors, thus clear identifications or exclusions are expected.

Possible further steps to improve the current limits on PSR J1932+1059 are on the one hand the subtraction of the point spread function at the position of the bright star to reduce source confusion in case of the objects closest to it. Furthermore we plan to determine the possible NTT SOFI image distortions by also scheduled ESO observations of an open star cluster. Considering these image distortions may reduce the positional errors further. It is also still interesting to re-observe PSR J1932+1059 to take into account all the sources identified as interesting from the first epoch observation as the NTT SOFI second epoch image is not as deep as the first epoch VLT ISAAC observation.

Radio observations of X-ray thermal isolated neutron stars We observed two of the Magnificent Seven with the 100 m Effelsberg telescope at 1.4 GHz. We did not detect regular pulsations from 1RXS J130848.6+212708 and RX J1605.3+3249 applying the Fast Folding algorithm by B. Klein (MPIfR, Bonn). This algorithm is especially suited to detect relatively long periods which are likely for these sources because of their long X-ray pulse periods known for 1RXS J130848.6+212708 and suspected in case of RX J1605.3+324. Up to now we did not find any single pulses which would be similar to those of the Rotational Radio Transients found by McLaughlin et al. (2006).

Due to technical problems the observations have to be repeated, are re-scheduled and will be analysed again. Especially, we will re-investigate the possibility of single pulses typical for Rotational Radio Transients.

# **Bibliography**

- Agüeros, M. A., Anderson, S. F., Margon, B., et al., 2006, Candidate Isolated Neutron Stars and Other Optically Blank X-Ray Fields Identified from the ROSAT All-Sky and Sloan Digital Sky Surveys, AJ, 131, 1740
- Amôres, E. B. & Lépine, J. R. D., 2005, Models for Interstellar Extinction in the Galaxy, AJ, 130, 659
- Anders, E. & Ebihara, M., 1982, Solar-system abundances of the elements, Geochim. Cosmochim. Acta, 46, 2363
- Anders, E. & Grevesse, N., 1989, Abundances of the elements Meteoritic and solar, Geochim. Cosmochim. Acta, 53, 197
- Anderson, S. F., Voges, W., Margon, B., et al., 2003, A Large, Uniform Sample of X-Ray-Emitting AGNs: Selection Approach and an Initial Catalog from the ROSAT All-Sky and Sloan Digital Sky Surveys, AJ, 126, 2209
- Appenzeller, I., Fricke, K., Furtig, W., et al., 1998, Successful commissioning of FORS1 the First Optical Instrument on the VLT., The Messenger, 94, 1
- Arnett, W. D., Schramm, D. N., & Truran, J. W., 1989, On relative supernova rates and nucleosynthesis roles, ApJ, 339, L25
- Arzoumanian, Z., Chernoff, D. F., & Cordes, J. M., 2002, The Velocity Distribution of Isolated Radio Pulsars, ApJ, 568, 289
- Baade, W. & Zwicky, F., 1934, On Super-novae, Proceedings of the National Academy of Science, 20, 254
- Becker, W. & Pavlov, G. G., 2002, The Milky Way Pulsars and Isolated Neutron Stars, ArXiv Astrophysics e-prints
- Bertin, E. & Arnouts, S., 1996, SExtractor: Software for source extraction., A&AS, 117, 393
- Blackburn, J. K., 1995, FTOOLS: A FITS Data Processing and Analysis Software Package. In: R. A. Shaw, H. E. Payne, and J. J. E. Hayes (eds.), pp 367—+
- Blaes, O. & Madau, P., 1993, Can we observe accreting, isolated neutron stars?, ApJ, 403, 690
- Blaha, C. & Humphreys, R. M., 1989, A comparison of the luminosity functions in U, B, and V and their relationship to the initial mass function for the Galaxy and the Magellanic Clouds, AJ, 98, 1598
- Blaschke, D., Grigorian, H., & Voskresensky, D. N., 2004, Cooling of neutron stars. Hadronic model, A&A, 424, 979

- Bochkarev, N. G., 1992, Basics of the ISM Physics, Moscow: Moscow University Press
- Braje, T. M. & Romani, R. W., 2002, RX J1856-3754: Evidence for a Stiff Equation of State, ApJ, 580, 1043
- Breitschwerdt, D., 1998, Introductory Lecture: The Local and General Interstellar Medium, LNP Vol. 506: IAU Colloq. 166: The Local Bubble and Beyond, 506, 5
- Burrows, A., Marley, M., Hubbard, W. B., et al., 1997, A Nongray Theory of Extrasolar Giant Planets and Brown Dwarfs, ApJ, 491, 856
- Burwitz, V., Haberl, F., Neuhäuser, R., et al., 2003, The thermal radiation of the isolated neutron star RX J1856.5-3754 observed with Chandra and XMM-Newton, A&A, 399, 1109
- Campana, S., Lazzati, D., Panzera, M. R., & Tagliaferri, G., 1999, The Brera Multiscale Wavelet ROSAT HRI Source Catalog. II. Application to the HRI and First Results, ApJ, 524, 423
- Caraveo, P. A., Bignami, G. F., Mignani, R., & Taff, L. G., 1996, Parallax Observations with the Hubble Space Telescope Yield the Distance to Geminga, ApJ, 461, L91+
- Caraveo, P. A., Lattanzi, M. G., Massone, G., et al., 1998, HIPPARCOS positioning of Geminga: how and why, A&A, 329, L1
- Cardelli, J. A., Meyer, D. M., Jura, M., & Savage, B. D., 1996, The Abundance of Interstellar Carbon, ApJ, 467, 334
- Casey, B. W., Mathieu, R. D., Vaz, L. P. R., Andersen, J., & Suntzeff, N. B., 1998, The Pre-Main-Sequence Eclipsing Binary TY Coronae Australis: Precise Stellar Dimensions and Tests of Evolutionary Models, AJ, 115, 1617
- Chatterjee, S., Cordes, J. M., Vlemmings, W. H. T., et al., 2004, Pulsar Parallaxes at 5 GHz with the Very Long Baseline Array, ApJ, 604, 339
- Chieregato, M., Campana, S., Treves, A., et al., 2005, Blank field sources in the ROSAT HRI Brera multiscale wavelet catalog, A&A, 444, 69
- Condon, J. J., Cotton, W. D., Greisen, E. W., et al., 1998, The NRAO VLA Sky Survey, AJ, 115, 1693
- Cropper, M., Zane, S., Ramsay, G., Haberl, F., & Motch, C., 2001, Modelling the spin pulse profile of the isolated neutron star RX J0720.4-3125 observed with XMM-Newton, A&A, 365, L302
- Dambis, A. K., Mel'nik, A. M., & Rastorguev, A. S., 2001, Trigonometric Parallaxes and a Kinematically Adjusted Distance Scale for OB Associations, Astronomy Letters, 27, 58
- D'Amico, N., Stappers, B. W., Bailes, M., et al., 1998, The Parkes Southern Pulsar Survey III. Timing of long-period pulsars, MNRAS, 297, 28
- Danner, R., 1998a, Searching for old neutron stars with ROSAT. I. Soft X-ray sources in molecular clouds at high galactic latitude, A&AS, 128, 331
- Danner, R., 1998b, Searching for old neutron stars with ROSAT. II. Soft X-ray sources in galactic dark clouds, A&AS, 128, 349
- de Boer, H., 1991, Some problems for galactic hydrostatic equilibria. In: H. Bloemen (ed.), pp 333–336

- de Vries, C. P., Vink, J., Méndez, M., & Verbunt, F., 2004, Long-term variability in the X-ray emission of RX J0720.4-3125, A&A, 415, L31
- de Zeeuw, P. T., Hoogerwerf, R., de Bruijne, J. H. J., Brown, A. G. A., & Blaauw, A., 1999, A HIPPARCOS Census of the Nearby OB Associations, AJ, 117, 354
- Dekker, H., Delabre, B., & Dodorico, S., 1986, ESO's Multimode Instrument for the Nasmyth focus of the 3.5 M New Technology Telescope. In: D. L. Crawford (ed.), pp 339–348
- Dennerl, K., Aschenbach, B., Briel, U. G., et al., 2004, *Improving XMM-Newton EPIC pn data at low energies: method and application to the Vela SNR*. In: G. Hasinger and M. J. L. Turner (eds.), pp 61–72
- Devillard, N., 1999, Infrared Jitter Imaging Data Reduction: Algorithms and Implementation. In: D. M. Mehringer, R. L. Plante, and D. A. Roberts (eds.), pp 333-+
- Devillard, N., 2001, ESO C Library for an Image Processing Software Environment (eclipse). In: F. R. Harnden, Jr., F. A. Primini, and H. E. Payne (eds.), pp 525-+
- Dickey, J. M. & Lockman, F. J., 1990, H I in the Galaxy, ARA&A, 28, 215
- D'Odorico, S., Beletic, J. W., Amico, P., et al., 1998, Commissioning of a 4Kx4K CCD mosaic and the new ESO FIERA CCD controller at the SUSI-2 imager of the NTT. In: S. D'Odorico (ed.), pp 507–511
- Dodson, R., Legge, D., Reynolds, J. E., & McCulloch, P. M., 2003, The Vela Pulsar's Proper Motion and Parallax Derived from VLBI Observations, ApJ, 596, 1137
- Drimmel, R., Cabrera-Lavers, A., & López-Corredoira, M., 2003, A three-dimensional Galactic extinction model, A&A, 409, 205
- Duncan, R. C. & Thompson, C., 1992, Formation of very strongly magnetized neutron stars Implications for gamma-ray bursts, ApJ, 392, L9
- Ertan, U., Erkut, M. H., Eksi, K. Y., & Alpar, M. A., 2006, A Fallback Disk Around a Neutron Star Spinning Down While Accreting, astro-ph/0606259
- ESA, 1997, The Hipparcos and Tycho Catalogues (ESA 1997), VizieR Online Data Catalog, 1239, 0
- Faherty, J., 2006, The Trigonometric Parallax of Geminga. I. The Technique. In: Proceedings of the Conference: Isolated Neutron Stars: from the Interior to the Surface, London
- Ferlet, R., Vidal-Madjar, A., & Gry, C., 1985, NA I as a tracer of H I in the diffuse interstellar medium, ApJ, 298, 838
- Fitzgerald, M. P., 1968, The Distribution of Interstellar Reddening Material, AJ, 73, 983
- Forbrich, J., Preibisch, T., & Menten, K. M., 2006, Radio and X-ray variability of young stellar objects in the Coronet cluster, A&A, 446, 155
- Fukugita, M., Ichikawa, T., Gunn, J. E., et al., 1996, The Sloan Digital Sky Survey Photometric System, AJ, 111, 1748
- Gaensler, B. M., Jones, D. H., & Stappers, B. W., 2002, An Optical Bow Shock around the Nearby Millisecond Pulsar J2124-3358, ApJ, 580, L137

- Geppert, U., Kueker, M., & Page, D., 2005, Temperature distribution in magnetized neutron star crusts. II. The effect of a strong toroidal component, ArXiv Astrophysics e-prints
- Geppert, U., Küker, M., & Page, D., 2004, Temperature distribution in magnetized neutron star crusts, A&A, 426, 267
- Golden, A., Brisken, W. F., Thorsett, S. E., Benjamin, R. A., & Goss, W. M., 2005, *Implications of a VLBA Parallax for PSR B0656+14*, Baltic Astronomy, 14, 436
- Golimowski, D. A., Leggett, S. K., Marley, M. S., et al., 2004, L' and M' Photometry of Ultracool Dwarfs, AJ, 127, 3516
- Greenstein, G. & Hartke, G. J., 1983, Pulselike character of blackbody radiation from neutron stars, ApJ, 271, 283
- Grenier, I. A., 2000, Gamma-ray sources as relics of recent supernovae in the nearby Gould Belt, A&A, 364, L93
- Grupe, D., 1996, Properties of bright soft X-ray selected ROSAT AGN, Ph.D. Thesis
- Guseinov, O. H., Ankay, A., & Tagieva, S. O., 2005, Influence of Neutron Star Parameters on Evolutions of Different Types of Pulsar, Ap&SS, 298, 553
- Haberl, F., 2004, AXPs and X-ray-dim isolated neutron stars: recent XMM-Newton and Chandra results, Advances in Space Research, 33, 638
- Haberl, F., 2006, The Magnificent Seven: Magnetic fields and surface temperature distributions. In: Proceedings of the Conference: Isolated Neutron Stars: from the Interior to the Surface, London, astro-ph/0609066
- Haberl, F., Motch, C., Buckley, D. A. H., Zickgraf, F.-J., & Pietsch, W., 1997, RXJ0720.4-3125: strong evidence for an isolated pulsating neutron star., A&A, 326, 662
- Haberl, F., Motch, C., Zavlin, V. E., et al., 2004a, The isolated neutron star X-ray pulsars ¡AS-TROBJ¿RX J0420.0-5022¡/ASTROBJ¿ and ¡ASTROBJ¿RX J0806.4-4123¡/ASTROBJ¿: New X-ray and optical observations, A&A, 424, 635
- Haberl, F. & Pietsch, W., 1999, A ROSAT PSPC catalogue of X-ray sources in the LMC region, A&AS, 139, 277
- Haberl, F., Schwope, A. D., Hambaryan, V., Hasinger, G., & Motch, C., 2003, A broad absorption feature in the X-ray spectrum of the isolated neutron star RBS1223 (1RXS J130848.6+212708), A&A, 403, L19
- Haberl, F., Turolla, R., de Vries, C. P., et al., 2006, Evidence for precession of the isolated neutron star ¡ASTROBJ¿RX J0720.4-3125¡/ASTROBJ¿, A&A, 451, L17
- Haberl, F. & Zavlin, V. E., 2002, XMM-Newton observations of the isolated neutron star RX J0806.4-4123, A&A, 391, 571
- Haberl, F., Zavlin, V. E., Trümper, J., & Burwitz, V., 2004b, A phase-dependent absorption line in the spectrum of the X-ray pulsar RX J0720.4-3125, A&A, 419, 1077
- Hakkila, J., Myers, J. M., Stidham, B. J., & Hartmann, D. H., 1997, A Computerized Model of Large-Scale Visual Interstellar Extinction, AJ, 114, 2043

- Hambaryan, V., Hasinger, G., Schwope, A. D., & Schulz, N. S., 2002, Discovery of 5.16 s pulsations from the isolated neutron star RBS 1223, A&A, 381, 98
- Harding, A. K. & Lai, D., 2006, Physics of strongly magnetized neutron stars, Reports of Progress in Physics, 69, 2631
- Hasinger, G., Miyaji, T., & Schmidt, M., 2005, Luminosity-dependent evolution of soft X-ray selected AGN. New Chandra and XMM-Newton surveys, A&A, 441, 417
- Helfand, D. J., Chanan, G. A., & Novick, R., 1980, Thermal X-ray emission from neutron stars, Nature, 283, 337
- Henbest, N. & Couper, H., 1994, The guide to the galaxy, Cambridge: University Press, —c1994
- Henke, B. L., Lee, P., Tanaka, T. J., Shimabukuro, R. L., & Fujikawa, B. K., 1982, Low-Energy X-Ray Interaction Coefficients: Photoabsorption, Scattering and Reflection, E=100-2000 eV, Z=1-94, Atomic Data and Nuclear Data Tables, 27, 1
- Hewish, A., Bell, S. J., Pilkington, J. D., Scott, P. F., & Collins, R. A., 1968, Observation of a Rapidly Pulsating Radio Source, Nature, 217, 709
- Hobbs, G., Lorimer, D. R., Lyne, A. G., & Kramer, M., 2005, A statistical study of 233 pulsar proper motions, MNRAS, 360, 974
- Hobbs, G., Manchester, R., Teoh, A., & Hobbs, M., 2004, *The ATNF Pulsar Catalog.* In: F. Camilo and B. M. Gaensler (eds.), pp 139-+
- Hobbs, L. M., Penprase, B. E., Welty, D. E., Blitz, L., & Magnani, L., 1988, On the nearest molecular clouds. II MBM 12 and 16, ApJ, 327, 356
- Hunter, I., Smoker, J. V., Keenan, F. P., et al., 2006, Early-type stars observed in the ESO UVES Paranal Observatory Project I. Interstellar NaI UV, TiII and CaII K observations, MNRAS, pp 277—+
- Jackson, M. S. & Halpern, J. P., 2005, A Refined Ephemeris and Phase-resolved X-Ray Spectroscopy of the Geminga Pulsar, ApJ, 633, 1114
- Jonker, P. G., van der Klis, M., & Groot, P. J., 2003, The mass of the neutron star in the low-mass X-ray binary 2A 1822 371, MNRAS, 339, 663
- Kalberla, P. M. W., Burton, W. B., Hartmann, D., et al., 2005, The Leiden/Argentine/Bonn (LAB) Survey of Galactic HI. Final data release of the combined LDS and IAR surveys with improved stray-radiation corrections, A&A, 440, 775
- Kaminker, A. D., Yakovlev, D. G., & Gnedin, O. Y., 2002, Three types of cooling superfluid neutron stars: Theory and observations, A&A, 383, 1076
- Kaplan, D. L., Kulkarni, S. R., & van Kerkwijk, M. H., 2002a, A Probable Optical Counterpart to the Isolated Neutron Star RX J1308.6+2127, ApJ, 579, L29
- Kaplan, D. L., Kulkarni, S. R., & van Kerkwijk, M. H., 2003, The Optical Counterpart of the Isolated Neutron Star RX J1605.3+3249, ApJ, 588, L33
- Kaplan, D. L. & van Kerkwijk, M. H., 2005a, A Coherent Timing Solution for the Nearby Isolated Neutron Star RX J0720.4-3125, ApJ, 628, L45

- Kaplan, D. L. & van Kerkwijk, M. H., 2005b, A Coherent Timing Solution for the Nearby Isolated Neutron Star RX J1308.6+2127/RBS 1223, ApJ, 635, L65
- Kaplan, D. L., van Kerkwijk, M. H., & Anderson, J., 2002b, The Parallax and Proper Motion of RX J1856.5-3754 Revisited, ApJ, 571, 447
- Kaspi, V. M., Roberts, M. S. E., & Harding, A. K., 2004, Isolated Neutron Stars, astro-ph/0402136
- Kenyon, S. J. & Hartmann, L., 1995, Pre-Main-Sequence Evolution in the Taurus-Auriga Molecular Cloud, ApJS, 101, 117
- Kharchenko, N. V., Piskunov, A. E., Röser, S., Schilbach, E., & Scholz, R.-D., 2005a, 109 new Galactic open clusters, A&A, 440, 403
- Kharchenko, N. V., Piskunov, A. E., Röser, S., Schilbach, E., & Scholz, R.-D., 2005b, Astrophysical parameters of Galactic open clusters, A&A, 438, 1163
- Kirkpatrick, J. D., Reid, I. N., Liebert, J., et al., 1999, Dwarfs Cooler than "M": The Definition of Spectral Type "L" Using Discoveries from the 2 Micron All-Sky Survey (2MASS), ApJ, 519, 802
- Knude, J., 2002, Methods to Account for Interstellar Extinction, Ap&SS, 280, 97
- Komarova, V., 2006, Optical search for counterparts to isolated neutron stars at the 6m telescope of SAO RAS. In: Proceedings of the Conference: Isolated Neutron Stars: from the Interior to the Surface, London
- Konacki, M. & Wolszczan, A., 2003, Masses and Orbital Inclinations of Planets in the PSR B1257+12 System, ApJ, 591, L147
- Kulkarni, S. R. & van Kerkwijk, M. H., 1998, Optical Observations of the Isolated Neutron Star RX J0720.4-3125, ApJ, 507, L49
- Kürster, M. & Hasinger, G., 1993, ROSAT AMCS Status Report Boresighting re-analysis, MPE Technical Note TN-ROS-ME-ZA00/30 Kürster and Hasinger1993b
- Lallement, R., Welsh, B. Y., Vergely, J. L., Crifo, F., & Sfeir, D., 2003, 3D mapping of the dense interstellar gas around the Local Bubble, A&A, 411, 447
- Lazzati, D., Campana, S., Rosati, P., Panzera, M. R., & Tagliaferri, G., 1999, The Brera Multiscale Wavelet ROSAT HRI Source Catalog. I. The Algorithm, ApJ, 524, 414
- Leggett, S. K., Golimowski, D. A., Fan, X., et al., 2002, Infrared Photometry of Late-M, L, and T Dwarfs, ApJ, 564, 452
- Lorimer, D. R., 2004, The Galactic Population and Birth Rate of Radio Pulsars. In: F. Camilo and B. M. Gaensler (eds.), pp 105-+
- Lorimer, D. R., 2005, Binary and Millisecond Pulsars, Living Reviews in Relativity, 8, 7
- Lorimer, D. R. & Kramer, M., 2004, *Handbook of Pulsar Astronomy*, Cambridge observing handbooks for research astronomers, Vol. 4., Cambridge University Press, 2004
- Lyne, A. G. & Graham-Smith, F., 2005, Pulsar Astronomy, ISBN 0521839548. Cambridge University Press, 2005.

- Maccacaro, T., Gioia, I. M., Wolter, A., Zamorani, G., & Stocke, J. T., 1988, The X-ray spectra of the extragalactic sources in the Einstein extended medium sensitivity survey, ApJ, 326, 680
- Magnani, L., Blitz, L., & Mundy, L., 1985, Molecular gas at high Galactic latitudes, ApJ, 295, 402
- Malofeev, V. M. & Malov, O. I., 1997, Detection of Geminga as a radio pulsar., Nature, 389, 697
- Malofeev, V. M., Malov, O. I., Teplykh, D. A., et al., 2006, Discovery of radio emission from X-ray pulsar XDINS 1RXS J214303.7 +065419+06, The Astronomer's Telegram, 798, 1
- Malofeev, V. M., Malov, O. I., Teplykh, D. A., Tyul'Bashev, S. A., & Tyul'Basheva, G. E., 2005, Radio Emission from Two Anomalous X-ray Pulsars, Astronomy Reports, 49, 242
- Manchester, R. N., Hobbs, G. B., Teoh, A., & Hobbs, M., 2005, The Australia Telescope National Facility Pulsar Catalogue, AJ, 129, 1993
- Manchester, R. N., Lyne, A. G., D'Amico, N., et al., 1996, The Parkes southern pulsar survey I. Observing and data analysis systems and initial results., MNRAS, 279, 1235
- Marshall, D. J., Robin, A. C., Reylé, C., Schultheis, M., & Picaud, S., 2006, Modelling the Galactic interstellar extinction distribution in three dimensions, A&A, 453, 635
- Marshall, H. L. & Schulz, N. S., 2002, Using the High-Resolution X-Ray Spectrum of PSR B0656+14 to Constrain the Chemical Composition of the Neutron Star Atmosphere, ApJ, 574, 377
- Mathis, J. S., Rumpl, W., & Nordsieck, K. H., 1977, The size distribution of interstellar grains, ApJ, 217, 425
- McLaughlin, M. A., Lyne, A. G., Lorimer, D. R., et al., 2006, Transient radio bursts from rotating neutron stars, Nature, 439, 817
- Meidinger, N., Andritschke, R., Hälker, O., et al., 2006, Systematic testing and results of x-ray CCDs developed for eROSITA and other applications. In: High Energy, Optical, and Infrared Detectors for Astronomy II. Edited by Dorn, David A.; Holland, Andrew D.. Proceedings of the SPIE, Volume 6276, pp. (2006).
- Mel'nik, A. M. & Efremov, Y. N., 1995, A new list of OB associations in our galaxy, Astronomy Letters, 21, 10
- Meyer, D. M., Cardelli, J. A., & Sofia, U. J., 1997, The Abundance of Interstellar Nitrogen, ApJ, 490, L103+
- Meyer, D. M., Jura, M., & Cardelli, J. A., 1998, The Definitive Abundance of Interstellar Oxygen, ApJ, 493, 222
- Michel, F. C., 1991, *Theory of neutron star magnetospheres*, Chicago, IL, University of Chicago Press, 1991, 533 p.
- Mignani, R. P., Manchester, R. N., & Pavlov, G. G., 2003, Search for the Optical Counterpart of the Nearby Pulsar PSR J0108-1431, ApJ, 582, 978
- Monet, D. G., Levine, S. E., Canzian, B., et al., 2003, The USNO-B Catalog, AJ, 125, 984

- Moorwood, A., Cuby, J.-G., Biereichel, P., et al., 1998, ISAAC sees first light at the VLT., The Messenger, 94, 7
- Morrison, R. & McCammon, D., 1983, Interstellar photoelectric absorption cross sections, 0.03-10 keV, ApJ, 270, 119
- Motch, C., Haberl, F., Zickgraf, F.-J., Hasinger, G., & Schwope, A. D., 1999, The isolated neutron star candidate RX J1605.3+3249, A&A, 351, 177
- Motch, C., Pires, A. M., Haberl, F., & Schwope, A., 2006, Measuring proper motions of isolated neutron stars with Chandra. In: Proceedings of the Conference: Isolated Neutron Stars: from the Interior to the Surface, London, astro-ph/0608589
- Motch, C., Sekiguchi, K., Haberl, F., et al., 2005, The proper motion of the isolated neutron star ¡ASTROBJ¿RX J1605.3+3249¡/ASTROBJ¿, A&A, 429, 257
- Motch, C., Zavlin, V. E., & Haberl, F., 2003, The proper motion and energy distribution of the isolated neutron star jASTROBJ¿RX J0720.4-3125j/ASTROBJ¿, A&A, 408, 323
- Mukai, K., 1993, PIMMS and Viewing: proposal preparation tools, Legacy, vol. 3, p.21-31, 3, 21
- Mushotzky, R., 2004, How are AGN Found?, pp 53–+, ASSL Vol. 308: Supermassive Black Holes in the Distant Universe
- Neuhäuser, R., 2001, The proper motion of the neutron star RXJ1856.5-3754 as measured by optical and X-ray imaging, Astronomische Nachrichten, 322, 3
- Neuhäuser, R., Thomas, H.-C., Danner, R., Peschke, S., & Walter, F. M., 1997, On the X-ray position and deep optical imaging of the neutron star candidate RX J1856.5-3754., A&A, 318, L43
- Neuhäuser, R. & Trümper, J. E., 1999, On the number of accreting and cooling isolated neutron stars detectable with the ROSAT All-Sky Survey, A&A, 343, 151
- Ostriker, J. P., Rees, M. J., & Silk, J., 1970, Some Observable Consequences of Accretion by Defunct Pulsars, Astrophys. Lett., 6, 179
- Paczynski, B., 1990, A test of the galactic origin of gamma-ray bursts, ApJ, 348, 485
- Paczynski, B., 1992, GB 790305 as a very strongly magnetized neutron star, Acta Astronomica, 42, 145
- Panzera, M. R., Campana, S., Covino, S., et al., 2003, The Brera Multi-scale Wavelet ROSAT HRI source catalogue, A&A, 399, 351
- Paresce, F., 1984, On the distribution of interstellar matter around the sun, AJ, 89, 1022
- Pavlov, G. G., Zavlin, V. E., Sanwal, D., Burwitz, V., & Garmire, G. P., 2001, The X-Ray Spectrum of the Vela Pulsar Resolved with the Chandra X-Ray Observatory, ApJ, 552, L129
- Perna, R., Narayan, R., Rybicki, G., Stella, L., & Treves, A., 2003, Bondi Accretion and the Problem of the Missing Isolated Neutron Stars, ApJ, 594, 936
- Pichardo, B., Martos, M., & Moreno, E., 2004, Models for the Gravitational Field of the Galactic Bar: An Application to Stellar Orbits in the Galactic Plane and Orbits of Some Globular Clusters, ApJ, 609, 144

- Piskunov, A. E., Kharchenko, N. V., Röser, S., Schilbach, E., & Scholz, R.-D., 2006, Revisiting the population of Galactic open clusters, A&A, 445, 545
- Podsiadlowski, P., 1995, *The Formation of Planet Pulsars*. In: A. S. Fruchter, M. Tavani, and D. C. Backer (eds.), pp 411–+
- Popov, S., Grigorian, H., Turolla, R., & Blaschke, D., 2006a, Population synthesis as a probe of neutron star thermal evolution, A&A, 448, 327
- Popov, S. B., Colpi, M., Prokhorov, M. E., Treves, A., & Turolla, R., 2000a, The LOG N-LOG S Distributions of Accreting and Cooling Isolated Neutron Stars, ApJ, 544, L53
- Popov, S. B., Colpi, M., Prokhorov, M. E., Treves, A., & Turolla, R., 2003, Young isolated neutron stars from the Gould Belt, A&A, 406, 111
- Popov, S. B., Colpi, M., Treves, A., et al., 2000b, The Neutron Star Census, ApJ, 530, 896
- Popov, S. B., Turolla, R., & Possenti, A., 2006b, A tale of two populations: rotating radio transients and X-ray dim isolated neutron stars, MNRAS, 369, L23
- Popov, S. B., Turolla, R., Prokhorov, M. E., Colpi, M., & Treves, A., 2005, Young Close-By Neutron Stars: The Gould Belt Vs. The Galactic Disc, Ap&SS, 299, 117
- Pöppel, W., 1997, The Gould Belt System and the Local Interstellar Medium, Fundamentals of Cosmic Physics, 18, 1
- Pöppel, W. G. L., 2001, *The Gould Belt System*. In: T. Montmerle and P. André (eds.), pp 667-+
- Predehl, P., Hasinger, G., Böhringer, H., et al., 2006, eROSITA. In: Space Telescopes and Instrumentation II: Ultraviolet to Gamma Ray. Edited by Turner, Martin J. L.; Hasinger, Günther. Proceedings of the SPIE, Volume 6266, pp. (2006).
- Predehl, P. & Schmitt, J. H. M. M., 1995, X-raying the interstellar medium: ROSAT observations of dust scattering halos., A&A, 293, 889
- Richards, G. T., Fan, X., Newberg, H. J., et al., 2002, Spectroscopic Target Selection in the Sloan Digital Sky Survey: The Quasar Sample, AJ, 123, 2945
- ROSAT Scientific Team, 2000a, ROSAT HRI Pointed Observations (1RXH) (ROSAT Team, 2000), VizieR Online Data Catalog, 9028, 0
- ROSAT Scientific Team, 2000b, Second ROSAT PSPC Catalog (ROSAT, 2000), VizieR Online Data Catalog, 9030, 0
- Rutledge, R. E., Fox, D. W., Bogosavljevic, M., & Mahabal, A., 2003, A Limit on the Number of Isolated Neutron Stars Detected in the ROSAT Bright Source Catalogue, ApJ, 598, 458
- Sasaki, M., Haberl, F., & Pietsch, W., 2000, ROSAT HRI catalogue of X-ray sources in the SMC region, A&AS, 147, 75
- Schmidt, A., 2004, Tiefe Infrarot-Aufnahmen von Begleiterkandidaten naher Neutronensterne, Bakkalaureus Abschlussarbeit, Friedrich-Schiller-Universität Jena
- Schwope, A., Hambaryan, V., Haberl, F., & Motch, C., 2006, A second absorption feature in the X-ray spectrum of RBS1223. In: Proceedings of the Conference: Isolated Neutron Stars: from the Interior to the Surface, London

- Schwope, A. D., Hasinger, G., Schwarz, R., Haberl, F., & Schmidt, M., 1999, The isolated neutron star candidate RBS1223 (1RXS J130848.6+212708), A&A, 341, L51
- Sfeir, D. M., Lallement, R., Crifo, F., & Welsh, B. Y., 1999, Mapping the contours of the Local bubble: preliminary results, A&A, 346, 785
- Sigurdsson, S., Richer, H. B., Hansen, B. M., Stairs, I. H., & Thorsett, S. E., 2003, A Young White Dwarf Companion to Pulsar B1620-26: Evidence for Early Planet Formation, Science, 301, 193
- Sigurdsson, S. & Thorsett, S. E., 2005, Update on Pulsar B1620-26 in M4: Observations, Models, and Implications. In: F. A. Rasio and I. H. Stairs (eds.), pp 213-+
- Skrutskie, M. F., Cutri, R. M., Stiening, R., et al., 2006, The Two Micron All Sky Survey (2MASS), AJ, 131, 1163
- Snow, T. P. & Witt, A. N., 1996, Interstellar Depletions Updated: Where All the Atoms Went, ApJ, 468, L65+
- Stocke, J. T., Morris, S. L., Gioia, I. M., et al., 1991, The Einstein Observatory Extended Medium-Sensitivity Survey. II The optical identifications, ApJS, 76, 813
- Stoughton, C., Lupton, R. H., Bernardi, M., et al., 2002, Sloan Digital Sky Survey: Early Data Release, AJ, 123, 485
- Tammann, G. A., Loeffler, W., & Schroeder, A., 1994, The Galactic supernova rate, ApJS, 92, 487
- Tauris, T. M. & Manchester, R. N., 1998, On the Evolution of Pulsar Beams, MNRAS, 298, 625
- Taylor, J. H., Manchester, R. N., & Lyne, A. G., 1993, Catalog of 558 pulsars, ApJS, 88, 529
- Timmes, F. X., Woosley, S. E., & Weaver, T. A., 1996, The Neutron Star and Black Hole Initial Mass Function, ApJ, 457, 834
- Tody, D., 1986, The IRAF Data Reduction and Analysis System. In: D. L. Crawford (ed.), pp 733-+
- Tody, D., 1993, IRAF in the Nineties. In: R. J. Hanisch, R. J. V. Brissenden, and J. Barnes (eds.), pp 173-+
- Torra, J., Fernández, D., & Figueras, F., 2000, Kinematics of young stars. I. Local irregularities, A&A, 359, 82
- Toscano, M., Sandhu, J. S., Bailes, M., et al., 1999, Millisecond pulsar velocities, MNRAS, 307, 925
- Treves, A., Turolla, R., Zane, S., & Colpi, M., 2000, Isolated Neutron Stars: Accretors and Coolers, PASP, 112, 297
- Trümper, J., 1992, ROSAT A new look at the X-ray sky (The 1991 Grubb-Parsons Lecture), QJRAS, 33, 165
- Trümper, J., 1993, ROSAT A new look at the X-ray sky, Science, 260, 1769

- Trümper, J., 2006, Radiation radii of neutron stars. In: 363rd Hereaus Seminar on: Neutron Stars and Pulsars About 40 years after the discovery
- Trümper, J. E., 2005, Observations of cooling neutron stars, arXiv:astro-ph/0502457
- Trümper, J. E., Burwitz, V., Haberl, F., & Zavlin, V. E., 2004, The puzzles of RX J1856.5-3754: neutron star or quark star?, Nuclear Physics B Proceedings Supplements, 132, 560
- Turbiner, A. N., 2006, *Molecular systems in a strong magnetic field*. In: Proceedings of the Conference: Isolated Neutron Stars: from the Interior to the Surface, London
- van Adelsberg, M., Lai, D., Potekhin, A. Y., & Arras, P., 2005, Radiation from Condensed Surface of Magnetic Neutron Stars, ApJ, 628, 902
- van Kerkwijk, M. H. & Kaplan, D. L., 2006, Isolated neutron stars: Magnetic fields, distances, and spectra, astro-ph/0607320
- van Kerkwijk, M. H., Kaplan, D. L., Durant, M., Kulkarni, S. R., & Paerels, F., 2004, A Strong, Broad Absorption Feature in the X-Ray Spectrum of the Nearby Neutron Star RX J1605.3+3249, ApJ, 608, 432
- van Kerkwijk, M. H. & Kulkarni, S. R., 2001, Optical spectroscopy and photometry of the neutron star ¡ASTROBJ¿RX J1856.5-3754¡/ASTROBJ¿, A&A, 378, 986
- van Paradijs, J., Taam, R. E., & van den Heuvel, E. P. J., 1995, On the nature of the 'anomalous' 6-s X-ray pulsars, A&A, 299, L41+
- Vergely, J.-L., Freire Ferrero, R., Siebert, A., & Valette, B., 2001, NaI and HI 3-D density distribution in the solar neighbourhood, A&A, 366, 1016
- Verner, D. A. & Yakovlev, D. G., 1995, Analytic FITS for partial photoionization cross sections., A&AS, 109, 125
- Verner, D. A., Yakovlev, D. G., Band, I. M., & Trzhaskovskaya, M. B., 1993, Subshell Photoionization Cross Sections and Ionization Energies of Atoms and Ions from He to Zn, Atomic Data and Nuclear Data Tables, 55, 233
- Voges, W., Aschenbach, B., Boller, T., et al., 1999, The ROSAT all-sky survey bright source catalogue, A&A, 349, 389
- Voges, W., Aschenbach, B., Boller, T., et al., 2000, ROSAT all-sky survey faint source catalogue., IAU Circ., 7432, 1
- Walter, F., 2006, *The Trigonometric Parallax of Geminga. II. Consequences*. In: Proceedings of the Conference: Isolated Neutron Stars: from the Interior to the Surface, London
- Walter, F. M., 2001, The Proper Motion, Parallax, and Origin of the Isolated Neutron Star RX J185635-3754, ApJ, 549, 433
- Walter, F. M. & Lattimer, J. M., 2002, A Revised Parallax and Its Implications for RX J185635-3754, ApJ, 576, L145
- Walter, F. M. & Matthews, L. D., 1997, The optical counterpart of the isolated neutron star RX J185635-3754., Nature, 389, 358
- Welty, D. E., Hobbs, L. M., & Kulkarni, V. P., 1994, A high-resolution survey of interstellar NA I D1 lines, ApJ, 436, 152

- White, R. L., Becker, R. H., Helfand, D. J., & Gregg, M. D., 1997, A Catalog of 1.4 GHz Radio Sources from the FIRST Survey, ApJ, 475, 479
- Wilms, J., Allen, A., & McCray, R., 2000, On the Absorption of X-Rays in the Interstellar Medium, ApJ, 542, 914
- Wolszczan, 2005, Scientists Announce Smallest Extra-Solar Planet Yet Discovered and Find Outer Limits of the Pulsar Planetary System http://www.science.psu.edu/alert/wolszczan2 - 2005.htm
- Wolszczan, A. & Frail, D. A., 1992, A planetary system around the millisecond pulsar PSR1257 + 12, Nature, 355, 145
- Woods, P. M. & Thompson, C., 2004, Soft Gamma Repeaters and Anomalous X-ray Pulsars: Magnetar Candidates, astro-ph/0406133
- Woosley, S. E., Heger, A., & Weaver, T. A., 2002, The evolution and explosion of massive stars, Reviews of Modern Physics, 74, 1015
- York, D. G., Adelman, J., Anderson, Jr., J. E., et al., 2000, The Sloan Digital Sky Survey: Technical Summary, AJ, 120, 1579
- Zampieri, L., Campana, S., Turolla, R., et al., 2001, 1RXS J214303.7+065419/RBS 1774: A new Isolated Neutron Star candidate, A&A, 378, L5
- Zane, S., Cropper, M., Turolla, R., et al., 2005, XMM-Newton Detection of Pulsations and a Spectral Feature in the X-Ray Emission of the Isolated Neutron Star 1RXS J214303.7+065419/RBS 1774, ApJ, 627, 397
- Zane, S. & Turolla, R., 2006, Unveiling the thermal and magnetic map of neutron star surfaces though their X-ray emission: method and light-curve analysis, MNRAS, 366, 727
- Zane, S., Turolla, R., Zampieri, L., Colpi, M., & Treves, A., 1995, Old Isolated Accreting Neutron Stars: Contribution to the Soft X-Ray Background in the 0.5–2 keV Band, ApJ, 451, 739
- Zickgraf, F.-J., Engels, D., Hagen, H.-J., Reimers, D., & Voges, W., 2003, The Hamburg/RASS Catalogue of optical identifications. Northern high-galactic latitude ROSAT Bright Source Catalogue X-ray sources, A&A, 406, 535

### Appendix A

## Telescopes, instruments and data sources

#### A.1 X-ray telescopes

#### A.1.1 ROSAT

(from the German name RÖntgen SATellit) was a space-borne soft X-ray observatory sensitive in the energy range from 0.1 to 2.4 keV. The ROSAT mission started on 1 June 1990 and ended 12 February 1999. Four Wolter-type I mirror systems were concentrically assembled to obtain images by grazing-incidence of the X-ray photons. The angular resolution achieved by the mirror system is  $\leq 5''$  considering the half energy width of detected sources. ROSAT was equipped with two types of detectors mounted in the focal plane: two Position Sensitive Proportional Counters (PSPCs) and one High Resolution Imager (HRI). Only one instrument was usable at a given time. ROSAT was a collaborative project between Germany, The United States of America (USA) and the United Kingdom (UK). An overview about the ROSAT mission was given by Trümper (1992) and Trümper (1993), see also MPE webpages<sup>1</sup> for more information.

#### Position Sensitive Proportional Counter (PSPC)

The PSPC was a multi-wire proportional counter developed at the Max Planck Institut für extraterrestrische Physik, Germany. In order to determine positions the front and the back layer of the cathode wires were rotated by 90°. The counter gas was a mixture of argon, xenon and methane. The energy resolution was limited by the Poisson statistics of created ion pairs in the gas. The required energy for the creation of ion pairs was 30 eV. The PSPC had a field of view with radius 1°. The entrance window with a Polypropylene foil was supported by an eight spoke structure with a central ring. To ensure equal illumination of the detector in case of pointed observation the telescope was operated in

<sup>&</sup>lt;sup>1</sup>http://wave.xray.mpe.mpg.de/rosat/doc/ruh

wobble mode (slow back and forth motion).

The PSPC was used for the ROSAT All Sky Survey (RASS) documented in the Bright and Faint RASS source catalogues (Voges et al., 1999, 2000). There were also pointed observations with the PSPC resulting, for example, in the 2RXP catalogue (ROSAT Scientific Team, 2000b). The 2RXP catalogue covers around 17.3% of the sky. For more information on the PSPC we refer to the wepages at MPE<sup>1</sup>.

#### High Resolution Imager (HRI)

The HRI was a multichannel plate detector developed at the Goddard Space Flight Center. The HRI had a field of view with radius 19′, no intrinsic energy resolution, but good spatial resolution of around 2″ (neglecting the systematic error of the whole satellite). The HRI was used for pointed observations resulting, for example, in the 1RXH catalogue (ROSAT Scientific Team, 2000a). The 1RXH catalogue covers around 1.9% of the sky. For more information on the HRI we refer to the HRI calibration report<sup>2</sup>.

#### A.1.2 XMM-Newton

The XMM-Newton satellite of the European Space Agency (ESA) was launched on 10 December 1999. XMM-Newton is a multi-nation collaborative project with instruments developed together by the UK, Italy, France, Germany, the Netherlands, and the USA. The satellite is controlled by the European Space Operations Centre, Darmstadt in Germany. Further operations centers are the XMM-Newton Science Operations Centre situated at VILSPA in Villafranca in Spain, and the XMM-Newton Survey Science Centre at Leicester University in the United Kingdom. XMM-Newton consists of three barrelshaped Mirror Modules, each containing 58 Wolter-type I wafer-thin concentric mirrors. XMM-Newton has a collecting area of 4300 cm<sup>2</sup> at 1.5 keV, the largest collecting area of all X-ray satellites until now. In principle XMM-Newton is sensitive to X-ray energies from 0.1 keV to 12 keV. The three main scientific instruments on board XMM-Newton are the three European Photon Imaging Cameras (EPIC), the two Reflection Grating Spectrometers (RGS) and the Optical Monitor (OM). In addition, XMM-Newton is equipped with a particle detector, the EPIC Radiation Monitor System (ERMS). Below we give some details about the EPIC instrument, which is considered in this thesis. More information on the XMM-Newton mission and the instruments can be found on ESA's webpages<sup>3</sup>.

#### The European Photon Imaging Cameras (EPIC)

The EPIC instrument consists of two EPIC-MOS (Metal Oxide Semi-conductor) CCD

<sup>&</sup>lt;sup>2</sup>http://hea-www.harvard.edu/rosat/hricalrep.html

<sup>&</sup>lt;sup>3</sup>http://sci.esa.int/science-e/www/area/index.cfm?fareaid=23

http://sci.esa.int/science-e/www/object/index.cfm?fobjectid=31281&fbodylongid=773

(charge-coupled devices) cameras, developed and built at the University of Leicester's Space Research Centre, and the EPIC-pn camera which uses a new type of CCD (pn) developed by the Max Planck Institut für extraterrestische Physik (MPE) in Garching, Germany. EPIC covers the whole field of view of the telescope, which is 30′. It detects X-ray photons in the energy range from 0.15 to 15 keV with moderate spectral ( $E/\Delta E \approx 20$ -50) and angular resolution (the point spread function has a full width of half maximum of 6″).

Each EPIC-MOS CCD consists of seven silicon chips, each made up of a matrix of  $600 \times 600$  pixels. The readout time for one CCD is a couple of seconds. The MOS CCDs have a good energy resolution at soft X-rays. Their response to hard X-rays is less good due to the thin 40-micron sensitive depth of silicon. For further information on EPIC-MOS we refer to the webpages of the University of Leicester<sup>1</sup>.

The EPIC-pn instrument consists of twelve silicon chips, each made up of a matrix of  $64 \times 189$  pixels. The silicon wafer manufactured with extreme precision is very thick (300 micron). The double-sided processed silicon detectors are illuminated from the rear sides (in contrast to the MOS CCDs), which do not have insensitive layers or coatings. The X-ray detection efficiency is extremely high and homogeneous from the very low to the highest XMM-Newton energies up to 12 keV. EPIC-pn readout time is only 80 ms for one picture or frame, in time resolution only 40 ms. The EPIC-pn instrument is very stable on time scales of years, a difference to the MOS cameras (Haberl, 2006), see also XMM calibration webpages<sup>2</sup>. More information can be found at MPE's EPIC-pn webpages<sup>3</sup>.

#### A.1.3 Chandra

The US-american Chandra X-ray Observatory was formerly known as AXAF, the Advanced X-ray Astrophysics Facility, but was renamed by the National Space Administration (NASA) in December, 1998. The X-ray satellite was started in 1999 by NASA and is controlled by the Jet Propulsion Laboratory and the Operations Control at the Chandra X-ray Center (CXC) in Cambridge, MA. The mirror system of Chandra consists of four nested Wolter-type I telescopes. Chandra is equipped with two focal plane science instruments and two grating instruments which can be flipped into the path of the X-rays just behind the mirrors. The High Resolution Camera (HRC), a microchannel plate detector, and the Advanced CCD Imaging Spectrometer (ACIS), an array of CCDs, are situated in the focal plane. The two transmission grating spectrometers are the High Energy Transmission Grating Spectrometer (HETGS) and the Low Energy Transmission Grating Spectrometer (LETG). Comparing to XMM-Newton it has less collecting area and is therefore less sensitive. Chandra has a superb spatial resolution which is usually better than 0.6", nearly a factor 10 better than XMM. XMM and Chandra are good comple-

<sup>&</sup>lt;sup>1</sup>http://www.src.le.ac.uk/projects/xmm/

 $<sup>^2</sup> http://xmm.vilspa.esa.es/external/xmm\_user\_support/usersgroup/20060518/epic\_cal.pdf$ 

<sup>&</sup>lt;sup>3</sup>http://wave.xray.mpe.mpg.de/xmm/epic/doc

ments to each other. More information on the Chandra observatory and its instruments can be found on NASA's Chandra webpages  $^{1}$   $^{2}$ 

<sup>&</sup>lt;sup>2</sup>http://cxc.harvard.edu/cal/

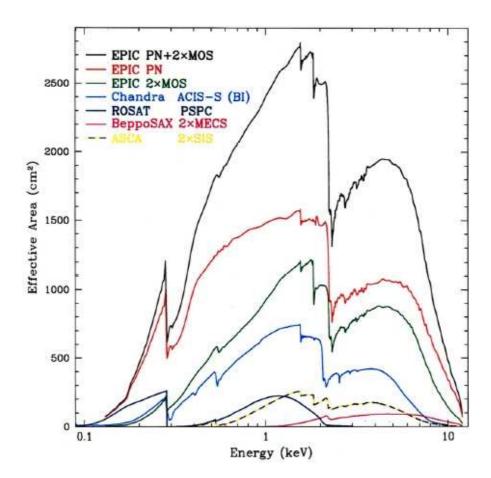


Figure A.1: Effective areas of different X-ray satellites

Shown are the effective areas (corresponding to the sensitivity) over energy in keV for the following instruments: ROSAT PSPC, XMM-Newton EPIC MOS and pn cameras individually and together, Chandra ACIS in S-mode with two backside illuminated CCDs, and two other (past) intruments (ASCA and BeppoSAX). At soft X-ray energies (< 1 keV) XMM EPIC-pn is the most sensitive individual instrument.

 $<sup>^{1}</sup> http://cxc.harvard.edu/cdo/about\_chandra/overview\_cxo.html$ 

#### A.2 Optical and Near Infrared Telescopes

#### A.2.1 Very Large Telescope (VLT)

The European Southern Observatory (ESO) operates the Very Large Telescope (VLT) at Cerro Paranal, a 2,635-m high mountain in the Atacama desert in Chile. The VLT operates at wavelengths from the near-ultraviolet to the mid-infrared. The VLT consists of an array of four 8-meter telescopes which can work independently or in combined mode. Each utility telescope (UT) is of Ritchey-Chrétien-type and applies active optics. Different instruments are mounted on the two Nasmyth foci as well as on the Cassegrain focus of each UT. More information on the VLT and its instrument can be found on ESO's webpages<sup>1</sup>.

#### Infrared Spectrometer And Array Camera (ISAAC)

ISAAC (Moorwood et al., 1998) operates at Infrared wavelengths of 1 to 5  $\mu$ m as an imager and spectrograph. It is mounted on the Nasmyth B focus of UT1. It has two arms, one equipped with the Hawaii Rockwell array, and the other with the Aladdin array from Santa Barbara Research Center. The Hawaii detector works at near infrared (NIR) wavelengths (1 - 2.5  $\mu$ m). The Aladdin detector operates at the mid infrared (3 - 5  $\mu$ m) and also at NIR. In this thesis the Hawaii array in imaging mode was used. The Hawaii array is based on mercury cadmium telluride CCDs. The Hawaii detector in imaging mode has a size of 1024 pixels  $\times$  1024 pixels, covering 152"  $\times$  152" with a pixel scale of 0.1484". Individual exposures can last 10 s to 12 s in case of observations in the H-band (1.65  $\mu$ m). For further information we refer to ESO's ISAAC webpages<sup>2</sup>.

#### FOcal Reducer and low dispersion Spectrograph (FORS)

FORS (Appenzeller et al., 1998) operates at the visual and in the near ultraviolet, from 330 nm to 1100 nm. There are two FORS instruments - FORS1 and FORS2. In this thesis data obtained with FORS1 was used. The FORS1 detector is a Tektronix 2048 pixels  $\times$  2048 pixels CCD with a pixel size of 24  $\mu$ mm, anti-reflection coated and backside illuminated. Two spatial resolutions and hence field sizes can be selected by exchange of the collimators. In case of using the standard resolution collimator for the FORS1 the field of view is  $6.8' \times 6.8'$  and the pixel scale is 0.2''. With the high resolution collimator the field of view is  $3.4' \times 3.4'$  and the pixel scale is 0.1''. For further information we refer to ESO's FORS webpages<sup>3</sup>.

<sup>&</sup>lt;sup>1</sup>http://www.eso.org/projects/vlt/unit-tel/,http://eso.org/instruments/#pao

<sup>&</sup>lt;sup>2</sup>http://www.eso.org/instruments/isaac/doc/

<sup>&</sup>lt;sup>3</sup>http://www.eso.org/instruments/fors/index.html

#### A.2.2 New Technology Telescope (NTT)

ESO's NTT is a 3.58 m Ritchey-Chrétien-type telescope situated on La Silla at 2375 m in the Atacama dersert, Chile. The NTT uses active optics and operates at visible and NIR wavelengths. Three different instruments are mounted on the two Nasmyth foci, shortly summarized below. For further information on the NTT see ESO's webpages<sup>1</sup>.

Son OF ISAAC (SOFI) SOFI is mounted on Nasmyth A focus. It is very similar to ISAAC at the VLT (Moorwood et al., 1998) and capable to do NIR imaging, spectroscopy and polarimetry. The SOFI intrument is also based on a Hawaii detector 1024 pixels  $\times$  1024 pixels CCD made of mercury cadmium telluride by Rockwell Scientific. In this thesis the small field imaging mode was used. The field of view is  $2.46' \times 2.46'$  with a pixel scale of 0.144'' in the small field imaging mode. Broad and narrow band filters in the wavelength range of  $0.9~\mu m$  to  $2.5~\mu m$  can be used. For further information we refer to ESO's SOFI webpages<sup>2</sup>.

Superb-Seeing Imager (SuSI2) SuSI2 is a direct optical imaging CCD camera mounted at the on the Nasmyth A focus. The camera (D'Odorico et al., 1998) consists of two CCDs, each  $2000 \times 4000$  pixels of  $15\mu$ m size. The whole field of view is  $5.5' \times 5.5'$  and the pixel scale is 0.0805''. Filters are provided for wavelengths from 360 nm to 840 nm. For further information we refer to ESO's SuSI webpages<sup>3</sup>.

**ESO Multi-Mode Instrument** (EMMI) The EMMI intrument (Dekker et al., 1986) is mounted on Nasmyth B focus and is used for observations in the visible wavelengths (between 300 nm and 1000 nm). Wide-field imaging and spectroscopy are possible operation modes. EMMI works with three thin, back-illuminated, anti-reflection coated scientific CCD cameras; two of them, which are arranged in a mosaic, in the red arm and one in the blue arm. Each CCD of the red arm are 2048 pixels  $\times$  4096 pixels with a size of 15 $\mu$ m, and a pixel scale of 0.166". The CCD in the blue arm has 1024 pixels  $\times$  1024 pixels with a size of 24 $\mu$ m, and a pixel scale of 0.37". For further information we refer to ESO's EMMI webpages<sup>4</sup>.

<sup>&</sup>lt;sup>1</sup>http://www.ls.eso.org/lasilla/sciops/ntt/NTT\_tech.html

<sup>&</sup>lt;sup>2</sup>http://www.ls.eso.org/lasilla/sciops/ntt/sofi/

<sup>&</sup>lt;sup>3</sup>http://www.ls.eso.org/lasilla/sciops/ntt/susi/index.html

<sup>&</sup>lt;sup>4</sup>http://www.ls.eso.org/lasilla/sciops/ntt/emmi/index.html

#### A.3 Data bases

#### A.3.1 The Sloan Digital Sky Survey (SDSS)

The SDSS is an imaging an spectroscopic survey using the dedicated 2.5-meter Ritchey-Chretien telescope on Apache Point, New Mexico. SDSS started in 2000 and has completed its first phase of operations SDSS-I in June, 2005. Over the course of five years serveral incremental data releases have been published. The last one is the data release DR5 (June 2006). SDSS-I imaged more than 8000 square degrees of the sky in the five bandpasses u (355.1 nm), g (468.6 nm), r (616.5 nm), i (748.1 nm), z (893.1 nm) detecting nearly 200 million celestial objects, and it measured spectra of more than 675000 galaxies, 90000 quasars, and 185000 stars. The 95% imaging completeness limit for stars is 22.0, 22.2, 22.2, 21.3, and 20.5 mag for u, g, r, i, and z respectively (SDSS DR5 wepages<sup>1</sup>). The photometric calibration is reproducible to 5%, 3%, 3%, 3%, and 5% respectively (Stoughton et al., 2002). The astrometry is thought to be better than 0.1" per coordinate (SDSS DR5 wepages). For more information on technical aspects we refer to York et al. (2000), for a description of the released data to Stoughton et al. (2002), and for the current data relase 5 (DR5) to the SDSS webpages<sup>2</sup>  $^3$ .

#### A.3.2 Further data bases

#### US Naval Observatory catalogues

There are several subsequent USNO all-sky catalogues done by scanning photometric plates. The latest, USNO-B (Monet et al., 2003) presents positions, proper motions, magnitudes in various optical passbands and star/galaxy estimators for  $\approx 1 \times 10^9$  objects obtained from scans of 7435 Schmidt plates taken for the various sky surveys during the last 50 years. USNO-B1.0 is believed to be complete down to V=21 mag with 0.3 mag photometric accuracy. USNO-B1.0 has an astrometric accuracy of 0.2" at J2000. The precursor of USNO-B1.0 was USNO-A2. More information on the USNO can be found at the USNO webpages<sup>4</sup>, USNO-B1.0 can be queried e.g. at VizieR<sup>5</sup>.

#### The Two Micron All Sky Survey (2MASS)

2MASS (Skrutskie et al., 2006) imaged 99.998% of the celestial sphere in the near-infrared J (1.25  $\mu$ m), H (1.65  $\mu$ m), and Ks (2.16  $\mu$ m) bandpasses. The observations were done using two dedicated 1.3 m diameter telescopes located at Mount Hopkins, Arizona, and Cerro Tololo, Chile. The  $10\sigma$  point-source detection level yielded is better than 15.8, 15.1,

<sup>&</sup>lt;sup>1</sup>http://www.sdss.org/dr5/index.html

<sup>&</sup>lt;sup>2</sup>http://www.sdss.org

<sup>&</sup>lt;sup>3</sup>http://www.sdss.org/dr5

<sup>&</sup>lt;sup>4</sup>http://www.nofs.navy.mil/data/fchpix/

<sup>&</sup>lt;sup>5</sup>http://vizier.u-strasbg.fr/viz-bin/Cat?I/284

and 14.3 mag at the J, H, and Ks bands, respectively. The  $1\sigma$  photometric uncertainty of bright source is below 0.03 mag and the astrometric accuracy is of the order of 100 mas (Skrutskie et al., 2006). For further information we refer to the 2MASS webpages<sup>1</sup>. In this thesis we applied the 2MASS Point Source Catalogue (PSC) which can be queried e.g. at VizieR<sup>2</sup>.

#### Infrared Astronomical Satellite (IRAS) point source catalogue (PSC)

IRAS observed at 12, 25, 60, and 100  $\mu$ m and is complete to about 0.4, 0.5, 0.6, and 1.0 Jy repectively. Typical position uncertainties are about 2" to 6" in-scan and about 8" to 16" cross-scan. The IRAS PSC can be queried e.g. at VizieR<sup>3</sup>, more information can be found at the IRAS webpages<sup>4</sup>.

#### NRAO Very Large Array (VLA) Sky Survey (NVSS)

NVSS (Condon et al., 1998) is radio survey at 1.4 GHz, and it covers the sky north of  $\delta = -40^{\circ}$  (82% of the celestial sphere). The VLA images all have 45" full width of half maximum resolution and nearly uniform sensitivity. The uncertainties in right ascension and declination vary from  $\leq 1$ " for the roughly  $4 \times 10^5$  sources stronger than 15 mJy to 7" at the survey limit 2.5mJy. Besides images at the NVSS website<sup>5</sup> there is also a source catalogue which can be queried e.g. at VizieR<sup>6</sup>.

#### Faint Images of the Radio Sky at Twenty centimeters (FIRST)

FIRST (White et al., 1997) is also a radio survey carried out by the VLA at a frequency of 1.4 GHz covering 10000 square degrees of the North and South Galactic Caps. The achieved sensitivity is about 1 mJy at an angular resolution of about 5". For further information we refer to the FIRST webpages<sup>7</sup>.

<sup>&</sup>lt;sup>1</sup>http://www.ipac.caltech.edu/2mass/

<sup>&</sup>lt;sup>2</sup>http://vizier.u-strasbg.fr/viz-bin/Cat?II/246

<sup>&</sup>lt;sup>3</sup>http://vizier.u-strasbg.fr/viz-bin/Cat?II/125

<sup>&</sup>lt;sup>4</sup>http://irsa.ipac.caltech.edu/IRASdocs/iras.html

<sup>&</sup>lt;sup>5</sup>http://www.cv.nrao.edu/nvss/

<sup>&</sup>lt;sup>6</sup>http://vizier.u-strasbg.fr/viz-bin/Cat?VIII/65

<sup>&</sup>lt;sup>7</sup>http://sundog.stsci.edu/

# Appendix B Additional figures to Chapter 2

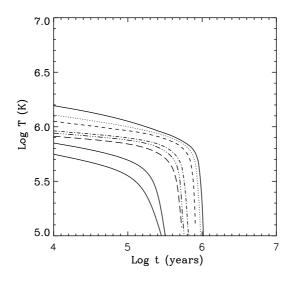


Figure B.1: Cooling curves for model I by Popov et al. (2006a)

The cooling curves (surface temperature over time from birth) are plotted for (from top to bottom) 1.1, 1.25, 1.32, 1.4, 1.48, 1.6, 1.7, 1.76  $M_{\odot}$  neutron stars. They are based on claculations by Blaschke et al. (2004) for hadronic matter only.

See Popov et al. (2006a) for more detailed description, e.g. their Table 1.

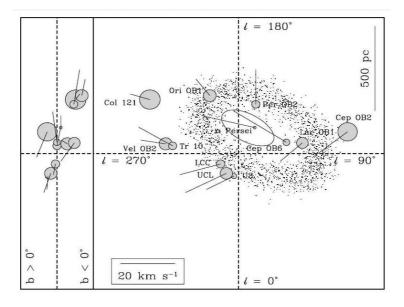


Figure B.2: Locations of the OB associations by de Zeeuw et al. (1999)

The locations are projected onto the Galactic plane (right) and a corresponding cross section (left). The grey circles indicate the physical dimensions as obtained from the angular dimensions and mean distances, on the same scale. The lines represent the streaming motions, derived from the average proper motions, mean distances and median radial velocities of the secure members. The ellipse around the  $\alpha$  Persei cluster indicates the Cas A-Tau association. The small dots schematically represent a model of the Gould Belt. This figure is taken from de Zeeuw et al. (1999) (their Fig. 29).

## Appendix C

## Additional information about the Magnificent Seven

Table C.1: X-ray and optical properties of the Magnificent Seven

Listed for each M7 member are the name, the temperature kT derived from spectral fits for the X-ray emission region, the periods found in the X-ray spectra, the amplitude of the pulsed fraction of the X-ray flux, the magnitudes of optical counterparts or limits, the proper motion PM and the corresponding references.

This table is taken from Haberl (2006).

| Object            | kT    | Period | Amplitude | Optical            | PM         | References  |
|-------------------|-------|--------|-----------|--------------------|------------|-------------|
|                   | [eV]  | [s]    | [%]       | [mag]              | [mas/year] |             |
| RX J0420.0-5022   | 44    | 3.45   | 13        | B = 26.6           |            | 1           |
| RXJ0720.4 – 3125  | 85-95 | 8.39   | 8-15      | B = 26.6           | 97         | 2,3,4,5,6   |
| RXJ0806.4-4123    | 96    | 11.37  | 6         | B > 24             |            | 7,1         |
| $RBS 1223^{(a)}$  | 86    | 10.31  | 18        | $m_{50ccd} = 28.6$ |            | 8,9,10,11   |
| RX J1605.3 + 3249 | 96    | 6.88?  | ?         | B = 27.2           | 145        | 12,13,14,15 |
| RX J1856.5 - 3754 | 62    | _      | < 1.3     | B = 25.2           | 332        | 16,17,18,19 |
| RBS $1774^{(b)}$  | 102   | 9.44   | 4         | B > 26             |            | 20,21,22    |

 $<sup>^{(</sup>a)} = 1RXS J130848.6 + 212708$   $^{(b)} = 1RXS J214303.7 + 065419$ 

#### References:

- (1) Haberl et al. (2004a) (2) Haberl et al. (1997) (3) Cropper et al. (2001)
- (4) Haberl et al. (2004b) (5) de Vries et al. (2004) (6) Motch et al. (2003)
- (7) Haberl & Zavlin (2002) (8) Schwope et al. (1999) (9) Hambaryan et al. (2002)
- (10) Kaplan et al. (2002a) (11) Haberl et al. (2003) (12) Motch et al. (1999)
- (13) Kaplan et al. (2003) (14) van Kerkwijk et al. (2004) (15) Motch et al. (2005)
- (16) Walter & Matthews (1997) (17) Walter & Lattimer (2002) (18) Burwitz et al. (2003)
- (19) van Kerkwijk & Kulkarni (2001) (20) Zampieri et al. (2001) (21) Zane et al. (2005)
- (22) Komarova (2006)

#### Table C.2: Magnetic field estimates for the Magnificent Seven

This table by Haberl (2006) gives an overview about different magnetic field estimates considering recent spectral fits of the M7. Listed are for each object the measured pulse period derivative  $\dot{P}$  or its limit, the line energy  $E_{\rm cyc}$  of a particular absorption feature which is assumed to be due to cyclotron resonance by protons, the magnetic field  $B_{\rm db}$  utilizing the magnetic dipole braking model for the pulsars with measured pulse period derivative, and the magnetic field  $B_{\rm cyc}$  if proton cyclotron lines are assumed. If multiple absorption lines were included in the spectral modeling, the lowest line energy was used for the estimate of the magnetic field.

| Object            | $\mathrm{d}P/\mathrm{d}t$    | $E_{ m cyc}$                        | $B_{ m db}$           | $B_{ m cyc}$          |
|-------------------|------------------------------|-------------------------------------|-----------------------|-----------------------|
|                   | $[10^{-13} \text{ ss}^{-1}]$ | [eV]                                | $[10^{13} \text{ G}]$ | $[10^{13} \text{ G}]$ |
| RX J0420.0-5022   | <92                          | 330                                 | <18                   | 6.6                   |
| RX J0720.4 - 3125 | 0.698(2)                     | 280                                 | 2.4                   | 5.6                   |
| RX J0806.4 - 4123 | <18                          | $430 \text{ or } 430/306^{(a)}$     | <14                   | 8.6 or 6.1            |
| RBS1223           | 1.120(3)                     | $300 \text{ or } 300/230^{(a)}$     | 3.4                   | 6.0  or  4.6          |
| RX J1605.3+3249   |                              | $450 \text{ or } 400/600/800^{(b)}$ |                       | 9 or 8                |
| RX J1856.5 - 3754 |                              | _                                   | $\sim 1^{(c)}$        |                       |
| RBS 1774          | $<60^{(d)}$                  | 750                                 | $<24^{(d)}$           | 15                    |

<sup>(</sup>a) Spectral fit with single line or two lines

<sup>(</sup>b) Spectral fit with single line or three lines

<sup>(</sup>c) Estimate from Hα nebula assuming that it is powered by magnetic dipole breaking (Kaplan et al., 2002b, Braje & Romani, 2002, Trümper et al., 2004)

<sup>(</sup>d) claimed radio detection: Malofeev et al. (2006)

# Appendix D Additional tables to Chapter 2

| star ass. | l     | b     | d                | Nt | star ass. | l     | b     | d                | Nt  |
|-----------|-------|-------|------------------|----|-----------|-------|-------|------------------|-----|
|           | [deg] | [deg] | $[\mathrm{kpc}]$ |    |           | [deg] | [deg] | $[\mathrm{kpc}]$ |     |
| SGR OB5   | 0.0   | -1.2  | 2.4              | 31 | CAS OB8   | 129.2 | -1.1  | 2.3              | 43  |
| SGR OB1   | 7.6   | -0.8  | 1.3              | 66 | PER OB1   | 134.7 | -3.2  | 1.8              | 167 |
| SGR OB4   | 12.1  | -1.0  | 1.9              | 15 | CAS OB6   | 135.0 | 0.8   | 1.8              | 46  |
| SER OB1   | 16.7  | 0.1   | 1.5              | 43 | CAM OB1   | 141.1 | 0.9   | 0.8              | 50  |
| SER OB2   | 18.2  | 1.6   | 1.6              | 18 | AUR OB1   | 173.9 | 0.1   | 1.1              | 36  |
| VUL OB1   | 60.4  | 0.0   | 1.6              | 28 | AUR OB2   | 173.3 | -0.2  | 2.4              | 20  |
| CYG OB3   | 72.8  | 2.0   | 1.8              | 42 | GEM OB1   | 189.0 | 2.2   | 1.2              | 40  |
| CYG OB1   | 75.8  | 1.1   | 1.5              | 71 | MON OB2   | 207.5 | -1.6  | 1.2              | 32  |
| CYG OB9   | 77.8  | 1.8   | 1.0              | 32 | CMA OB1   | 224.6 | -1.6  | 1.1              | 17  |
| CYG OB8   | 77.9  | 3.4   | 1.8              | 21 | VELA OB1  | 264.9 | -1.4  | 1.5              | 46  |
| CYG OB2   | 80.3  | 0.9   | 1.5              | 15 | CAR OB1   | 286.5 | -0.5  | 2.0              | 126 |
| CYG OB7   | 89.0  | 0.0   | 0.6              | 29 | TR 16     | 287.3 | -0.3  | 2.1              | 18  |
| CEP OB2   | 102.1 | 4.6   | 0.7              | 59 | COLL 228  | 287.6 | -1.0  | 2.0              | 15  |
| CAS OB2   | 112.0 | 0.0   | 2.1              | 41 | CAR OB2   | 290.4 | 0.1   | 1.8              | 59  |
| CEP OB3   | 110.4 | 2.6   | 0.7              | 26 | CRU OB1   | 294.9 | -1.1  | 2.0              | 76  |
| CAS OB5   | 116.1 | -0.5  | 2.0              | 52 | CEN OB1   | 304.2 | 1.4   | 1.9              | 103 |
| CAS OB4   | 120.1 | -0.3  | 2.3              | 27 | ARA OB1A  | 337.7 | -0.9  | 1.1              | 53  |
| CAS OB7   | 123.0 | 1.2   | 2.0              | 39 | SCO OB1   | 343.7 | 1.4   | 1.5              | 76  |

**Table D.1:** These 36 star associations outside a 400 pc radius around the sun are considered as most probable birth places of neutron star. They are taken from the catalogs by Blaha & Humphreys (1989) and Mel'nik & Efremov (1995). Listed are the name of the star association, the galactic longitude l, the galactic latitude b, the distance d and the number of known members Nt. Note that the distances to the associations are reduced (the distances given by Blaha & Humphreys (1989) are multiplied by 0.8) according to Dambis et al. (2001).

## Appendix E

### Additional tables to Chapter 3

Table E.1: ROSAT HRI hardness ratios for five of the Magnificent Seven Listed are the different available HRI pointings with the corresponding exposure time, the determined source position and the  $HR_{HRI}$  from the catalogue by R. Supper and W. Voges. The error of  $HR_{HRI}$  is usually rather small. However, this can be caused by a large number of background counts, from which the ROSAT HRI often suffered (W. Voges, personal communication).

| Name                  | ObsID       | Exposure | RA       | DEC      | $HR_{HRI}$       |
|-----------------------|-------------|----------|----------|----------|------------------|
|                       |             | [s]      | [deg]    | [deg]    |                  |
| RX J0420.0-5022       | wg600959h   | 5722     | 65.0091  | -50.3796 | $-0.05 \pm 0.09$ |
| RX J0420.0-5022       | wg600959h-1 | 1147     | 65.0080  | -50.3807 | $+0.70 \pm 0.16$ |
| RX J0720.4-3125       | wg400884h   | 33231    | 110.1040 | -31.4310 | $-0.03 \pm 0.01$ |
| RX J0720.4-3125       | wg400944h   | 8005     | 110.1029 | -31.4304 | $+0.49 \pm 0.02$ |
| RX J0720.4-3125       | wg300508h   | 3519     | 110.1028 | -31.4302 | $+0.20 \pm 0.03$ |
| RX J0720.4-3125       | wg300508h-1 | 1388     | 110.1039 | -31.4298 | $+0.17 \pm 0.05$ |
| 1RXS J130848.6+212708 | wg704082h   | 4883     | 197.2014 | 21.4518  | $+0.60 \pm 0.04$ |
| 1RXS J130848.6+212708 | wg703848h   | 2189     | 197.2006 | 21.4522  | $-0.20 \pm 0.06$ |
| RX J1605.3+3249       | wg400938h   | 2090     | 241.3277 | 32.8211  | $+0.52 \pm 0.01$ |
| RX J1856.5-3754       | us400864h   | 28724    | 284.1478 | -37.9101 | $-0.48 \pm 0.01$ |
| RX J1856.5-3754       | us400612h   | 17557    | 284.1473 | -37.9092 | $+0.42 \pm 0.01$ |

Table E.2: Hardness ratios of the Magnificent Seven

Listed are the ROSAT PSPC hardness ratios  $HR1^{PSPC}$  and  $HR2^{PSPC}$ , as well as the hardness ratio  $HR_{XMM}$ , which was obtained by considering the two energy bands [0.15, 0.5] keV and [0.5, 1.0] keV of available archival XMM-Newton EPIC-pn observations (see sec. 3.3 for method).

| Name                  | $HR1^{PSPC}$         | $HR2^{PSPC}$                  | $HR_{XMM}$                     |
|-----------------------|----------------------|-------------------------------|--------------------------------|
| RX J0420.0-5022       | $-0.96 \pm 0.03^{a}$ | $-0.45 \pm 0.73^{a}$          | $-0.91 \pm 0.01$               |
| RX J0720.4-3125       | $-0.82 \pm 0.01$     | $-0.77 \pm 0.03$              | $-0.40 \cdots -0.56 \pm 0.002$ |
| RX J0806.4-4123       | $-0.74 \pm 0.02$     | $-0.66 \pm 0.08$              | $-0.49 \pm 0.01$               |
| RBS $1223^{1}$        | $-0.20 \pm 0.08^{a}$ | $-0.51 \pm 0.1^{\rm a}$       | $-0.20 \pm 0.004$              |
| RX J1605.3+3249       | $-0.67 \pm 0.02$     | $-0.68 \pm 0.04$              |                                |
| RX J1856.5-3754       | $-0.96 \pm 0.01$     | $-0.94 \pm 0.02$              |                                |
| RBS 1774 <sup>2</sup> | $-0.06 \pm 0.12^{a}$ | $-0.60 \pm 0.17^{\mathrm{a}}$ |                                |

<sup>&</sup>lt;sup>1</sup> 1RXS J130848.6+212708, <sup>2</sup> 1RXS J214303.7+065419

<sup>&</sup>lt;sup>a</sup> from RASS

#### Table E.3: SSC2 hardness ratios of the Magnificent Seven

For the M7 with entries in the second XMM-Newton Serendipitous Source Catalogue (SSC2) (prereleased at 20th July 2006) are listed with errors: the count rate PN CR with the pn-camera (PN8rate in SSC2) and the hardness ratios  $HR1_{PN}$  to  $HR3_{PN}$  obtained with the pn-camera. At the end the revolution number, REV, is given (the entries for the REV with the lowest count rate errors are chosen). All sources except RX J1605.3+3249 are observed in EPIC-pn full frame mode with the thin filter.

| Name                                     | PN CR                        | $HR1_{PN}$         | $HR2_{PN}$          | $HR3_{PN}$         | REV |
|--|------------------------------|--------------------|---------------------|--------------------|-----|
|  | $[{\rm cnts}\ {\rm s}^{-1}]$ |                    |                     |                    |     |
| RX J0420                                 | $0.1002 \pm 0.0025$          | $-0.90 \pm 0.01$   | $-0.87 \pm 0.07$    | $-0.24 \pm 0.50$   | 560 |
| RX J0720                                 | $6.7088 \pm 0.0156$          | $-0.455 \pm 0.002$ | $-0.918 \pm 0.002$  | $-1.000 \pm 0.003$ | 534 |
| RX J0806                                 | $1.5543 \pm 0.0098$          | $-0.44 \pm 0.01$   | $-0.90 \pm 0.01$    | $-0.99 \pm 0.02$   | 618 |
| RBS $1223^{1}$                           | $2.6145 \pm 0.0105$          | $-0.164 \pm 0.004$ | $-0.931 \pm -0.002$ | $-1.00 \pm 0.01$   | 561 |
| $RX J1605^a$                             | $3.9581 \pm 0.0126$          | $-0.433 \pm 0.003$ | $-0.901 \pm 0.003$  | $-1.00 \pm 0.01$   | 569 |
| $\mathrm{RX}\;\mathrm{J}1856^\mathrm{b}$ |                              |                    |                     |                    |     |
| RBS $1774^{2b}$                          |                              |                    |                     |                    |     |

 $<sup>^{1}</sup>$  1RXS J130848.6+212708,  $^{2}$  1RXS J214303.7+065419,

<sup>&</sup>lt;sup>a</sup> Large field mode of EPIC-pn and thin filter,

<sup>&</sup>lt;sup>b</sup> not included in SSC2 due to observations only available in Small Field Mode

Table E.4: Bad Pixels for XMM-Newton EPIC-pn at energies < 200eV Listed are the CCD number, RAWX and RAWY CCD coordinates, extension in X and Y for new bad pixels found to be present in most of the deep XMM-Newton EPIC-pn full frame mode observations if one considers detector energies from 150 eV to 1 keV.

| CCD <sup>a</sup> | RAWX | RAWY | $X_{ext}$ | $Y_{ext}$ | CCD <sup>a</sup> | RAWX | RAWY | $X_{ext}$ | $Y_{ext}$ |
|------------------|------|------|-----------|-----------|------------------|------|------|-----------|-----------|
| 2                | 43   | 50   | 1         | 1         | 8                | 9    | 153  | 1         | 1         |
| 3                | 23   | 37   | 2         | 1         | 8                | 3    | 146  | 1         | 1         |
| 4                | 30   | 82   | 1         | 1         | 8                | 44   | 122  | 1         | 1         |
| 5                | 41   | 182  | 1         | 3         | 8                | 53   | 87   | 1         | 1         |
| 5                | 2    | 150  | 1         | 1         | 8                | 63   | 61   | 1         | 1         |
| 5                | 9    | 70   | 1         | 1         | 9                | 10   | 129  | 1         | 2         |
| 6                | 51   | 182  | 1         | 1         | 10               | 39   | 169  | 1         | 1         |
| 7                | 27   | 112  | 1         | 1         | 10               | 41   | 19   | 1         | 1         |
| 7                | 33   | 47   | 1         | 1         | 11               | 28   | 180  | 1         | 1         |

<sup>&</sup>lt;sup>a</sup> see e.g. XMM-Newton User Handbook for definition http://xmm.esac.esa.int/external/xmm\_user\_support/documentation/uhb\_2.1/node27.html

## **Acknowledgement // Danksagung**

Meinen beiden Betreuern, Herrn Prof. Dr. G. Hasinger (MPE) und Herrn Prof. Dr. R. Neuhäuser (AIU), möchte ich herzlich für die Begleitung meiner Doktorandenzeit mit zahlreichen Anregungen, Ermunterungen und hilfreichen Diskussionen bedanken, ebenso für das Ermöglichen von Konferenz- und Kooperationspartnerbesuchen sowie Anmerkungen zum Manuskript.

Sehr dankbar bin ich auch Herrn Prof. Dr. J. Trümper (MPE), durch den ich jetzt einen klareren Blick auf den Dschungel der Neutronensterne und ihrer Eigenschaften habe. Insbesondere seine Erklärungen und das kritische Durchkucken des Manuskripts hat mir sehr geholfen, dem Verständnis der Neutronensternphysik näher zu kommen.

Ein großer Dank geht auch an Dr. F. Haberl (MPE), dessen stets kompetente Erklärungen und Ratschläge einen wesentlichen Anteil daran haben, dass für mich die Röntgenastronomie jetzt weniger geheimnisvoll, dafür aber eine wunderbar spannende Angelegenheit ist. Ebenso habe ich viel über Neutronensterne von ihm gelernt. Vielen Dank auch für die Durchsicht des Manuskripts.

I want to thank my collaborators Dr. S. B. Popov (Sternberg, Moscov) and Dr. M. Agüeros (University of Washington, Seattle) for the very fruitful cooperations. Dr. S. B. Popov introduced me very carefully to his population synthesis model explaining many problems (and possible solutions). I enjoyed the lively discussions with him as well as sharing new ideas. I want to thank Dr. S. B. Popov for reading of my population synthesis chapter and his suggestions, too.

I am very grateful to Dr. M. Agüeros that he was also interested in allowing a competing *Sloan*-project to become a very successful cooperational work. The world of the *Sloan Digital Sky Survey* is now more familiar to me thanks to him. Many thanks especially for proof-reading and the language correction of most of my English manuscript! In this respect I want to thank Dr. L. Gallo (MPE) as well who also proof-read one chapter of my English manuscript. The suggestions by Dr. M. Agüeros and Dr. L. Gallo have highly improved the readability of this thesis.

I want to thank Prof. Dr. R. Turolla (University of Padova) whose hospitality in Padova I highly enjoyed as well as the enlightening discussions with him.

I am very grateful to Dr. R. Lallement (CNRS, Paris). She kindly provided me with her great work, the Natrium density cube, and answered all my questions.

Thanks go to Prof. Dr. F. Walter (State University of New York), Drs. C. Motch (University of Strasbourg), and R. Mignani (ESO //MSSL London) whose deep optical observations I got in reduced, calibrated form together with explanations.

I want to thank Drs. D. Lorimer (West Virginia University, Morgantown).and B. Klein (MPI für Radioastronomie, Bonn) who let me realize that neutron stars are not only interesting in X-rays and also provided me with their software and answers to many questions concerning radio observations of pulsars.

Ein großer Dank geht auch meine Kollegen, sowohl am Astrophysikalischen Institut in Jena als auch in der Röntgengruppe am MPE in Garching. Besonders dankbar bin ich folgenden Kollegen: Dr. M. Freyberg für das schnelle Vorprozessieren meiner zahlreichen XMM-epreject-Datensätze, Dr. W. Pietsch für das Überlassen eines XMM-SAS-Programms als Starthilfe, Dr. W. Voges für ROSAT und Sloan-Erkenntnisse, den Dres. K. Dennerl, H. Brunner, P. Predehl, E. Pfeffermann und V. Burwitz für erhellende Erklärungen und Diskussionen, sowie Dr. G. Lemson für seine Hilfe bei der Sloandatenabfrage. Auf AIU-Seite bin ich besonders Dipl. Phys. A. Seifahrt für zahlreiche Diskussionen über die Geheimnisse von Gaia und IDL dankbar. Wertvolle Anregungen habe ich auch von Dr. K. Schreyer und Dr. G. Wuchterl bekommen. Den Dres. M. Ammler und C. Broeg bin ich für Hinweise zu Formalien und LATEX-Tipps dankbar.

Ohne die beiden Systemadministratoren – H. Baumgartner auf MPE-Seite und J. Weiprecht auf AIU-Seite – wäre diese Arbeit nicht möglich gewesen. Stets waren sie mit Rat und Tat zur Stelle wenn die Rechner mal wieder nicht so wollten wie sie sollten oder der Plattenplatz eng wurde.... Vielen Dank.

Freundliche, hilfsbereite Kollegen sowohl am MPE als auch am AIU zu haben, hat mir bei meiner Arbeit sehr geholfen. Stellvertretend für das AIU möchte ich an dieser Stelle insbesondere Dr. M. Ammler danken, der viele kleine Dinge am AIU im Auge behielt, die das Leben aller sehr erleichterten. Stellvertretend für das MPE möchte ich Dipl. Phys. F. Mokler danken, die durch ihre freundliche Aufnahme sehr viel des tristen Hotelalltags abmilderte.

Ich bin meinen Kollegen und den jeweiligen Institutsleitern auch sehr dankbar für die Duldung von Rana als arbeitsfördernder Maßnahme.

Besonders möchte ich mich bei meiner Familie bedanken, die meine Arbeit stets unterstützend begleitetete, im Fall der Fälle immer zur Stelle war und mir die Ruhe für dieses Werk gab.

Dir, mein lieber Jan, gebührt ein ebenfalls besonders großer Dank. Nicht nur für die zahlreichen Diskussionen, Anregungen und der kritischen Durchsicht meiner Texte bin ich Dir dankbar, sondern auch für Deine Unterstützung, Deinen Humor und für die zahlreichen nichtphysikalischen Erbauungen.

Den Herren J.S. Bach, J. Brahms, G. Fauré, F.-G. Gossec, G.-F. Händel, F. Mendelsohn-Bartholdy, M. Mussorgksy, J.-D. Zelenka u.a. bin ich sehr für künstlerische Anregungen verbunden.